May 2018

The Design, Modeling, and Optimization of a Biomimetic Soft Robot for Fluid Pumping and Thrust Generation Using Electroactive Polymer Actuators

Zakai Jedidiah Olsen
zakaiolsen@gmail.com

THE DESIGN, MODELING, AND OPTIMIZATION OF A BIOMIMETIC SOFT ROBOT

FOR FLUID PUMPING AND THRUST GENERATION USING ELECTROACTIVE

POLYMER ACTUATORS

By

Zakai J. Olsen

Bachelor of Science in Engineering – Mechanical Engineering
University of Nevada, Las Vegas
2016

A thesis submitted in partial fulfillment
of the requirements for the

Master of Science in Engineering – Mechanical Engineering

Department of Mechanical Engineering
Howard R. Hughes College of Engineering
The Graduate College

University of Nevada, Las Vegas
May 2018

Thesis Approval

The Graduate College
The University of Nevada, Las Vegas

April 13, 2018

This thesis prepared by

Zakai J. Olsen

entitled

The Design, Modeling, and Optimization of a Biomimetic Soft Robot for Fluid Pumping and Thrust Generation Using Electroactive Polymer Actuators

is approved in partial fulfillment of the requirements for the degree of

Master of Science in Engineering – Mechanical Engineering
Department of Mechanical Engineering

Kwang Kim, Ph.D.   Kathryn Hausbeck Korgan, Ph.D.
Examination Committee Chair   *Graduate College Interim Dean*

Mohamed Trabia, Ph.D.
Examination Committee Member

Woosoon Yim, Ph.D.
Examination Committee Member

Rebecca Martin, Ph.D.
Graduate College Faculty Representative

Abstract

Nature is a constant source of inspiration for engineers and scientists through its simple, effective, and elegant solutions to many complex problems. Smart materials and soft robotics have been seen to be particularly well suited for developing biomimetic devices and are active fields of research. In this study, the design, modeling, and optimization of a new biomimetic soft robot is described. Preliminary work was made in the modeling of a biomimetic robot based on the locomotion and kinematics of jellyfish. Modifications were made to the governing equations for jellyfish locomotion that accounted for geometric differences between biology and the robotic design. Particularly, the capability of the model to account for the mass and geometry of the robot design. A simple geometrically defined model is developed and used to show the feasibility of a proposed biomimetic robot. With the concept verified, a more robust physics-based model is developed. In this model, linear beam theory is coupled to an equivalent circuit model to actuate the robot with ionic polymer-metal composite (IPMC) actuators. The circuit model is verified using a robust, Multiphysics finite element model of the IPMC actuator. The newly created physics-based model of the soft robot is compared to that of the geometric model as well as biological jellyfish swimming to highlight its improved efficiency. The design is then optimized using a sequential quadratic programming algorithm for nonlinear multivariable optimization. Standard deviations of the optimized values are used to verify their accuracy, and the propulsion efficiency of the unoptimized and optimized model are compared to verify the improvement in efficiency and overall performance. Scale effects on the optimal design are also examined as an initial form of dimensional analysis. The optimized design shows clear improvement over the unoptimized counterpart, and the modularity of the modeling approach allows for more complex models that include nonlinearities to be easily added.

Acknowledgements

I would like to thank my advisor, Dr. Kwang Kim, for his immense support and advice throughout my undergraduate and graduate studies. His mentorship, teaching, financial support, research guidance, and amazing travel opportunities given to me have greatly shaped my career as an engineer and researcher. I am profoundly grateful for Dr. Kim's generosity and interest invested in these many areas of my life, all of which have helped lead me to graduating at this time.

I would also like to thank committee members, Dr. Mohamed Trabia, Dr. Woosoon Yim, and Dr. Rebecca Martin for their teaching and advice during my career at UNLV. I truly appreciate their time and interest spent on my studies and development as a researcher.

All of the faculty and staff who have had such a positive impact on me throughout my time at UNLV are very much appreciated and my sincere thanks go to each of them. The incredible professors I have studied under have given me the education necessary to pursue a graduate career, and beyond. I would like to specifically thank Joan Conway for all her incredible assistance, encouragement, and support. All my colleagues in the AMSL lab who helped me throughout my graduate studies are well-deserving of my thanks. Their advice and support are greatly appreciated, equally as much as their friendship. I also thank the National Science Foundation PIRE program and the Nevada NASA Space Grant Consortium for the funding and support for my graduate research.

Finally, an acknowledgement of warmhearted gratitude for my friends and family. Their continual support of my academic and professional endeavors has helped me stay focused and level-headed. I particularly give special thanks to my younger brother, Luke Olsen, for always being there to give his advice and perspective whenever I needed it.

Table of Contents

List of Tables

List of Figures

Nomenclature

A_v	Velar / valve aperture area (m^2)	G	Acceleration reaction (N)
α_h	Hydrofilicity coefficient (N-m/mol)	h	Bell height (m)
		h_t	Integrator time step (s)
α_{AM}	Added mass coefficient	I	Moment of inertia (m^4)
α_{RCW}	Hydrofilicity coefficient for circuit model (N/m-C)	J	Cation flux (mol/m^3-s)
		κ	Bending strain (1/m)
α_c	Hydrofilicity coefficient in COMSOL (N/C)	L_c	Characteristic length (m)
		m	Mass of jellyfish / robot (kg)
α	Starting polar angle	μ	Cation mobility (s-mol/kg)
β_h	Hydrofilicity coefficient (N-m^4/mol^2)	N_w	Number of shape functions
		$\boldsymbol{N_s}$	Vector of shape functions
β	Ending polar angle	$\boldsymbol{N_\zeta}$	Vector of nondimensional shape functions
C_d	Drag coefficient		
c_0	Anion concentraction (mol/m^3)	ν	Kinematic viscosity of water (m^2/s)
C	Stiffness tensor (Pa)		
c	Cation concentration (mol/m^3)	O_G	Order of gauss quadrature
D_e	Electric displacement (C/m^2)	P_w	Transverse loading (N/m)
D_{force}	Drag force of jellyfish / robot (N)	ϕ	Electric potential (V)
		Q	Charge in IPMC (C)
δ_i	Perturbation of ith SQP variable	ρ_w	Density of water (kg/m^2)
δ_t	Time ratio	ρ_c	Charge density (C/m^3)
D	Cation diffusivity (m^2/s)	ρ_m	Material density (kg/m^3)
dV	Volume change for jellyfish swimming model (m^3)	Re	Reynold's number
		r	Instantaneous bell radius (m)
$\vec{E}$	Electric field strength (N/C)	ρ	Radius of curvature (m)
ε_0	Dielectric constant in vacuum (F/m)	S_0	Initial cross-sectional area (m^2)
		S_A	Cross-sectional area w.r.t flow (m^2)
ε_d	Strain tensor		
ε_r	Relative dielectric constant	σ_{ext}	External stress (Pa)
η_{prop}	Propulsion efficiency	σ	Stress tensor (Pa)
ϵ_L	Minimum allowable passive material (m)	t_c	Contraction time (s)
		t_m	Time since last contraction cycle start (s)
E	Young's modulus (Pa)		
ε	Absolute dielectric constant (F/m)	t_r	Relaxation time (s)
		θ_s	Polar angle of beam (rad)
ϵ	Axial strain	T	Thrust force of jellyfish / robot (N)
F_b	Body forces (N/m^3)		
$F_{inertia}$	Inertial force (N)	t	Time (s)
G_p	Gauss-Legendre point	u_e	Velocity of exchanged fluid (m/s)
G_w	Gauss-Legendre weight		

$\vec{u}$	Material displacement field (m)
u_x	Deflection along x-axis (m)
u_y	Deflection along y-axis (m)
u	Swimming velocity (m/s)
V_f	Total volume of fluid (m^3)
V_i	Internal volume
v_e	Ejected fluid velocity (m/s)
v	Axial deflection (m)
w	Transverse deflection (m)
$\widetilde{w}$	Trial displacemnt (m)
$\widehat{w}$	Galerkin coefficient
$\widehat{\widetilde{w}}$	Modified Galerkin coefficient
$\boldsymbol{\widehat{w}}$	Vector of coefficients
$X_{i,0}$	Initial value of ith SQP variable
x_i	Nominal value of ith SQP variable
Z_{Cap}	Capacitive impedance (1/F)
Z_R	Resistive impedance (Ohm)
$Z_{Warburg}$	Warburg ipmedance (1/Ohm-s^2)
z	Charge number
ζ	Nondimensional axial coordiante

Chapter 1. Introduction

Over the last 25 years, electroactive polymers (EAP) have emerged and grown into a vast and diverse field of research, with numerous potential applications in soft robotics and smart materials. Due to their similar behavior to biological muscle, these materials are commonly referred to as artificial muscles [1]. O'Halloran et al give an overview of EAP technology in [2], but the basic operation of these materials is a transduction of electrical stimuli into mechanical deformation. Most EAP materials have the capability of both electromechanical transduction, where they can act as actuators [3–5], as well as mechanoelectrical transduction, where they work as sensors [6–9]. This duality lies in the fundamentals of the electrochemical nature that governs both transduction modes, and is explored throughout literature [10–13]. The class of EAP includes materials such as dielectric elastomers, ferroelectric polymers, ionic polymer gels, and many more [2].

In this work the focus is placed on the ionic polymer-metal composite (IPMC). This material consists of an ionic polymer, typically Nafion® or Aquivion® [4,14], that is composited between two electrodes, most commonly platinum or gold. While there are a few fabrication methods for such materials, typically the electrodes are plated to an activated polymer membrane through an electroless process [15]. IPMC actuators have a unique characteristic in that they exhibit large mechanical deformations in response to a relatively low voltage [1,11,14,16,17], making them attractive for compact, low power soft robotics.

IPMCs achieve their electromechanical transduction due to free moving cations within the polymer that are hydrated with water molecules. Under an applied electric potential to the electrodes, these hydrated cations migrate to the cathode and cause swelling at the polymer-electrode interface, which in turn bends the IPMC towards the anode. Due to the similarities of

1

EAP to biological muscle, biology inspires many soft robotic designs seen in literature. This gives rise to an entire field of soft robotics, namely, biomimetic soft robotics [5,18].

The IPMCs ability to actuate in water [19–22] has focused the soft robotics development heavily on aquatic animals. The biomimetic applications of IPMCs range from small scale biological structures such as cilia [23] all the way up to full size robots [24]. Fabrication of fin-like actuators has been demonstrated in [15,25,26], while the authors in [27–32] all worked on developing small fish-like robots. Manta ray robots are seen in the works of [33,34], and a tiny dolphin robot is found in [35]. As will be elaborated on later, the jellyfish is of interest for this research. Many others have developed biomimetic jellyfish robots, using EAPs as well as traditional robotic actuators. A few of these designs can be found in [36–42].

The jellyfish has been the focus of many researchers in the biology and engineering field, with varying interests in its swimming mechanism. As will be discussed in the next chapter, the jellyfish utilizes what is known as a jet propulsion method of locomotion. This has been extensively explored throughout literature from hydrodynamic, kinematic, and geometric perspectives. The interest here is to examine the behavior of the swimming jellyfish and develop a new biomimetic soft robot that builds on the basic mechanisms used in biology for locomotion and address any observed limitations.

Chapter 2. Biological Inspiration

2.1. Kinematics of Swimming Jellyfish

The work of [43] gives a great overview on biological and bioinspired forms, and has a wide breadth of information on the propulsion mechanisms used in nature by aquatic animals. There, the mechanism of jet propulsion is described as a method for fish locomotion. Jet propulsion is broken into three categories, bell constriction, mantel constriction, and shell compression. The jellyfish, as noted in the aforementioned work, mainly utilizes the bell constriction form of jet propulsion.

This swimming behavior is characterized by the movement of a flexible bell, and propulsion is generated during alternating contraction and relaxation phases of the bell muscles, ejecting or refilling water into the volume of the bell. Two forms of bell constriction are available to jellyfish, depending on their geometry. Namely, jet and rowing propulsion, which are similar in the muscles activated during swimming, but differentiated by size of the muscle necessary to achieve each. The jet method of propulsion is of interest in this work, and it will be assumed from here onward that when referring to jellyfish swimming that jet propulsion will be the mechanism that is used. An illustrative graphic of the bell deformation that occurs during the contraction and relaxation phases is provided in Figure 2.1.

Numerous studies have been conducted into the self-propulsion of aquatic animals. Specifically, Lauder et al. researched the use of bio-robotic models and how they may provide insight into the hydrodynamics and kinematics of aquatic propulsion, Lu et al. investigated the hydrodynamics of fish-like swimming through the use of numerical and experimental studies, and Triantafyllou et al. worked on the optimal thrust generated via jet-like flows from oscillating

foils similar to that of fish fins [44–46]. More in line with the work presented here, the jet

propulsion of aquatic animals such as the jellyfish has been studied in [47–49].

The jellyfish itself has been the center of numerous studies involving a wide range of

topics, such as the flow patterns during swimming, bell deformation kinematics, dynamics and

structure, and the hydrodynamic effects of the biological structure and locomotion of the animal.

These topics can be found throughout literature in [50–57]. Of particular interest is the work

found in [51,58,59] where dynamic equations of motion (EoM) can be found that can be used to

model the biological jet propulsion of jellyfish. These will be used and modified later in order to

simulate the swimming of a proposed biomimetic soft robot.
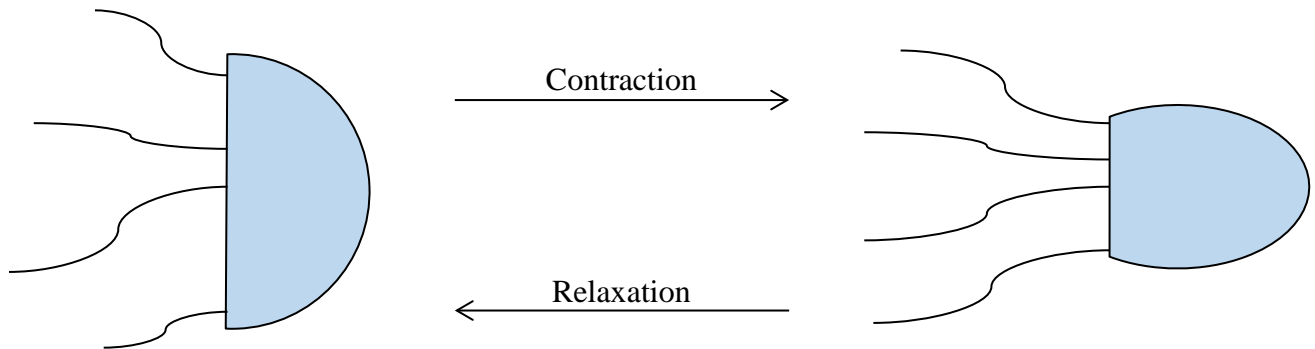
Figure 2.1 Illustration of Jet Propulsion Mechanism Found in Biological Jellyfish
In between contraction and relaxation phases the fluid contained within the body of the jellyfish
is exchanged with the surrounding fluid and the momentum exchanged in this process results in a
net-positive thrust over the duration of a complete swimming cycle.

2.1.1. Derivation of Governing Equations

The jet propulsion mechanism of the jellyfish as studied in [58] follows a simple dynamic

EoM that can be used to simulate the swimming behavior of biological jellyfish. This also

provides a source point for modeling jellyfish-like robotics, which will be demonstrated later in

Chapter 4.1. Here, the governing equation is re-derived from [58] and analyzed to visualize how

biological jellyfish swim, as well as give rise to the inspiration that leads to the development of the soft robot design presented later in this chapter.

In [58], the jet propulsion swimming mechanism was broken down into four components: thrust, drag, inertia, and acceleration reaction. Each of these is modeled independently and then assembled to give the full dynamic EoM, that governs the swimming motion. Following the derivation of [58], the thrust is written as

$$T = u_e \frac{dm}{dt} \tag{2.1}$$

where T, u_e, and m are the thrust, velocity of fluid exchanged, and the mass of the jellyfish and contained fluid volume.

Writing the mass of the jellyfish in terms of the total volume of the jellyfish and contained fluid, assuming the jellyfish is roughly the density of water [60], allows the ejected fluid velocity to be written as a function of total volume

$$\frac{dm}{dt} = \rho_w \frac{dV_f}{dt} \tag{2.2}$$

$$u_e = \frac{1}{\rho_w A_V} \frac{dm}{dt} = \frac{1}{A_V} \frac{dV_f}{dt} \tag{2.3}$$

where ρ_w, V_f, and A_V are the density of water, total volume, and velar aperture area, respectively [52,58]. Now, thrust can be rewritten in terms of water density, velar aperture, and total volume

$$T = \frac{\rho_w}{A_V} \left(\frac{dV_f}{dt} \right)^2 \tag{2.4}$$

5

The drag component in the EoM is governed by the standard drag equation, given as

$$D_{\text{force}} = \frac{1}{2}C_d\rho_w S_A u^2 \tag{2.5}$$

where D is the drag force, C_d is the drag coefficient, S_A is the cross-sectional area with respect to the swimming direction, and u is the swimming speed of the jellyfish. Both the drag coefficient and cross-sectional area change as the jellyfish body deforms during swimming. To obtain the cross-sectional area, the truncated bell shape is used to derive the following expression for area as a function of volume

$$S_A = S_0 + \frac{3}{2h}\frac{dV_f}{dt}t \tag{2.6}$$

with S_0 being the initial cross-sectional area and h the height of the bell geometry at the start of a contraction phase. The structure of this truncated bell shape is shown in Figure 2.2.
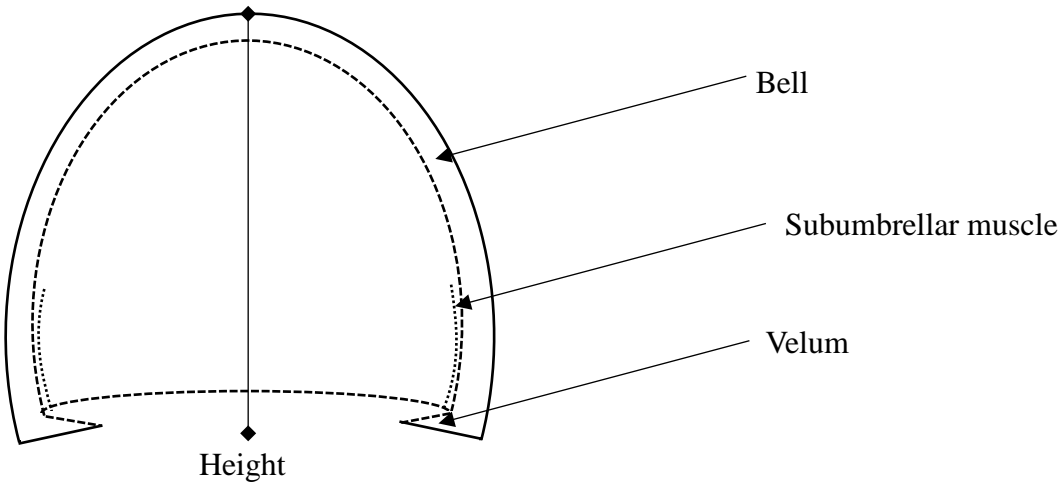
Figure 2.2 Illustration of Jellyfish Body Structure
The hemiellipsoid structure of the jellyfish body can be defined through the bell height and the velar aperture radius.

The drag coefficient can be related to the Reynold's number by assuming that the jellyfish bell behaves roughly the same as that of a sphere, providing a simple relation between flow speed and drag coefficient

$$C_d = \frac{24}{(Re)^n} = 24\left(\frac{\nu}{uL_c}\right)^n \tag{2.7}$$

where the definition of the Reynold's number has been used with a kinematic viscosity of ν and characteristic length of L_c, calculated here as the ratio of volume to cross-sectional area. The exponent n is defined as [58]

$$n = \begin{cases} 1.0 & Re < 1 \\ 0.7 & Re < 500 \end{cases} \tag{2.8}$$

Acceleration reaction is an inertial type force that arises when an object accelerates through a fluid and is related to the inertia of the fluid that must be accelerated around the geometry of the object. Here, the acceleration reaction is

$$G = -\alpha_{AM}\rho V_f \frac{du}{dt} \tag{2.9}$$

where α_{AM} is the added mass coefficient. From the form of this equation it is clear where the terms acceleration reaction and added mass come from. This force can be viewed as an additional mass the object must accelerate through the fluid, which is a function of the physical geometry of the object itself. Experiments have determined an added mass coefficient for a hemiellipsoid to be given by the following regression equation [58]

$$\alpha_{AM} = \left(\frac{h}{r}\right)^{1.4} \tag{2.10}$$

in which r is the instantaneous bell radius. These force components must balance with the jellyfish's inertial force, written using Newton's Laws, and thus yields the following governing equation. Figure 2.3 gives a free body diagram of the forces involved in the jet propulsion swimming of a jellyfish.

$$\text{F}_{\text{inertia}} = \rho_w V_f \frac{du}{dt} = T - D + G$$

$$(1 + \alpha_{AM})\rho_w V_f \frac{du}{dt} = \frac{\rho_w}{A_V}\left(\frac{dV_f}{dt}\right)^2 - \frac{1}{2}C_d\rho_w S_A u^2$$

(2.11)
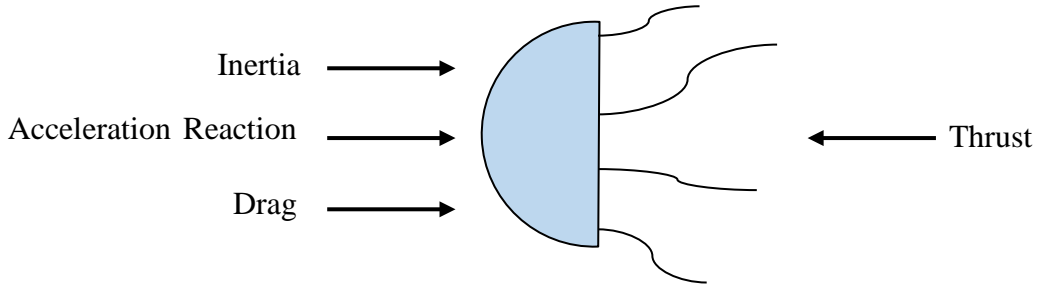
Figure 2.3 Free Body Diagram of Swimming Jellyfish
The inertial, acceleration reaction, and drag forces work against the thrust generation during the swimming cycle.

2.1.2. Modeling of Jellyfish Locomotion

A few points of discussion on the form of the governing equation are necessary prior to using it as a framework for soft robotics. First, it should be noted that the added mass coefficient used here is not applicable for geometries other than the hemiellipsoid shape assumed to define that of the biological jellyfish. Additionally, this component is normally defined in terms of an added mass tensor, which is highly dependent on surface geometry of an object and in some cases can be very complex to calculate [61,62].

Next, it is important to take note of the strong dependence of the acceleration on the rate of change in the volume. This will be seen to play a critical role in designing an efficient swimming mechanism through a careful balance of the contraction and relaxation phases that dictate the internal volume. The lack of body forces in the equation is also of interest. This restricts the model to horizontal swimming where gravity will not contribute to the acceleration. Lastly, these equations will necessarily need some modification to account for differences between the body of a jellyfish, and that of a soft robot. Later, as the design of the robot is thoroughly defined, these changes will be elaborated on in more detail.

The governing equation obtained in Equation (2.11) constitutes a first order nonhomogeneous nonlinear ODE in the variable u, and a second order ODE in the variable x defining the position. The solution of this equation is obtained numerically via a state-space representation and a 4th order Runge-Kutta method, as outlined next.

First, the equation is written in state-space form using two state variables, y_1 and y_2, which are defined as

$$\vec{y}(x,t) = \begin{Bmatrix} y_1(x,t) \\ y_2(x,t) \end{Bmatrix} = \begin{Bmatrix} x \\ \dot{x} \end{Bmatrix} = \begin{Bmatrix} x \\ u \end{Bmatrix} \tag{2.12}$$

where the overhead dot short hand notation for differentiation with respect to time has been used. With these state variables, Equation (2.11) can now be rewritten

$$\dot{\vec{y}} = \begin{Bmatrix} \dot{y}_1 \\ \dot{y}_2 \end{Bmatrix} = \begin{Bmatrix} y_2 \\ \dfrac{\dfrac{\rho_w}{A_V}\left(\dfrac{dV_f}{dt}\right)^2 - \dfrac{1}{2}C_d\rho_w S_A y_2^2}{(1+\alpha_{AM})\rho_w V_f} \end{Bmatrix} = f(\vec{y},t) \tag{2.13}$$

this allows both the position and velocity of the jellyfish to be integrated forward in time using any first order ODE solver. In this instance, a 4th order Runge-Kutta method (RK4) was used as

follows. Using the state space representation, the state at time $t_i + h_t$ can be written in terms of the state at the current time t_i with a weighted average of four increments

$$\vec{y}_{i+1} = \vec{y}_i + \frac{h_t}{6}(f_1 + 2f_2 + 2f_3 + f_4) \tag{2.14}$$

where h_t is the integrator time step and the terms in parenthesis are the increments that are estimations of the slope of the function being integrated, given by the following equations.

$$f_1 = f(\vec{y}_i, t_i) \tag{2.15}$$

$$f_2 = f\left(\vec{y}_i + \frac{1}{2}f_1, t_i + \frac{1}{2}h_t\right) \tag{2.16}$$

$$f_3 = f\left(\vec{y}_i + \frac{1}{2}f_2, t_i + \frac{1}{2}h_t\right) \tag{2.17}$$

$$f_4 = f(\vec{y}_i + f_3, t_i + h_t) \tag{2.18}$$

Then the acceleration of the jellyfish may be calculated by evaluating $\dot{y}_2$ at each time step.

As modeled in the literature, the volume rate of change is taken to be constant over both the contraction and relaxation phases. This can be achieved by defining a volume percentage change that should occur over these intervals, denoted dV, and calculating the rate of change over the interval as

$$\frac{dV_f}{dt} = \begin{cases} -\dfrac{dV}{t_c} & contraction \\ \dfrac{dV}{t_r} & relaxation \end{cases} \tag{2.19}$$

where t_c and t_r are the durations of the contraction and relaxation phases, respectively. This

gives the volume for the jellyfish as

$$V_f = \int_0^t \frac{dV_f}{dt} dt = V_0 + \begin{cases} -\dfrac{dV}{t_c} t_m & contraction \\ \dfrac{dV}{t_r}(t_m - t_c) & relaxation \end{cases} \tag{2.20}$$

for an initial volume of V_0 at the start of the contraction phase and t_m represents the time since

the last complete swimming cycle. For the jellyfish modeled in [58] the results shown in Figure

2.4 were obtained. As evident from the figure, the swimming mechanism of the jellyfish has a

characteristic oscillation due to the alternating contraction and relaxation phases. This behavior

is most easily seen in the velocity results but is also evident in the position and acceleration.

While somewhat difficult to see, the velocity also shows an asymptotic behavior as the thrust

slowly balances the drag and inertia forces to reach a steady-state average velocity.

A major take-away from these results is the negative acceleration created during the

relaxation phase of the swimming cycle. This is due to the mass-flux of water into the enclosed

volume of the jellyfish bell, causing a negative momentum exchange that pulls the jellyfish

backwards. If the contraction and relaxation phases were equal in time, it would be seen that the

momentum exchange during each cycle would identically cancel, and after each cycle the

jellyfish would return to a zero-velocity state. Thus, the relation between contraction and

relaxation times is a crucial aspect of efficient jet propulsive swimming and must be carefully

considered when designing a soft robot.
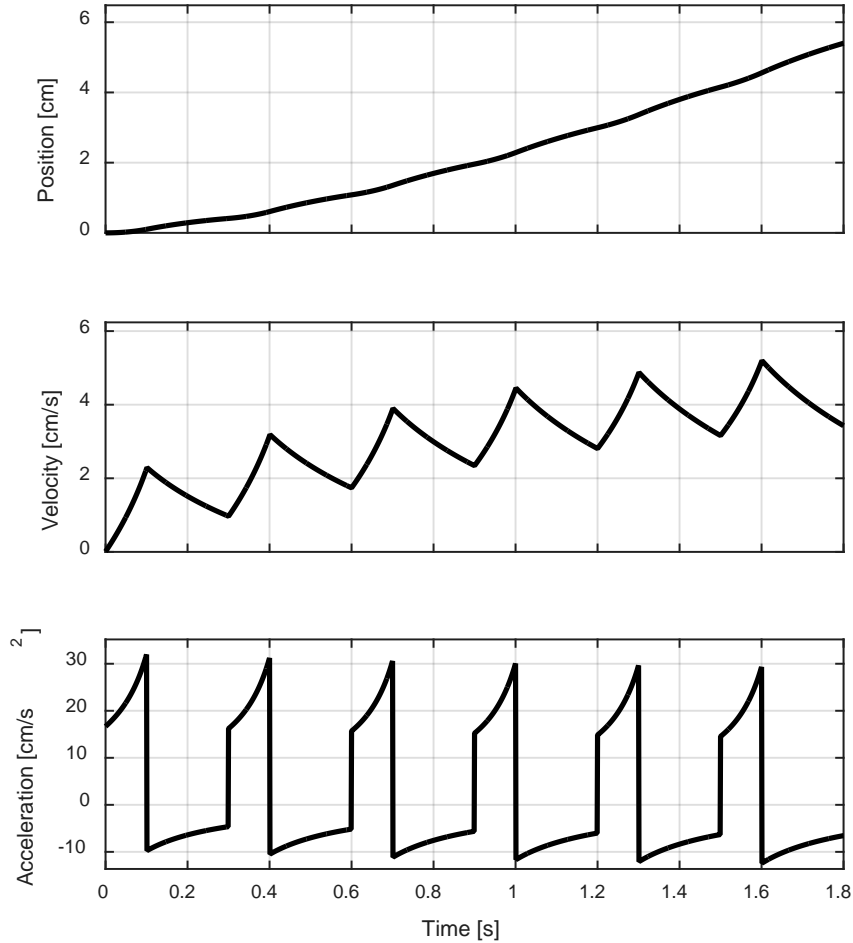
Figure 2.4 Position, Velocity, and Acceleration of Biological Jellyfish
The characteristic position, velocity, and acceleration profiles of a swimming jellyfish are recreated using the derived model, and can be compared to the results obtained in [58].

2.2. Design Principle of a Biomimetic Jellyfish

As noted previously, the jellyfish swimming mechanism has a disadvantage due to the intake of water during the relaxation phase. This causes a negative momentum exchange that pulls back on the animal, thus slowing it down. Here is where the proposed biomimetic robot seeks to modify the jet propulsion swimming mechanism. If the water that is drawn into the enclosed volume is redirected as to assist the propulsion of the device, then continual forward motion is achieved by an always increasing velocity until a steady-state is reached. This,

theoretically, should allow for a more efficient and effective swimming mechanism for a potential soft robot.

To achieve this necessary modification, the addition of a distinct inlet and outlet to the enclosed volume is proposed. During contraction, only the outlet valve allows fluid flow, thus constraining the direction of the mass flux and hence the momentum exchanged. Then, during relaxation, the inlet would allow for the mass flux to occur along the same direction, therefore contributing a positive acceleration. A simple illustrative cross-section of such a design is given in Figure 2.5. A soft robot utilizing this sort of structure may be deformed via EAP actuators, as will be elaborated on later.
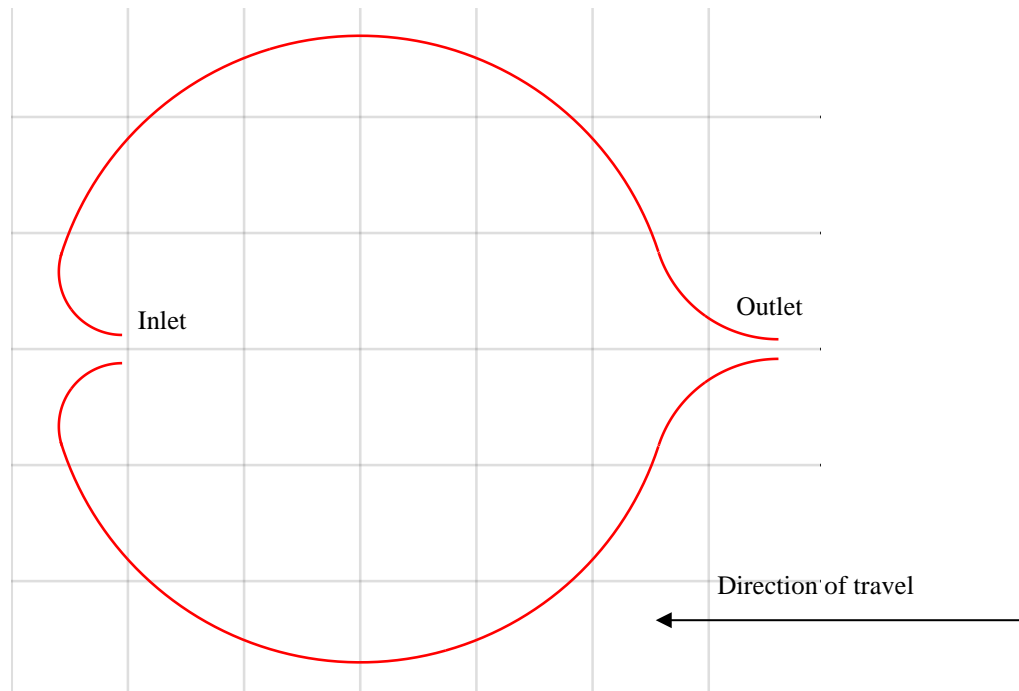
Figure 2.5 Illustrative Cross-Section of Proposed Soft Robot Design
The inlet and outlet valves illustrated here are intended to operate with a leaf-valve type mechanism wherein they allow fluid flow in only one direction.

Chapter 3. Electromechanical Modeling of Ionic Polymer-Metal Composite Actuators

The modeling and simulation of IPMC actuators is a rich and diverse research field. A general overview of the electrochemistry and electromechanical transduction of IPMCs can be found in [10,13,63–67], while a few of the many modeling techniques and approaches are seen in [3,6,10,12,68–72]. The electromechanical modeling of IPMC actuators presented here falls into two categories, physics-based and equivalent circuit. These approaches differ in both robustness as well as difficulty. Physics-based models typically utilize continuum mechanics equations to describe the electrochemical interactions within the polymer. Circuit models are found throughout literature as an alternative to physics-based models and have the advantage of simple implementation while providing adequate results for most modeling applications. In both cases, the actuation of the IPMC is related to the charge or charge density within the polymer through an electromechanical coupling equation, as in [12,73]. To develop soft robotic systems utilizing EAPs accurate models for their electromechanical transduction are critical.

3.1. Physics-Based Modeling

To construct a physics-based model of the IPMC electrochemistry, the Poisson-Nernst-Planck (PNP) system described in [12] and seen throughout literature [7,10,13,17,65,67,74–79]. The PNP equations can be used to describe an IPMC's cation concentration and electric potential as two scalar fields in space and time. Actuation is achieved by coupling the PNP equations with continuum equations describing the polymer deformation through an electromechanical coupling equation. Below, a derivation of the governing equations is given, and these equations will be used to model an IPMC actuator in COMSOL Multiphysics similar to what is described in [80].

3.1.1. Governing Partial Differential Equations

Following the procedure of [17,67,77,81], the electric potential distribution within the ionic polymer may be calculated by the Gauss Law

$$\nabla \cdot D_e = \rho_c \tag{3.1}$$

where D_e and ρ_c are the electric displacement and charge density within the polymer, respectively. The electric displacement can be related to the electric field strength, $\vec{E}$, as

$$D_e = \varepsilon \vec{E} \tag{3.2}$$

for a material with an absolute dielectric constant of ε. Combining Equation (3.1) and Equation (3.2), the electric potential within the polymer is found to be governed by the Poisson equation for electrostatics

$$\nabla \cdot \vec{E} = -\nabla^2 \phi = \frac{\rho_c}{\varepsilon} = \frac{F(c - c_0)}{\varepsilon_0 \varepsilon_r} \tag{3.3}$$

where ϕ, F, c, c_0, ε_0, and ε_r are the electric potential, Faraday's constant, mobile cation concentration, fixed anion concentration, dielectric constant in vacuum, and relative dielectric permittivity, respectively.

The electro-chemical model is completed by writing the mass balance equation for the mobile cation species in terms of the ion concentration time evolution and the cation flux within the polymer. This mass balance equation is written as

$$\frac{\partial c}{\partial t} = -\nabla \cdot J \tag{3.4}$$

for an ion flux within the polymer of J. Considering only migrative and diffusive flux components, the ion flux is related to the concentration and electric potential within the polymer through

$$J = -(D\nabla c + z\mu Fc\nabla\phi) \tag{3.5}$$

where D, z, and μ are diffusivity, charge number, and mobility of the ions, respectively. This is an extension of Fick's law that accounts for the migration of ions in an electric field. Flux associated with mechanical deformation of the polymer is neglected because it has been shown that during electromechanical transduction it is of much lower order than the migrative and diffusive components [80]. Substituting Equation (3.5) into Equation (3.4) we obtain the Nernst-Planck equation

$$\frac{\partial c}{\partial t} = \nabla \cdot (D\nabla c + z\mu Fc\nabla\phi) \tag{3.6}$$

which frequently arises throughout literature to determine the migration and diffusion of the free cations in IPMC.

Under an externally applied voltage, the free cations migrate towards the cathode while the anions remain fixed, which is defined via Equation (3.6). As the cations collect near the ion-blocking electrode, a non-zero net charge is formed which results in an electric field that opposes the applied one [75], governed by Equation (3.3). These two equations define a set of coupled partial differential equations known as the Poisson-Nernst-Planck system, and fully govern the electrochemical nature of the IPMC actuator.

Mechanical deformation of the actuator can be described using Newton's second law

$$\rho_m \frac{\partial \vec{u}}{\partial t} = \nabla \sigma + F_b \tag{3.7}$$

where $\vec{u}$, ρ_m, σ and F_b are the displacement field, material density, stress tensor, and body forces, respectively. The stress strain relationship can be written as

$$\sigma = C : \varepsilon_d \tag{3.8}$$

where C and ε_d are the stiffness tensor and strain tensor, respectively. The fourth order stiffness tensor retains the various material constants that describe the deformation behavior of the material. Here, linear elasticity is used which reduces the material constants to two elastic moduli, the Young's modulus and Poisson's ratio. Furthermore, to construct a simple model an assumption of infinitesimal strain is made resulting in the following strain displacement relation

$$\varepsilon_d = \frac{1}{2}(\nabla \vec{u} + (\nabla \vec{u})^T) \tag{3.9}$$

These equations dictate the mechanical deformation of the polymer when viewed as a continuum. During an electromechanical transduction, an additional equation is needed to couple the electrochemical behavior to the mechanical deformation of the IPMC actuator. From [12,17] the internal stress of the polymer as a function of the ionic charge density is written as

$$\sigma_{ext} = \alpha_h \rho_c + \beta_h \rho_c^2 \tag{3.10}$$

where α_h and β_h are electromechanical coupling coefficients. Due to the nature of IPMC actuation, wherein the hydrated mobile cations induce the bending behavior, these coefficients can be seen as hydrophilicity coefficients of the ions [79,82,83] as they directly correlate to the amount of water that travels with the free moving cations under the electrical input. The linear term is typically fitted to a small voltage step response, where the charge density is more symmetric and thus quadratic effects are not as prominent. The quadratic term is then used to correct the linear model at larger voltage inputs [17]. This external stress can then be added to the material stress tensor to provide the necessary electromechanical coupling that governs the IPMC actuation. When Newton's EoM are solved for the mechanical deformation, the material stress tensor accounts for the body's elastic response to the external loading while the external stress calculated with Equation (3.10).

3.1.2. Multi-Physics Modeling in COMSOL

Due to the highly nonlinear nature of the PNP system, as well as the equations of elasticity, many scholars commonly employ the finite element method [7,12,65,74–77,79,80,84,85]. Here, COMSOL Multiphysics is used to solve the described equations.

When attempting to solve the PNP system analytically it is common to see the equations be reduced to a single spatial dimension to obtain a solution more easily [8,9,67–69,74]. This is normally justified by noting that the cation migration within the polymer generates a charge density and electric potential that is virtually constant in the length and width directions, so the equations are solved along the thickness of the IPMC only. While this is not as common in numerical modeling when using commercial software such as COMSOL Multiphysics, it is just

18

as justified and leads to smaller stiffness matrices and faster computation, as will be

demonstrated next. The approach is similar to what has been recently seen in [72].

In COMSOL, the Multiphysics module of Transport of Diluted Species with migration in

electric field is used to model the Nernst-Planck equation, Electric Currents is used to solve for

the electric potential in the electrodes, and a general form PDE module calculates the Poisson

equation for the electrostatics within the ionic polymer. As with many models, a cantilever

configuration is used; a schematic of which is shown in Figure 3.1 below.
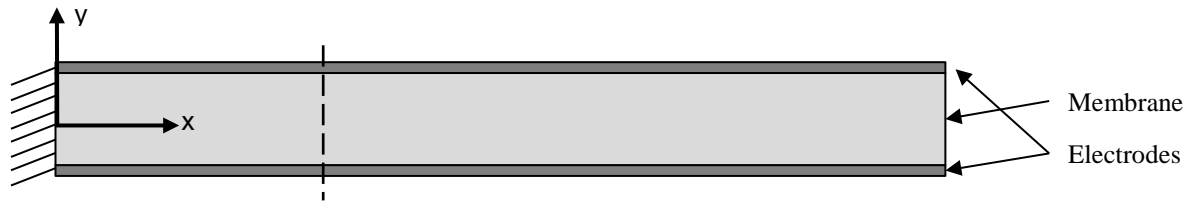
Figure 3.1 Cantilever IPMC Diagram for COMSOL Multiphysics Modeling
Thickness of both the polymer membrane and the metallic electrodes have been exaggerated here
for illustrative purposes. The cantilever configuration is commonly used throughout literature for
modeling IPMC actuators and serves as a good baseline model for verification.

The governing PDEs are solved along the y-axis seen in Figure 3.1, where the dashed line

is an arbitrary representative slice along this direction. This reduction in dimensionality leads to

a smaller computational domain in COMSOL, shown in Figure 3.2, where only the through the

thickness profiles for concentration and electric potential are calculated. To verify the validity of

this approach, a comparable model to that found in [80] was created. Both models utilize the

same mesh density, 5000 elements, along the thickness of the membrane and simulate an IPMC

with the parameters found in Table 3.1. In contrast to Equation (3.10), this model uses an

electromechanical coupling equation found in [80,86] of the form

$$F = \alpha_c \rho_c \tag{3.11}$$

19

where the coupling is now between the charge density and an external force, and only the linear

term has been retained, as in [80]. Later the original form of Equation (3.10) will be used, but for

consistency with [80] this equation has been chosen for now.
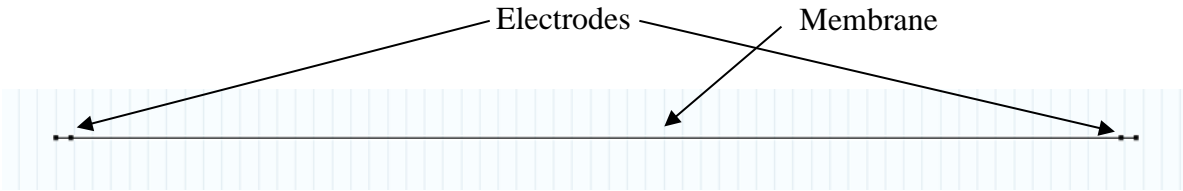
Figure 3.2 COMSOL Domain for 1D PNP FEM
The COMSOL domain shown consists of two small domains that model the electrical current
within the electrodes, and a larger domain which models the PNP equation along the thickness of
the IPMC.

Table 3.1 Model parameters for 2D vs 1D PNP Comparison

Parameter	Value
Width (mm)	9.94
Length (mm)	51.07
Thickness, Polymer (mm)	0.57
Thickness, Electrodes (mm)	0.08
Diffusion Coefficient (m^2/s)	7e-11
Permittivity (mF/m)	2
Anion Concentration (mol/m^3)	1,200
Poisson Ratio (1)	0.49
Young's Modulus (MPa)	249
Density (kg/m^3)	2,000
α_c (N/C)	2e-5

A 2D domain is then used to calculate the mechanical deformation of the IPMC based on

the results of the 1D PNP simulation. The domain is shown in Figure 3.3, where it is important to

note that the vertical y-axis has its zero-line at the lower polymer-electrode interface. More

detailed views of the COMSOL domains and meshes can be found in Appendix A.

Figure 3.3 Domain for 2D Solid Mechanics in COMSOL
The COMSOL domain used in the calculation of the mechanical deformation under the
electromechanical transduction of the IPMC.

The cation concentration, charge density, and electric potential calculated on the 1D

domain must be mapped to the 2D domain to calculate the electromechanical transduction. In

this model, the coupling is one-way, and mechanical deformation has no effect on the anion

concentration and hence the charge density. This has been shown to be acceptable for actuation

type transduction [80]. To link the 1D and 2D domains, a general extrusion operator is used to

map the 1D domain through a mathematical equation defining the geometry of the 2D domain.

For the simple case of a cantilever IPMC, this can be written as

$$x_i - t_e = y \tag{3.12}$$

where x_i, t_e, and y are the x-axis variable in the 1D domain, thickness of the electrode, and y-

axis variable in the 2D domain, respectively. This equation maps all values obtained in the 1D

PNP to their respective location in the 2D geometry along the thickness direction of the polymer

membrane. The subtraction of the electrode thickness is necessary to ensure that both x_i and y

start at zero at the lower polymer-electrode interface.

The comparison of the 1D and 2D COMSOL results can be seen in Figure 3.4, where it is

evident that both solutions are in very good agreement. The maximum difference between the

results occurs at approximately 4.65 seconds and yields a percent error of only 0.31%, thus

21

verifying the accuracy of the new approach. A few metrics for evaluating the efficiency of the model are given in Table 3.2, where the key result is the computation time. In using a 1D approach for the PNP system, the time required to obtain the results shown was reduced by a factor of ~23, which is a dramatic improvement. This can be further improved upon by leveraging the fact that charge density and concentration and potential gradients along the thickness direction are virtually negligible.
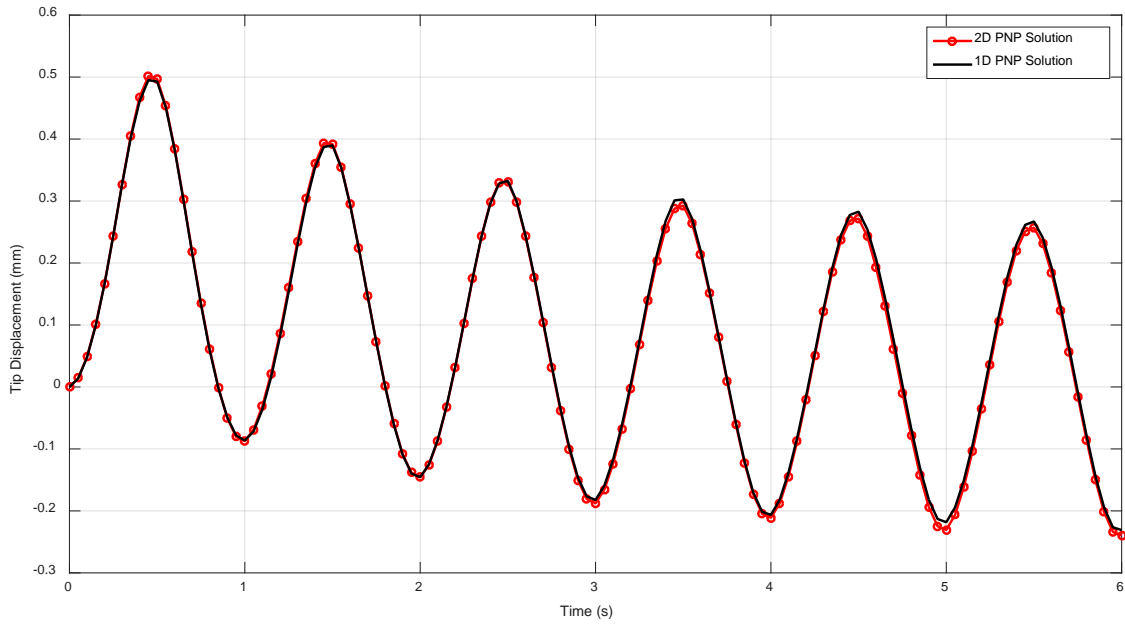
Figure 3.4 Comparison of 1D and 2D PNP Models
The comparison between 1D and 2D PNP solutions shown highlights the value in using a reduced dimensionality domain for the computation of the complicated PDE system.

Table 3.2 Metrics for 1D vs 2D PNP Comparison

Parameter	1D PNP	2D PNP
Time step (s)	0.1	0.1
Sim. Time (s)	6	6
DoF (1)	51,780	329,119
Comp. Time (s)	102	2,308

22

A modification is made to address this behavior of the PNP solution in these problems. Specifically, the membrane domain is partitioned into three segments, two located at each of the polymer-electrode interfaces, and one in the middle constituting the bulk of the membrane. The exterior partitions, referred to as buffer regions, are meshed with a higher mesh density than the bulk region, while the overall element count is reduced. Mesh reduction is conducted until the results would rise above a 0.1% change. This allows the 1D model to capture the steep gradients located in the buffer regions more easily, while not wasting computational resources in the bulk of the polymer where gradients are small. A schematic comparison of the two domains is given in Figure 3.5.
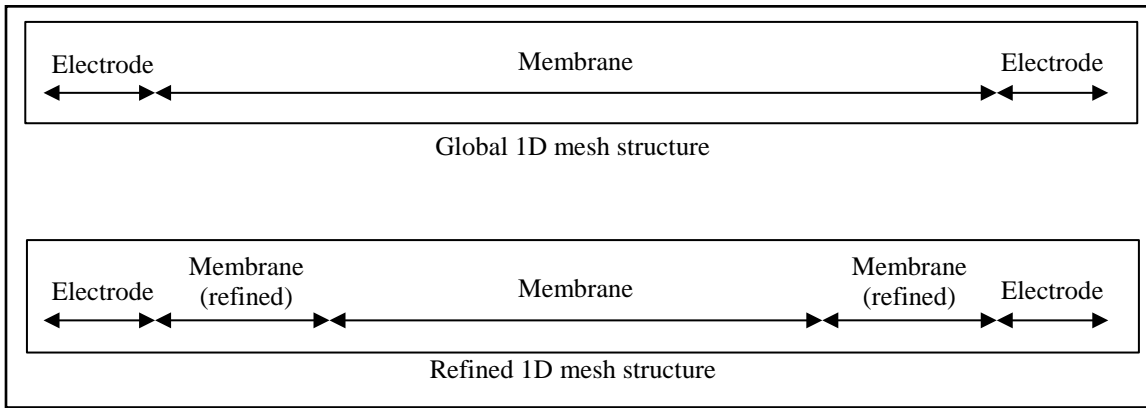
Figure 3.5 Differences in 1D Domain Structures Used in COMSOL
The refined domain uses insight into the nature of the PNP system, wherein large concentration gradients arise near the electrode polymer interface and within the bulk polymer the concentration is near constant. This is most clearly demonstrated in [67].

With the newly refined domain, further reduction in computational overhead is achieved without loss of accuracy, as demonstrated in Figure 3.6, again with some of the metrics for comparison given in Table 3.3. Of importance to note is the reduction in computation time by another factor of 2, as well as the refinement in temporal accuracy from a timestep of 0.1 to 0.01 seconds. Displacement is accurate within 4% error between the two results and is further reduced

23

with increased mesh density within the refined regions of the new domain. This increase in the time resolution allows for more accurate simulations in time while still requiring minimal computational efforts and demonstrates an advancement in the modeling procedures for IPMC based system. This potentially allows for more complex and dynamic soft robotics to be modeled with full IPMC physics included.
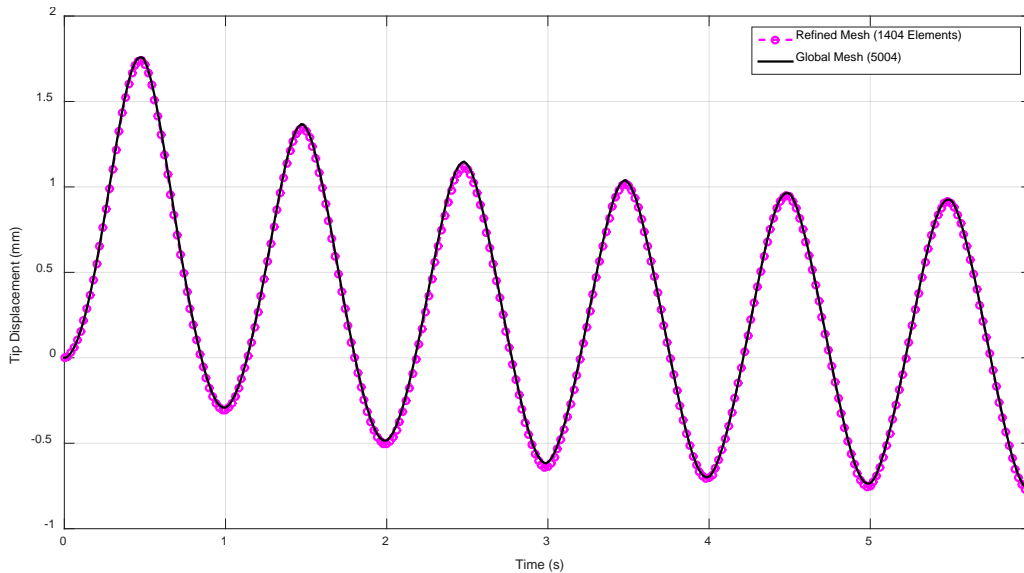
Figure 3.6 Comparison of 1D and Refined 1D PNP Models
Here the comparison between the refined mesh with buffer regions near the electrode polymer interface and the globally meshed domain is provided, again highlighting the accuracy obtained when using the more efficient mesh and domain structure.

Table 3.3 Metrics for 1D vs Refined 1D PNP Comparison

Parameter	1D PNP	Refined 1D PNP
Time step (s)	0.01	0.01
Sim. Time (s)	6	6
DoF (1)	51,780	30,180
Comp. Time (s)	174	90

24

Upon examination of this model, it is clear that the use of a boundary load as in [80] will not work in all circumstances. For instance, in the case of an unconstrained IPMC, the boundary load would result in an unconstrained force resulting in constant rigid body acceleration of the IPMC, which is obviously unreasonable. To remedy this, the external stress physics was added into the material model in COMSOL. This allows for an electromechanical coupling equation of the form in Equation (3.10) to be used, and results in no rigid body acceleration when modeled as an unconstrained IPMC. This is illustrated in Figure 3.7, where an IPMC was given a step response in an unconstrained state and deforms as expected.
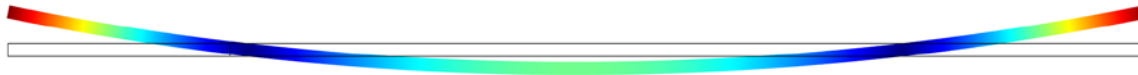
Figure 3.7 Unconstrained IPMC Deformation Under External Stress Loading
With a boundary load applied to the IPMC model, an unconstrained actuator would see an unbalanced force and experience rigid body motion. The alternative external stress electromechanical coupling fixes these issues, as demonstrated in this figure.

The refined 1D PNP model has been compared to experimental actuation results from an IPMC made with off-the-shelf Nafion®. A plot of the actuation results is seen in Figure 3.8, and Table 3.4 contains the physical dimensions and electromechanical coupling coefficient used to obtain these results. From the figure, it is clearly seen that the COMSOL model can accurately capture the performance of the physical IPMC in the steady-state, while the initial transient portion is not quite as good. The phase-lag between the results is a result of the experimental data being captured not quite at the instant the actuation started and is not due to any missing physics in the COMSOL model.
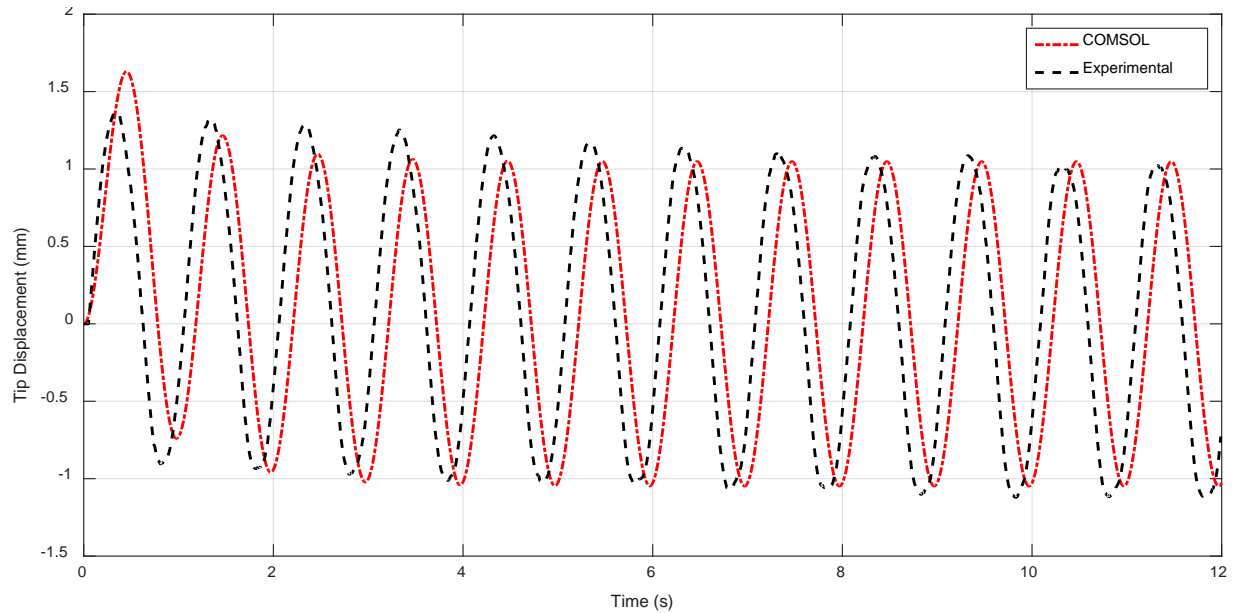
Figure 3.8 Comparison Between Refined 1D COMSOL Model and Experimental Data
The described IPMC model is shown to give good results when compared to a physical IPMC
actuator and the collected experimental deformation.

Table 3.4 Parameters and Dimensions of IPMC Used for Experimental Comparison

Parameter	Value
Length (mm)	45.08
Width (mm)	11.57
Thickness (mm)	0.67
Diffusion Coefficient (m^2/s) *	7e-11
α_c (N/C) *	2e-5
Voltage (V)	1
Frequency (Hz)	1

* Denotes an assumed value for the simulated model obtained from literature [80].

3.2. Equivalent Circuit Modeling

Throughout literature, the use of an equivalent circuit representation for electrochemical

nature of IPMCs has been used to provide a simple, relatively accurate model that is easily

incorporated into soft robotics research [67,70,87–89]. Electrochemical transduction is modeled

26

using lumped circuit components, which can be determine both experimentally [88], or through the linearization of an analytical solution to the PNP system in order to explore the sources of the lumped impedance values from a physics standpoint [78]. The benefits of using a circuit-based model is that closed form solutions can be easily obtained for a variety of external potential inputs and the IPMC response to such inputs can be easily combined into models of physical devices. This requires no computational overhead, as compared to a finite element method approach that may give more accurate and meaningful results. The interest in investigating the equivalent circuit model is primarily for its ease of incorporation into other models of soft robotic systems using IPMC actuators.

3.2.1. RCW Circuit Model

Similar to [14,78], a circuit model that incorporates resistive, capacitive, and Warburg (RCW) impedances is used. These impedances model the surface and polymer resistance, inherent polymer capacitance and double layer capacitance due to cation migration, and charge transfer and diffusion within the polymer [78,90], respectively. A diagram of this circuit is provided in Figure 3.9.
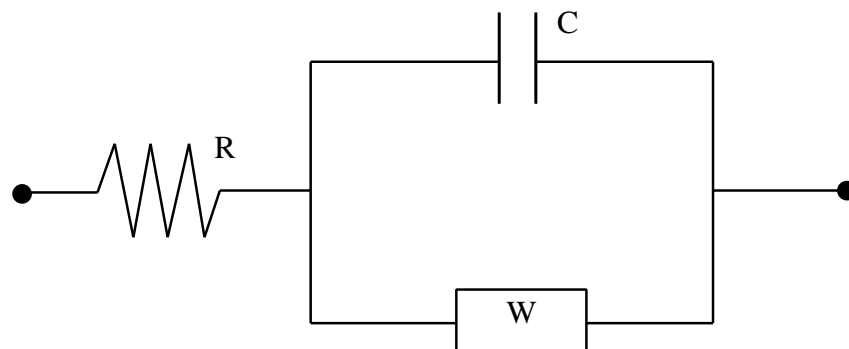
Figure 3.9 Circuit Diagram Used for Equivalent Circuit IPMC Model
The shown circuit diagram can be used to construct an accurate model for the electromechanical transduction of IPMC actuators.

The electrical impedance of each of these lumped circuit elements is written below, where R, C, and W are the lumped electrical resistance, lumped capacitance, and Warburg impedance, respectively

$$Z_R = R \tag{3.13}$$

$$Z_{Cap} = \frac{1}{j\omega C} \tag{3.14}$$

$$Z_{Warburg} = \frac{W}{\sqrt{j\omega}} \tag{3.15}$$

A transfer function may be written between an input voltage and the respective current generated through the circuit [78].

$$H(s) = \frac{I(s)}{V(s)} = \frac{Cs + W\sqrt{s}}{RCs + RW\sqrt{s} + 1} \tag{3.16}$$

Akin to Equation (3.10), an electromechanical coupling equation can be written in the following form [73]

$$P = \alpha_{RCW} Q \tag{3.17}$$

where P, α_{RCW}, and Q are the mechanical loading of the IPMC, electromechanical coupling coefficient, and total charge within the polymer, respectively. The actuation response of an IPMC under the RCW circuit model can then be obtained from the current via

$$Q(t) = \int_0^t i(\tau)d\tau = \mathcal{L}^{-1}\left\{\frac{1}{s}I(s)\right\} = \mathcal{L}^{-1}\left\{\frac{1}{s}H(s)\mathcal{L}\{V_{ext}(t)\}\right\} \tag{3.18}$$

where $i(t)$ is the electrical current through the circuit, $V_{ext}(t)$ is an externally applied voltage, and $\mathcal{L}$ is the Laplace transform operator and an assumption of zero initial current was made.

A physics-based model for the impedances used in the RCW circuit is found in [78], which gives a starting point for finding the correct parameters that fit the model to physical IPMC actuators. Here, the parameters were manually tuned from the baseline given by the physics-based model to arrive at suitable values to compare this model approach to that of COMSOL and to the experimental data collected from the physical IPMC. The parameter values used are given below in Table 3.5.

Table 3.5 Parameter Values for Equivalent Circuit Model

Parameter	Value
R (Ohm)	3.21
C (mF)	1.62
W (1/Ohm*s^2)	5e-1
α_{RCW} (N/C*m^2)	2.55

Using the parameters given in Table 3.5, the circuit model was compared to the same experimental data as the physics-based COMSOL FEM model. A quasi-static linear beam equation was used with a distributed load calculated using Equation (3.17). More details on the beam theory equation used are given in 4.3.1. The results of the comparison can be seen in Figure 3.10, where again there is a good agreement of the circuit model to the experimental displacement. The input voltage and frequency for the model are the same as those found in Table 3.4. When using different physical IPMC samples, a tuning process will be necessary to capture the exact behavior of the sample's electrochemical nature. Nevertheless, this approach is attractive due to the simplified mathematics behind it, and its ease of implementation as a component of a larger, more complex model, as will be discussed in the next section.

29
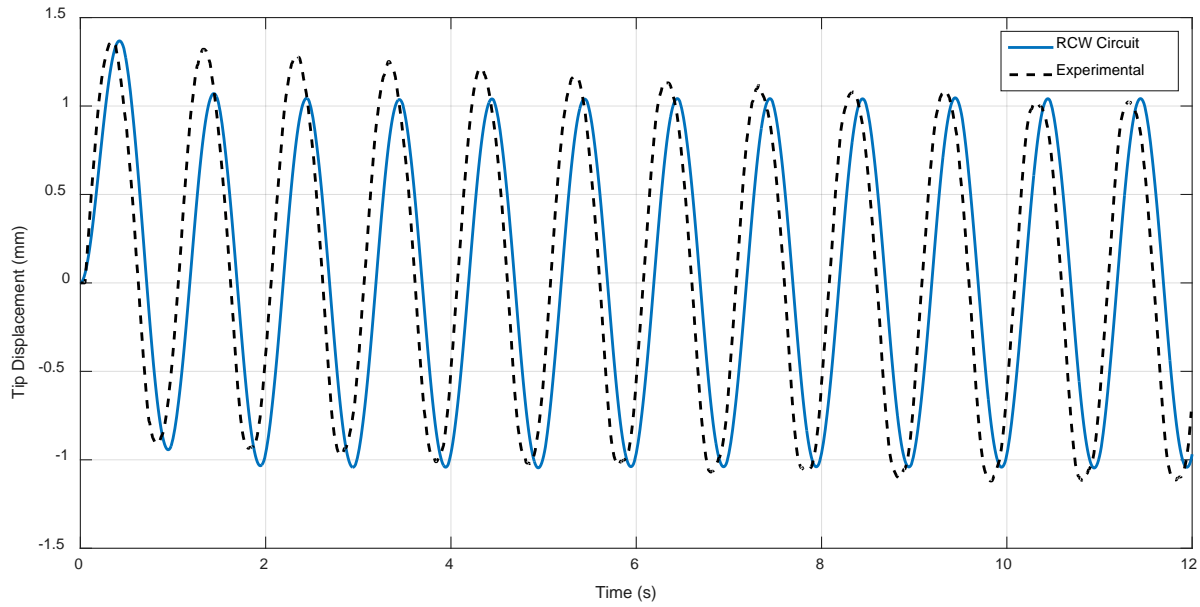
Figure 3.10 Comparison Between RCW Circuit Model and Experimental Data
Like the COMSOL model, the described equivalent circuit model shows good agreement with
the experimental data collected from a physical IPMC actuator.

3.3. Comparison and Utility of Modeling Approaches

The final question regarding the two modeling approaches seen is which to use in the

development of the proposed robot design. For obvious reasons, the physics-based finite element

approach taken in COMSOL is the more accurate technique. Following the work in [67], a non-

dimensional form illustrates that at the scales involved in IPMC applications the PNP system is a

singularly perturbed equation and has boundary layer effects at both polymer-electrode

interfaces. The FEM approach is capable of accurately capturing the complex electrochemistry

occurring within the ionic polymer and is adaptable for any kind of material model or

electromechanical coupling. While the advantages of a highly accurate model are numerous, the

FEM implementation within an external package such as COMSOL does not lend itself to be

combined in conjunction with other modeling techniques to simulate entire robotic systems. This

is where the circuit-based model becomes attractive.

30

The physical basis for the circuit model is not as sound as the direct solution obtained via FEM, but there are many methods for determining suitable parameters [3,35,70,73,88,91,92] for a simple circuit model that yields accurate electromechanical transduction results for a given IPMC. Furthermore, the circuit model is easily integrated into larger modeling approaches, which will be the focus of Chapter 4.3.3, and gives researchers more flexibility with how the mechanical deformation of the IPMC is solved. For these reasons, the circuit model will be used for including the electromechanical effects of the IPMCs used in the proposed soft robot design. One final comparison between both methods and the experimental data is given in Figure 3.11 for a comprehensive comparison and conclusion of the discussion in this chapter.
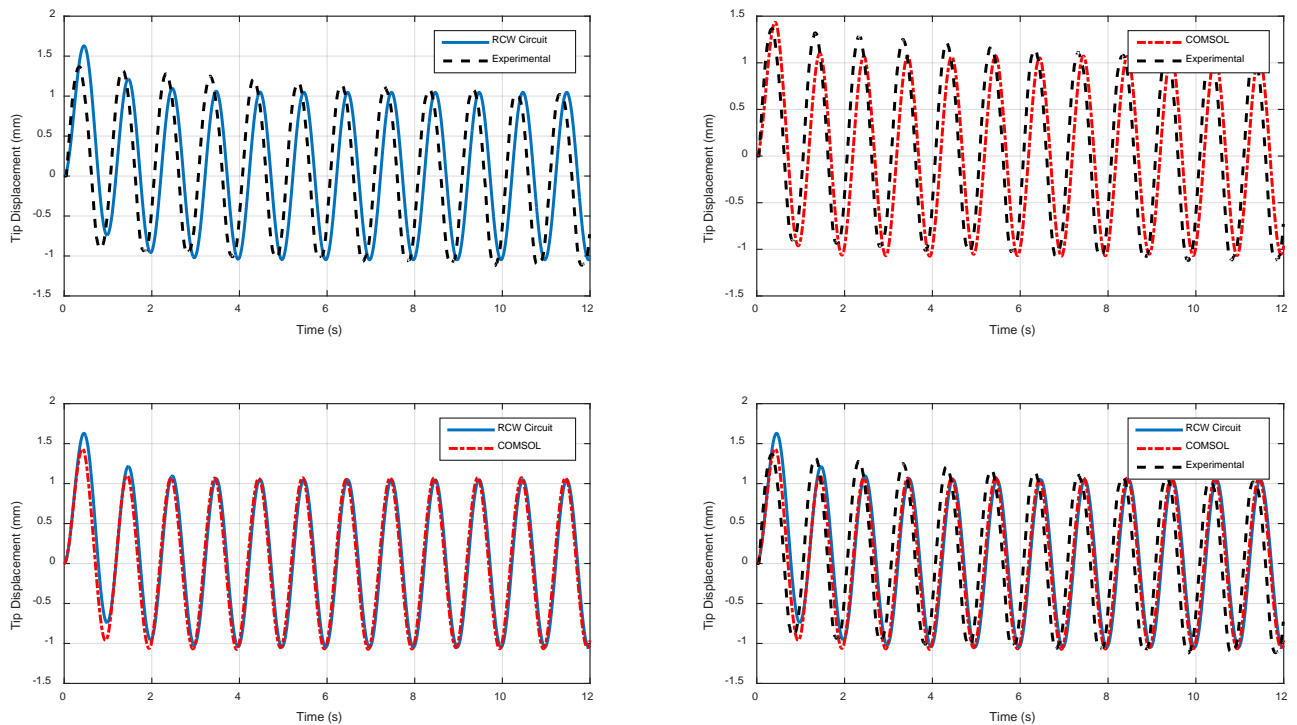
Figure 3.11 Comparison of FEM, Equivalent Circuit, and Experimental IPMC Deflection
Here, all pair-wise comparisons between the two described models as the experimental data are provided for compactness.

Chapter 4. Modeling of a Biomimetic Soft Robot

Prior to constructing any models of the biomimetic soft robot shown in Chapter 2, the governing EoM must be modified to account for the differences between biological jellyfish and the proposed design. To model the soft robot design proposed in Chapter 2, two different approaches are taken. A preliminary model is constructed that considers the body of the robot as a geometric surface, and that the body retains this geometric description throughout the deformation process. The necessary derivations for the deformation, volume, and surface area are described and the model is compared to an equivalently sized biological jellyfish. This model is primarily used as a proof of concept of the robot design and demonstrates the feasibility of such a robot. The second model expands the concept and spirit of the first through an implementation of beam theory to ground the mechanical deformation of the robot body within solid mechanics. Further derivations are given for the pertinent parameters seen in EoM, and the equivalent circuit model for IPMCs is coupled with the beam theory implementation to model the electro-chemo-mechanical behavior of the final robot.

4.1. Governing Equation and Model Inputs

In deriving Equation (2.11), an assumption was made that the body of a jellyfish is approximately the same density as water. This assumption is no longer universally valid for all constructions of the biomimetic robot as the material used to construct the body of the device may vary in density. To remedy this, the mass of the robot is split into a persistent mass that encompasses the materials that make up the shell of the body and the mass of water contained within the robot. Furthermore, the added mass is an effect that occurs on the external interface with the water, and as such its effect should be based on the external volume of the robot shell.

32

This differentiation between internal and external volume amounts to accounting for the thickness of the material that is used to construct the robot.

Lastly, to model the effect of having directional control over the inlet and outlet of water, the direction cosine of the outlet/inlet vector is included, as illustrated in Figure 4.1. This comes with an assumption that these outlet/inlet locations are symmetric about the direction of travel. For example, an inlet located perpendicular to the swimming direction would allow for the internal volume to refill but would not contribute any acceleration to the robot, while an inlet directed in the direction of swimming would allow for water intake and contribute a positive acceleration to the robot. This simple addition allows for the robot to have better control over its velocity profile during swimming and will be shown to be more effective than the swimming mechanism of biological jellyfish.

The modified EoM can now be written as

$$(m_b + \rho_w V_i + \alpha_{AM}\rho_w V_o)\frac{du}{dt} = \cos(\theta)\frac{\rho_w}{A_V}\left(\frac{dV_i}{dt}\right)^2 - \frac{1}{2}C_d\rho_w S_A u^2 \qquad (4.1)$$

where m_b is the mass of the robot body assumed to be fixed with a density not equal to water, V_i is the internal fluid volume, V_o is the external volume of the body, and $\cos(\theta)$ is the direction cosine illustrated in Figure 4.1. These modifications are necessary to capture a more accurate swimming behavior of the proposed robot.
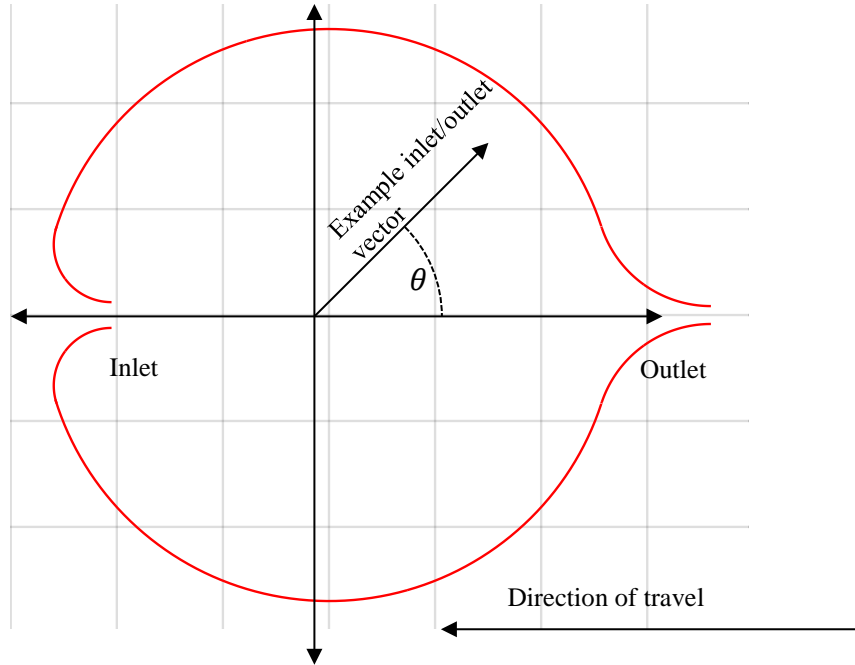
Figure 4.1 Illustration of Direction Cosine for Inlet and Outlet Valves
The direction cosine of an inlet or outlet for the proposed design is based off the polar angle
starting on the positive x-axis and trending positive counterclockwise.

In the modeling of biological jellyfish, the change in volume was assumed to be constant

during the contraction and relaxation phase with a distinct rate during each phase. In anticipation

of using an EAP actuator for the final model, a similar input source is constructed that can be

used to mimic this kind of behavior. Here, a variable amplitude and duty cycle square wave is

used as an input. This both serves to define the rate of change in volume for the original jellyfish

model, as well as model an electric potential input that could be created with a function

generator. This waveform was constructed via the Fourier series given below

$$
\begin{aligned}
F(t) = {} & \frac{At_c + Bt_r}{t_c + t_r} \\
& + \sum_{n=1}^{\infty} \frac{A - B}{n\pi} \left[sin\left(\frac{2n\pi}{t_c + t_r} t_c\right) cos\left(\frac{2n\pi}{t_c + t_r} t\right) \right. \\
& \left. + \left(1 - cos\left(\frac{2n\pi}{t_c + t_r} t_c\right)\right) sin\left(\frac{2n\pi}{t_c + t_r} t\right) \right]
\end{aligned}
\tag{4.2}
$$

where A and B are the contraction and relaxation phase amplitudes, respectively. An example of the waveforms generated by the 3rd, 10th, and 1,000th partial sums of the Fourier series is given in Figure 4.2. As demonstrated in the figure, the series can construct a square wave of varying duty cycle with distinct amplitudes during each phase in a given cycle. This will be a very important feature that is leveraged in both models further on. Later it will become relevant to references the time ratio of relaxation time to contraction time, so it will be defined below.

$$\delta_t = \frac{t_r}{t_c} \tag{4.3}$$
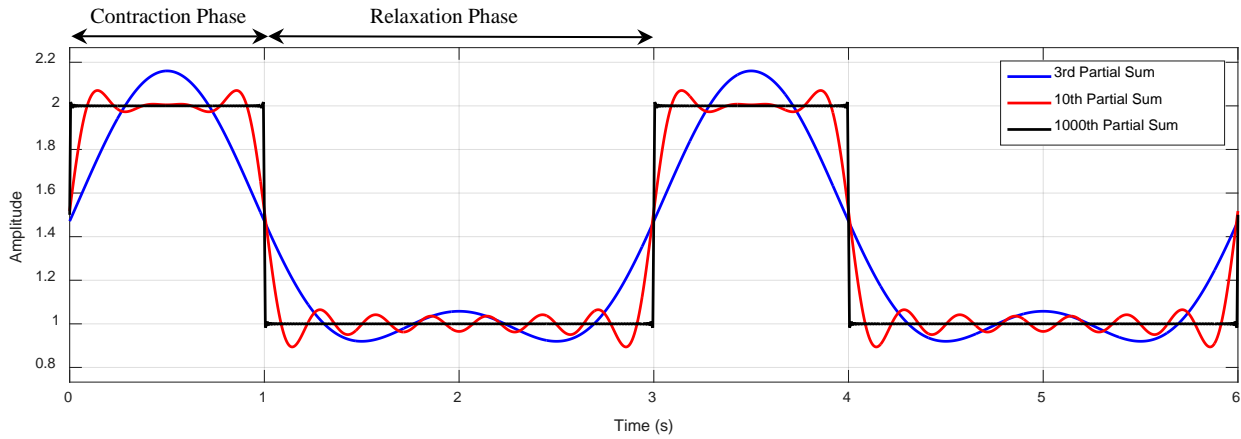
Figure 4.2 Representative Waveforms Generated with Fourier Series Square Wave
The characteristic contraction and relaxation phases of the jellyfish can be captured by the Fourier series shown here.

4.2. Geometry Based Modeling

4.2.1. Description of Robot Body as Geometric Surface

As discussed at the beginning of the chapter, this first modeling approach describes the body of the robot as a geometric surface. Specifically, the shell of the robot is defined as an ellipsoid with half-axis dimensions a, b, and c as illustrated in Figure 4.3. This simplified geometric approach is mainly used as a proof of concept and feasibility study, while also helping

35

aid in determining what parameters might play important roles in more robust and physics-based modeling approaches. A constraint is placed on the model that all deformed states of the body can be described though the definition of an ellipsoid, given by the well-known equation

$$\left(\frac{x}{c}\right)^2 + \left(\frac{y}{b}\right)^2 + \left(\frac{z}{a}\right)^2 = 1 \tag{4.4}$$
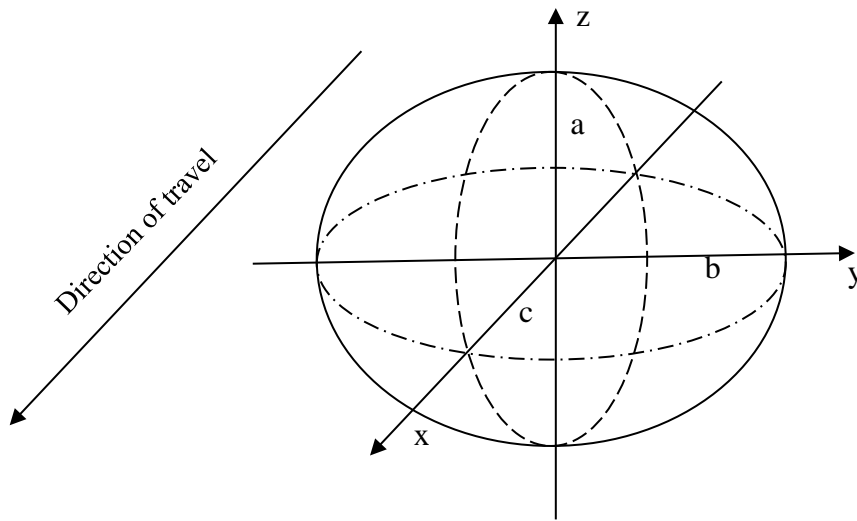
Figure 4.3 Geometric Description of Robot Body as an Ellipsoid
The body of the robot can be approximated as an ellipsoid for initial feasibility study of the proposed design.

4.2.2. Derivation of Model Parameters

To use a geometric approach for modeling the biomimetic robot, the volume, deformation of the volume, cross-sectional area, drag, and added mass effects must be determined. The internal volume of the given ellipsoid is calculated with Equation (4.5), and, with an added wall thickness of d, the external volume with Equation (4.6) below.

$$V_i = \frac{4}{3}\pi abc \tag{4.5}$$

$$V_o = \frac{4}{3}\pi(a + d)(b + d)(c + d) \tag{4.6}$$

The time rate of change for the internal and external volume are obtained

$$\frac{dV_i}{dt} = \frac{4}{3}\pi\left(\frac{da}{dt}bc + a\frac{db}{dt}c + ab\frac{dc}{dt}\right) \tag{4.7}$$

$$\frac{dV_o}{dt} = \frac{4}{3}\pi\left((b + d)(c + d)\frac{da}{dt} + (a + d)(c + d)\frac{db}{dt} + (a + d)(b + d)\frac{dc}{dt}\right) \tag{4.8}$$

where the half-axis dimensions of a, b, and c are all able to vary with time. Now conservation of mass with respect to the body of the device can be written as

$$\frac{dm_b}{dt} = \frac{d(\rho_b V_b)}{dt} = \rho_b\frac{d(V_o - V_i)}{dt} = \rho_b\left(\frac{dV_o}{dt} - \frac{dV_i}{dt}\right) = 0 \tag{4.9}$$

where ρ_b is the density of the material that makes up the body of the robot. Assuming the input to the device will cause a deformation of the half-axis dimension a, and that the corresponding deformation will be symmetric about the z-axis, a constraint is enforced with the equation below.

$$b(t) = c(t) \tag{4.10}$$

Now, using Equation (4.10) along with the conservation of mass Equation (4.9), the rate of change of b and c are obtained as functions of the input deformation in a, as shown below.

$$b\frac{db}{dt} = \frac{dc}{dt} = -\frac{2b + d}{2(a + b + d)}\frac{da}{dt} \tag{4.11}$$

The cross-sectional area with respect to the swimming direction can be calculated based on the external volume

$$S_A = \frac{3V_o}{4(c+d)} \tag{4.12}$$

Extending from the drag coefficient formulation seen in Equation (2.7), the formulation found in [93] is used. This allows for a wide range of Reynold's numbers, 10^{-1} to 10^6, but still assumes a spherical body, which will introduce small errors into the model. A plot of this drag coefficient is provided in Figure 4.4.Overall though, the results should be accurate enough for a first approximation and feasibility study.

$$C_d = \frac{24}{Re} + \frac{2.6\frac{Re}{5.0}}{1 + \left(\frac{Re}{5.0}\right)^{1.52}} + \frac{0.411\left(\frac{Re}{263000}\right)^{-7.94}}{1 + \left(\frac{Re}{263000}\right)^{-8.00}} + \frac{0.25\frac{Re}{10^6}}{1 + \frac{Re}{10^6}} \tag{4.13}$$

Finally, the added mass coefficient for an ellipsoid body is found using [94]:

$$A_0 = abc \int_0^\infty \frac{du}{(c^2+u)\sqrt{(a^2+u)(b^2+u)(c^2+u)}}, \quad \alpha_{AM} = \frac{A_0}{2 - A_0} \tag{4.14}$$

With these parameters fully defined, the EoM given in Equation (4.1) can be used to simulate the biomimetic robot swimming.
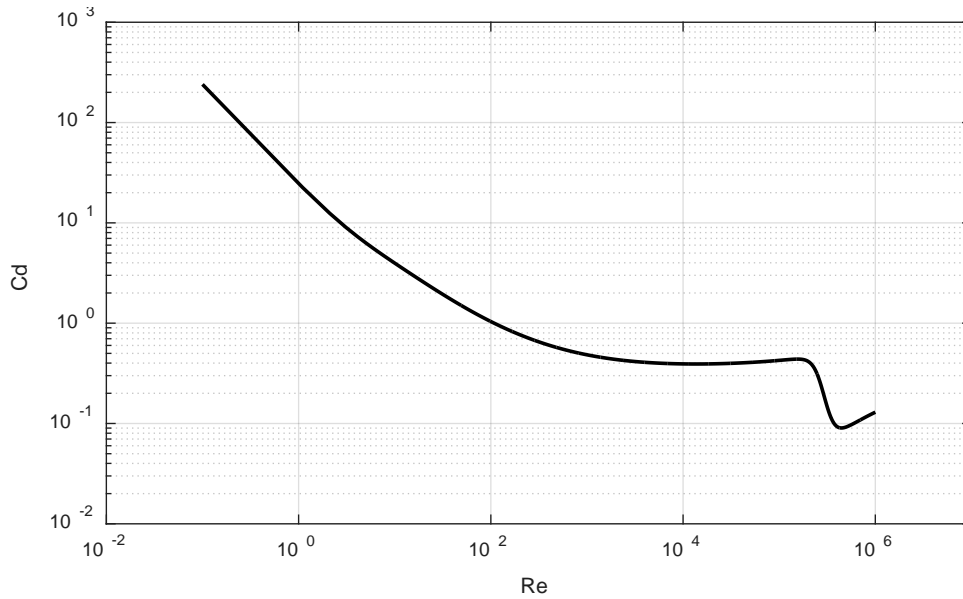
Figure 4.4 Drag Coefficient as a Function of Reynold's Number
The drag coefficient correlation given in Equation (4.13) is valid over a large range of Reynold's numbers, as shown here.

4.2.3. Comparison to Biological Jellyfish

In the proposed model, the biomimetic robot has a forward-facing inlet that, under ideal circumstances, allows for unidirectional mass flow through the body of the robot, which will be referenced as the P1 swimming mode. This effect manifests itself in the direction cosine term in Equation (4.1). A side effect of allowing this kind of control is that the model can be used to simulate a jellyfish, P2, mode, in which the inlet is directed rearward, simulating the familiar swimming characteristics seen in Figure 2.4. The direction cosine angle for each swimming mode is given in Table 4.1.

Table 4.1 Direction Cosine Angles for Inlet and Outlet During Different Swimming Modes

	Propulsion Mode 1 (P1)	Propulsion Mode 2 (P2)
Inlet	$\theta = 0$	$\theta = \pi$
Outlet	$\theta = 0$	$\theta = 0$

As an input to the geometric model, the rate of change of the half-axis dimension a is defined through the Fourier series found in Equation (4.2). A constraint is placed on the magnitude of the contraction and relaxation amplitudes that ensures that after one complete swimming cycle the volume returns to its initial state. This is written as

$$B = -\frac{t_c}{t_r}A \qquad (4.15)$$

For an input rate of change to a of -0.3 cm/s, the half-axis dimension varies in time as shown in Figure 4.5, where it is clear that the rate of change in the half-axis dimension is constant throughout both the contraction and relaxation phases, and the constraint given by Equation (4.15) forces the dimensions of the shell to return to their initial state after each cycle.
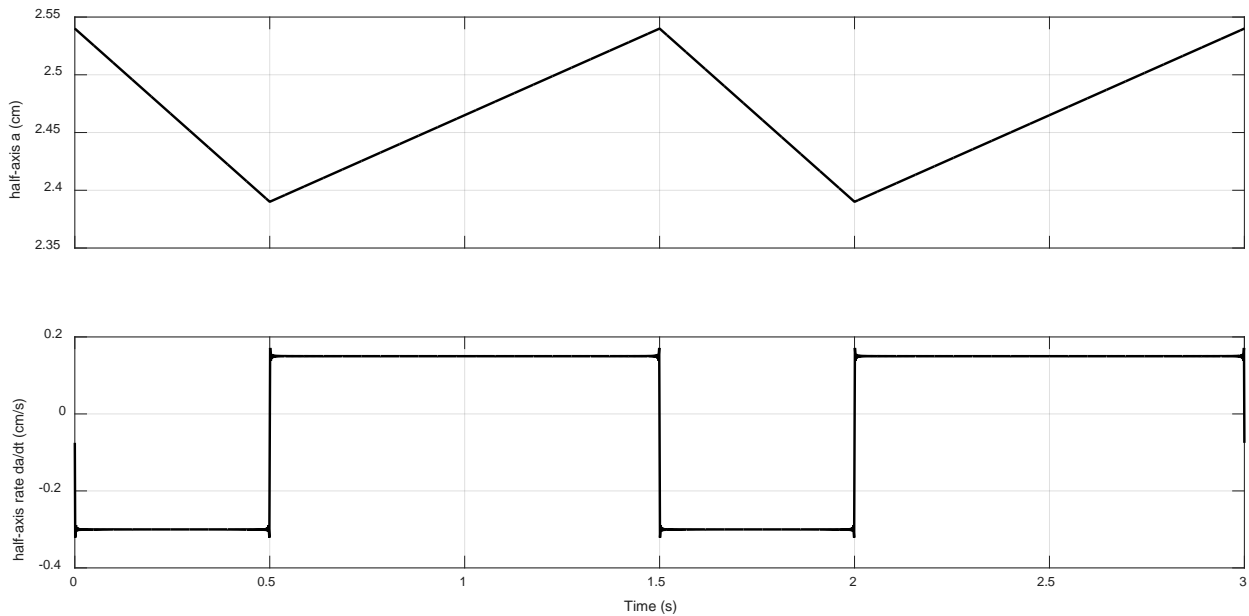
Figure 4.5 Input Half-Axis Dimension for Geometric Model, 1000th Partial Sum Input
Using the ellipsoid model, the input half-axis dimension a takes on the above rate of change and numeric values during deformation.

40

Using this input waveform, a short simulation comparing the two swimming modes is presented in Figure 4.6. The 3rd and 1,000th partial sums are compared to illustrate the effect of a non-ideal input. As evident from the plots, the proposed P1 mode performs better when using the more efficient inlet/outlet directions as compared to the P2 mode. This was expected as the mass-flux into the internal volume is in the same direction as the mass-flux out during the contraction phase.

The effects of the non-ideal input are also expected. A lower partial sum of the Fourier series leads to a larger transition region between contraction and relaxation phases, so the robot slows down and begins to refill the internal volume sooner than in the idealized case. This effect is also seen in the plot, where at approximately $t = 0.4$ the robot begins to decelerate when the non-ideal partial sum is used. This contrasts with the sharp acceleration change seen in the plot for the idealized input. Ultimately, both input waveforms yield higher swimming performance than the biological swimming mode, and the proposed robot design looks to be a promising concept.
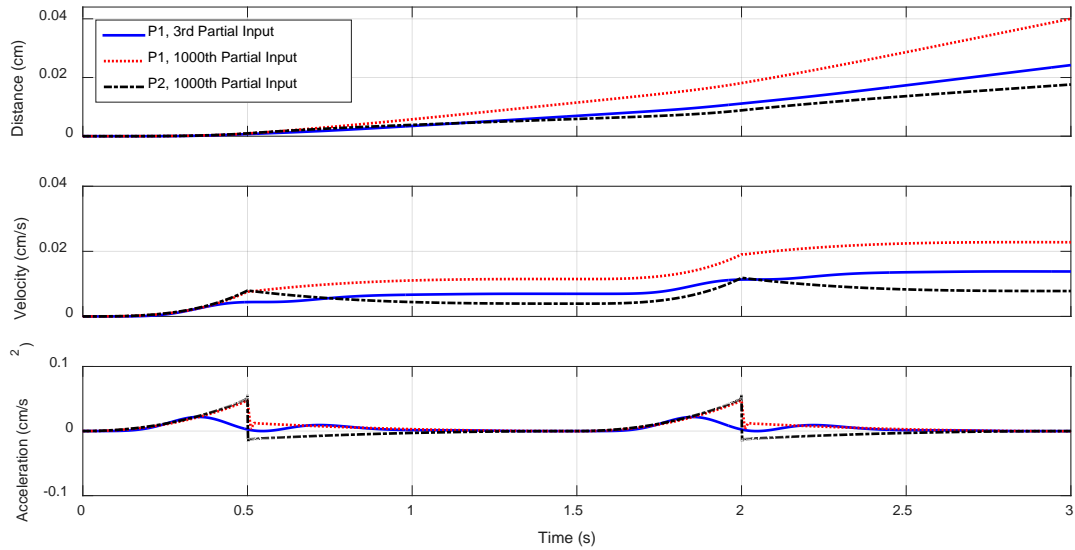
Figure 4.6 Simulation of Geometric Model with Various Inputs and Swimming Modes
From the plots shown, the P1 swimming mode far out performs the P2 mode, and the higher partial sum that correlates to a more ideal input results in an increased performance.

A plot of the thrust profile is given in Figure 4.7 where the effect of the forward-facing inlet is more easily seen. During the contraction phases, both thrust profiles are identical, but when the robot body begins to relax and take water into the internal volume, the P1 mode generates a positive thrust while the P2 mode is negative. An important consequence of this is that the relation between contraction and relaxation time is no longer as important in generating a net positive thrust.
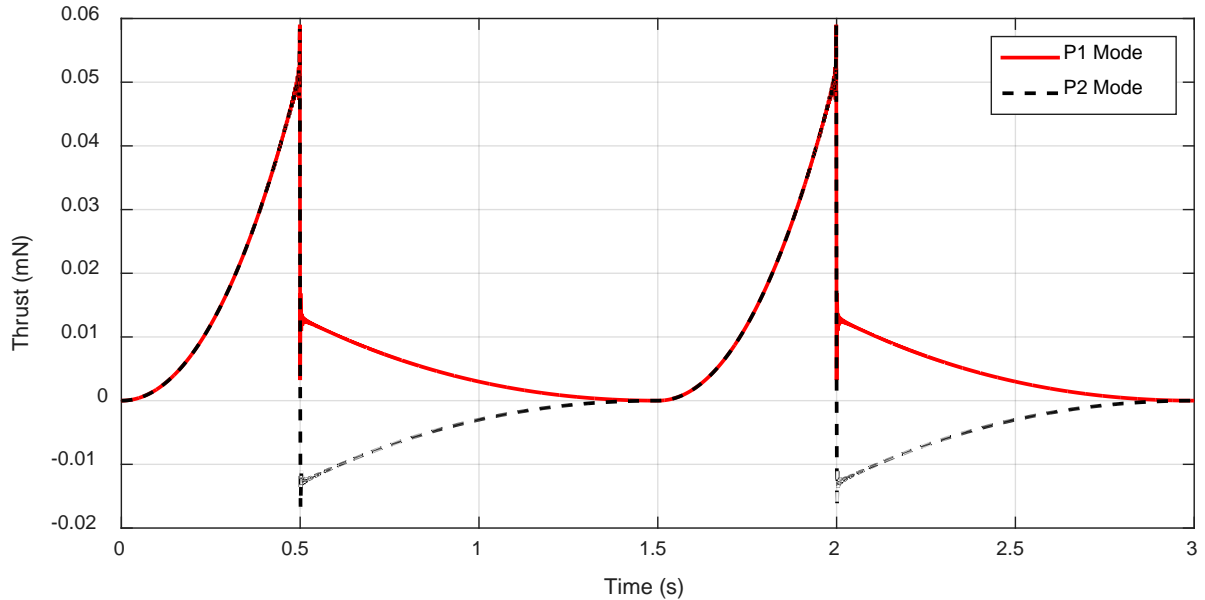
Figure 4.7 Thrust Profile for Geometric Model in Both Swimming Modes
The P1 swimming mode shows a positive thrust profile throughout both the contraction and relaxation phases of the swimming cycle, as opposed to the positive and negative profile of the P2 swimming mode.

4.3. Physics-Based Modeling

To advance from the simplified geometric based approach taken in the previous model, a more physics-based route is explored. Here, the deformation of the robot body will be governed through an implementation of beam theory to describe the shell wall displacement in response to mechanical loading from an EAP actuator. The beam theory is used to simplify the computation of mechanical deformation by reducing the problem from the continuum model of solid mechanics. As will be demonstrated, the use of beam theory here is modular, in the sense that more robust and higher order models can be easily implemented in its place. Again, the necessary model parameters for the dynamic EoM are derived and related back to the beam theory deformation used as the method of input. Then, focusing on IPMC actuators, the equivalent circuit model discussed before is implemented to inform the beam model on the electromechanical response of an IPMC.

43

4.3.1. Beam Theory Approach

Relating back to Figure 4.3, the new modeling approach breaks away from the constraint of the robot body being fully defined by the equation of an ellipsoid. Instead, as illustrated in Figure 4.8, the body is broken into active and passive regions, where the active region is physically deformed under the IPMC loading, and the passive region is completely dictated by the boundary conditions imposed on the geometry. Again, the deformation is assumed to be symmetric about the z-axis. A cross-section is illustrated in, where the length measurement of the actuator is more apparent, and the planes of symmetry are highlighted. Throughout the modeling process, only the first quadrant of the cross-section is analyzed and the axis symmetry about the z-axis and mirror symmetry about the xy-plane is enforced.
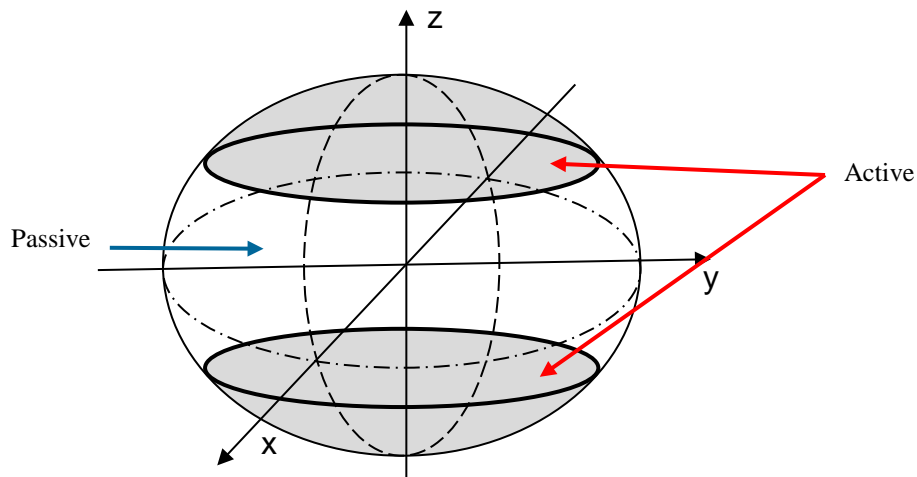
Figure 4.8 Diagram of Physics-Based Description of Robot Body
Active portions of the robot body can be deformed using a wide variety of EAP actuators.
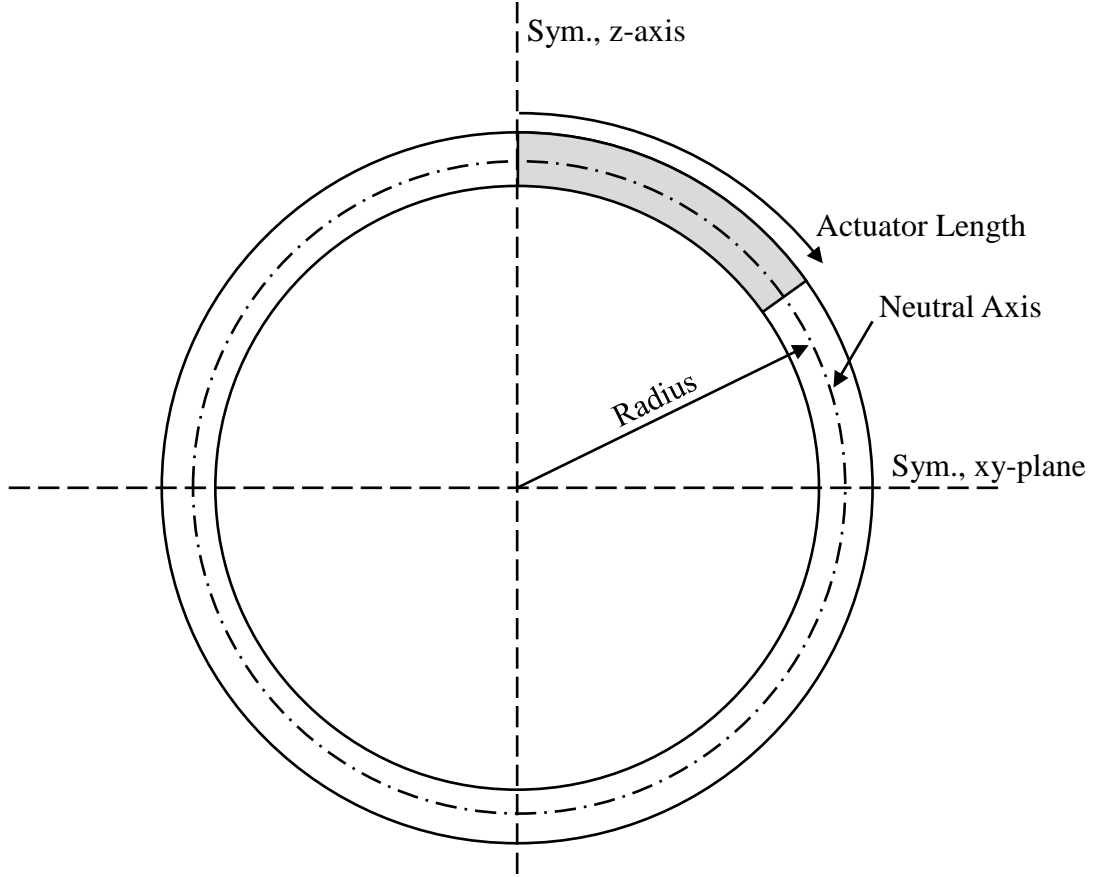
Figure 4.9 Illustrative Cross-Section of Proposed Physics-Based Model
The symmetry z-axis and xy-plane are shown in the illustration, as well as the actuator length within the active portion of the shell wall, and the radius describing the neutral axis of the beam used within the beam theory.

To describe the deformation of the shell wall, a cross-section slice along the y-z plane is taken and the upper portion of the shell is modeled as a curved beam. Using virtual displacement, a functional of the form below is obtained

$$\int_0^L M\delta\kappa + N\delta\epsilon - P_w\delta w - P_v\delta v \, ds = 0 \tag{4.16}$$

where M, N, P, w v, and s are the internal bending moment, internal axial load, external loading broken into transverse (P_w) and axial (P_v) directions, transverse and axial displacements, and the

local axial coordinate along the length of the beam, respectively. The infinitesimal strain of the beam is defined in terms of the curvature and axial strain, κ and ϵ, given by

$$\epsilon = v' - \frac{w}{\rho} \tag{4.17}$$

$$\kappa = w'' + \left(\frac{v}{\rho}\right)' \tag{4.18}$$

where ρ is the undeformed radius of curvature of the beam, assumed to be constant for simplicity. The first terms in both strain expressions are the familiar axial and curvature strain found in the Euler-Bernoulli beam theory for straight beams [95]. Not as familiar are the second terms, which are couplings of the transverse and axial deformation to the axial and curvature strains which is found only in curved beams. It can be easily verified that as the radius of curvature tends towards infinity, these terms tend to zero and thus the straight beam theory is recovered.

Now, the assumptions of an inextensible beam, transverse external load, and linear elasticity are applied which yields the new functional for the beam

$$\int_0^L EI\left(w'' + \frac{w}{\rho^2}\right)\delta\left(w'' + \frac{w}{\rho^2}\right) - P_w\delta w\, ds = 0 \tag{4.19}$$

with Young's modulus E and cross-sectional moment of inertia I. Using the standard virtual displacement procedure, the functional shown can be used to construct the governing ODE for the beam's deformation seen below. Similarly, it can be easily shown that as the radius of curvature tends towards infinity, the Euler-Bernoulli equation for straight beams is recovered.

$$w^{iv} + \frac{w''}{\rho^2} + \frac{w}{\rho^4} = \frac{P_w}{EI} \tag{4.20}$$

with a general solution obtained by solving the homogenous and particular solutions of

Equation (4.20)

$$w(s) = A\cos\left(\frac{s}{\rho}\right) + B\sin\left(\frac{s}{\rho}\right) + C\cos\left(\frac{s}{\rho}\right)s + D\sin\left(\frac{s}{\rho}\right)s + \frac{P_w \rho^4}{EI} \tag{4.21}$$

In anticipation of finding an easily modified model with as close to a closed form

solution as possible, a volume integral of the form below must be calculated for use in the

dynamic EoM.

$$V_i = \iiint r^2 \sin\theta \, dr d\theta d\phi \tag{4.22}$$

where $r = (\rho + w)$ describes the outer shell walls deformation, and hence internal volume. This

form depends nonlinearly on the transverse deflection, w, of the beam model. Due to the form

seen in Equation (4.21), which is entirely dependent on boundary conditions, an alternative

approach is taken to ease the work necessary to compute the volume integral.

Due to its ease in changing boundary conditions without a great deal of additional work,

the Galerkin method is used to form a trial function for the functional in Equation (4.19) to

approximate the transverse deflection. More precisely, the Galerkin method is used to construct

approximations to the deflection in terms of monomials of the local axial coordinate, seen below.

This facilitates easier calculation of the parameters used in the EoM, as will be demonstrated in

the next section. The approximation is constructed as

$$\widetilde{w} = \sum_{n=0}^{N_w} s^n \widehat{w}_n = \boldsymbol{N_s} \widehat{\boldsymbol{w}} \tag{4.23}$$

where $\widetilde{w}$ is the trial function, N_w is the number of monomial shape functions used, $\boldsymbol{N_s}$ is a vector

of the shape functions, and $\widehat{\boldsymbol{w}}$ is a vector of the Galerkin coefficients $\widehat{w}_n$. Boundary conditions

are enforced by influencing the resulting stiffness matrix directly using the Galerkin form of the displacement, slope, bending moment, and shear force of the beam, given below.

$$\widetilde{w} = N_s \widehat{w} \tag{4.24}$$

$$\widetilde{w}' = N_s' \widehat{w} \tag{4.25}$$

$$\widetilde{M}_{moment} = (N_s'' + \frac{N_s}{\rho^2})\widehat{w} \tag{4.26}$$

$$\widetilde{V}_{shear} = (N_s''' + \frac{N_s'}{\rho^2})\widehat{w} \tag{4.27}$$

where the moment and shear relations have been derived from the Euler-Bernoulli expressions and introductory beam theory. Substitution of the Galerkin trial function into the functional in Equation (4.19) results in:

$$\delta \widehat{w}^T \int_0^L N_s^T \left[EI \left(N_s^{(iv)} + \frac{N_s''}{\rho^2} + \frac{N_s}{\rho^4} \right) \widehat{w} - P_w \right] ds \tag{4.28}$$

which can be written as:

$$K\widehat{w} = \overline{P} \tag{4.29}$$

with stiffness matrix and load vector defined as:

$$K = \int_0^L N_s^T \left[EI \left(N_s^{(iv)} + \frac{N_s''}{\rho^2} + \frac{N_s}{\rho^4} \right) \right] ds \tag{4.30}$$

$$\overline{P} = N_s^T P_w \tag{4.31}$$

which is a system of linear equations to solve for the unknown Galerkin coefficients $\widehat{w}_n$. The integration of the stiffness matrix is achieved using Gauss-Legendre quadrature. Because the shape functions are simple monomials, the quadrature scheme is easily implemented after a few modifications.

The local axial coordinate is first normalized with respect to the length using the following coordinate transformation.

$$\zeta = \frac{s}{L} \tag{4.32}$$

Traditional Gauss-Legendre quadrature is conducted on the domain [-1,1], so the quadrature weights and Gauss points are transformed as well with:

$$G_p' = 1 - \left| \frac{1 - G_p}{2} \right| \tag{4.33}$$

$$G_w' = \frac{G_w}{2} \tag{4.34}$$

Where Equation (4.33) transforms the domain [-1,1] of the traditional Gauss points to the domain of [0,1] of the normalized local axial coordinate, and Equation (4.34) transforms the Gauss weights accordingly to obtain the correct integration. The integrand of the stiffness matrix can then be written as

$$\boldsymbol{N}_\zeta^T \left[EI \left(\boldsymbol{N}_\zeta^{(iv)} + \frac{\boldsymbol{N}_\zeta''}{\rho^2} + \frac{\boldsymbol{N}_\zeta}{\rho^4} \right) \right] = \widetilde{\boldsymbol{N}}_\zeta(\zeta) \tag{4.35}$$

with $\boldsymbol{N}_\zeta$ being the new shape functions in terms of the normalized length coordinate. Now the stiffness matrix, calculated using Gauss-Legendre quadrature, becomes

$$\boldsymbol{K} = L \int_0^1 \boldsymbol{N}_\zeta^T \left[EI \left(\boldsymbol{N}_\zeta^{(iv)} + \frac{\boldsymbol{N}_\zeta''}{\rho^2} + \frac{\boldsymbol{N}_\zeta}{\rho^4} \right) \right] d\zeta = L \int_0^1 \widetilde{N}_\zeta(\zeta) d\zeta = L \sum_{i=1}^{O_G} G_{w,i}' \widetilde{N}_\zeta(G_{p,i}') \qquad (4.36)$$

where O_G is the order of the quadrature scheme. Now, with the transverse deformation able to be computed, the condition of inextensibility can be used to determine the local axial deformation induced in the beam.

$$\epsilon = v' - \frac{w}{\rho} = 0 \qquad (4.37)$$

$$\tilde{v} = \frac{1}{\rho} \int_0^L \widetilde{w} \, dx = \frac{1}{\rho} \int_0^L \sum_{n=0}^{N_w} s^n \widehat{w}_n \, ds = \frac{1}{\rho} \sum_{n=0}^{N_w} \frac{L^{n+1}}{n+1} \widehat{w}_n \qquad (4.38)$$

The last step in this process illustrates how the use of monomial shape functions facilitates easier integration in the process of deriving these necessary equations. With the transverse and axial deformations computed in a frame local to the curved beam, they can be transformed into standard Cartesian coordinates via:

$$\begin{Bmatrix} u_x \\ u_y \end{Bmatrix} = \begin{bmatrix} cos(\theta_s) & sin(\theta_s) \\ -sin(\theta_s) & cos(\theta_s) \end{bmatrix} \begin{Bmatrix} \tilde{v} \\ \widetilde{w} \end{Bmatrix} \qquad (4.39)$$

where $\theta_s = {}^s\!/_\rho$ is the angle defining the position along the beam in polar coordinates with $\theta_s = 0$ starting at the beginning of the beam moving in a clockwise positive direction.

An important question must be raised regarding the accuracy of the approach described. A simple beam model on the scale expected for the proposed design was created in COMSOL in which the continuum mechanics equations for mechanical deformation are solved under a linear elastic assumption and serves as a benchmark for the beam model. A plot comparing the deformation is given in Figure 4.10, while information regarding the beam geometry, material, and loading is given in Table 4.2. From the figure it's clear that the proposed implementation of

the curved beam theory is acceptable and is in very good agreement with the robust finite

element solution of the continuum equations.
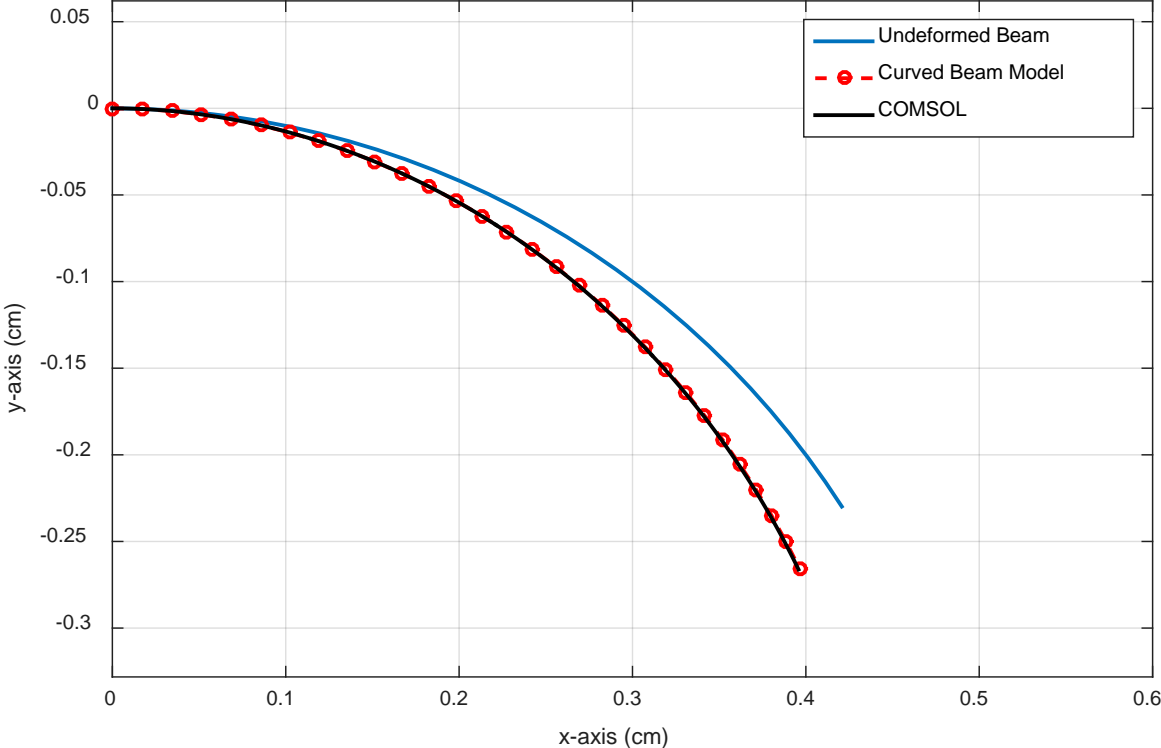
Figure 4.10 Comparison of Beam Theory to FEM Implementation
The proposed modeling approach where a Galerkin approximation is used to model a curved
beam is shown here to be valid when compared to the COMSOL FEM solution.

Table 4.2 Beam Geometry and Loading for COMSOL Comparison

Parameter	Value
Length (cm)	0.5
Width (cm)	0.25
Thickness (cm)	0.25
Modulus (cm)	50
Radius of Curvature (cm)	0.5
Load (N/m)	0.1

One more point of concern is whether the use of a curved beam model is necessary in the given circumstance. In the limit as the radius of curvature of a beam approaches infinity, the solution should approach that of the straight beam. Therefore, it is proposed that an accurate measure of the effect of curvature would be to examine the error incurred in a beam's deflection as a function of the radius of curvature to length ratio.

Figure 4.11 demonstrates such an analysis, where the curvature aspect ratio of the beam used in this model is highlighted and shows that a maximum percent error of approximately 3.5% is incurred when using a straight beam assumption. While this error is not necessarily outside the range of a reasonable approximation, the ease of the Galerkin approximation makes the decision to stay with a curved beam model obvious.
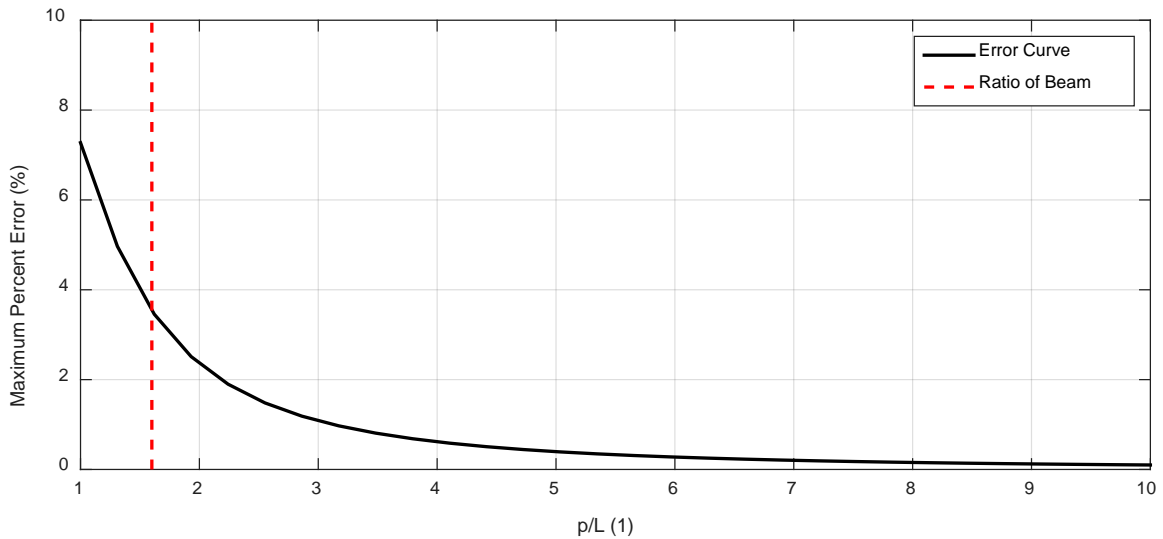
Figure 4.11 Error of Straight Beam Assumption
The abscissa measures the curvature aspect ratio of a curved beam, while the ordinate is a measure of the maximum error obtained in assuming an infinite radius of curvature, i.e. a straight beam.

4.3.2. Derivation of Model Parameters

To derive an expression for the internal volume in this new model, Equation (4.22) is integrated first with respect to the azimuthal angle, ϕ, and the radial distance to obtain:

$$V_i = \frac{4\pi}{3} \int_0^{\frac{\pi}{2}} r^3 \sin(\theta_s)\, d\theta_s \tag{4.40}$$

where the symmetry of the deformation has been leveraged. The integration bounds are left as variable because the integrand, which is dependent on the Galerkin trial function, changes as the polar angle transitions from the active portion to the passive portion of the body. Substituting the trial function into the expression for radial position and factoring out the dependence on the loading and bending stiffness from the Galerkin coefficients yields

$$r = (\rho + \widetilde{w}) = \left(\rho + \frac{P_w}{EI} \sum_{n=0}^{N_w} \theta_s^n \widetilde{\widehat{w}}_n \right) \tag{4.41}$$

where a change of variable has been made from the local axial coordinate into the polar angle, and the Galerkin coefficients $\widehat{w}_n$ have absorbed the dependence on ρ from this change of variable and become $\widetilde{\widehat{w}}_n$. The radial position is seen to have two components, the nominal radius of curvature with an addition of the transverse deflection along the beams length. Substitution of this into the volume integral results in the expression below.

$$
\begin{aligned}
V_i = \frac{4\pi}{3} \int_0^{\frac{\pi}{2}} \Bigg[&\rho^3 + 3\rho^2 \frac{P_w}{EI} \sum_{n=0}^{N_w} \theta_s^n \widetilde{\widehat{w}}_n + 3\rho \left(\frac{P_w}{EI} \sum_{n=0}^{N_w} \theta_s^n \widetilde{\widehat{w}}_n \right)^2 \\
&+ \left(\frac{P_w}{EI} \sum_{n=0}^{N_w} \theta_s^n \widetilde{\widehat{w}}_n \right)^3 \Bigg] \sin(\theta_s)\, d\theta_s
\end{aligned}
\tag{4.42}
$$

In what is to follow, some notation is introduced to simplify the expressions and write the

parameters for the EoM in terms of the mechanical loading. First, the summation terms risen to a

power are condensed into a single expression.

$$\left(\sum_{n=0}^{N_w} \theta_s^n \widetilde{w}_n \right)^p = W_p(\theta_s) \tag{4.43}$$

which allows Equation (4.42) to be rewritten as:

$$V_i = \frac{4\pi}{3} \int_0^{\frac{\pi}{2}} \left(\rho^3 + 3\rho^2 \frac{P_w}{EI} W_1(\theta_s) + 3\rho \left(\frac{P_w}{EI} \right)^2 W_2(\theta_s) + \left(\frac{P_w}{EI} \right)^3 W_3(\theta_s) \right) sin(\theta_s) \, d\theta_s \tag{4.44}$$

Integrating this expression term by term is a cumbersome task, but can be made

significantly easier by noticing that if expanded, the integral is a series of integrals of the form

$$\int_\alpha^\beta a_n \theta^n \, sin \, \theta \, d\theta \tag{4.45}$$

and using integration by parts on this integral gives a series representation of the indefinite

integral, denoted by $I_n(\theta)$

$$I_n(\theta) = cos(\theta) \sum_{m=0}^{\left\lfloor \frac{n}{2} \right\rfloor} \frac{(-1)^{m+1} n!}{(n-2m)!} \theta^{n-2m} + sin(\theta) \sum_{k=0}^{\left\lfloor \frac{n-1}{2} \right\rfloor} \frac{(-1)^k n!}{(n-2k-1)!} \theta^{n-2k-1} \tag{4.46}$$

where $\lfloor \, \rfloor$ is the floor operation, which gives the lowest integer value of its argument through

truncation of the decimal. This allows the definite integrals of the form Equation (4.45) to be

written as

$$^\beta_\alpha \bar{I}_n = I_n(\beta) - I_n(\alpha) \tag{4.47}$$

The integration of the internal volume can now be written in a compact form. From the form of Equation (4.44), it is clear that the integral can be resolved into a polynomial in the mechanical loading, with coefficients that are combinations of ${}_{\alpha}^{\beta}\bar{I}_n$ and $\widetilde{w}_n$. The expansion and collection of these terms can be easily written in compact form using summations, the results of which are given in Appendix B, where the integration bounds and are properly taken care of for the active and passive portions of the shell. Finally, the internal volume is resolved into the cubic polynomial shown in Equation (4.48). The simple polynomial form is a result of the Galerkin approximation used. The time dependence of the volume has now been highlighted and stems solely from the time variations in the loading. The beam theory used has assumed static deflection, and thus the entire model is quasi-static, neglecting inertial effects in the mechanical deformation.

$$V_i(t) = \frac{4\pi}{3}\left[A_0 + A_1\left(\frac{P_w(t)}{EI}\right) + A_2\left(\frac{P_w(t)}{EI}\right)^2 + A_3\left(\frac{P_w(t)}{EI}\right)^3\right] \tag{4.48}$$

The cross-sectional area with respect to the flow direction can be derived with a similar approach as that taken for the volume. Specifically, the area integral necessary is:

$$S = \iint r\, dr d\theta_s \tag{4.49}$$

With the radial distance defined in Equation (4.41), the integral becomes:

$$S_A = 4\int_0^{\pi/2} \rho^2 + 2\rho\frac{P_w}{EI}\sum_{n=0}^{N_w}\theta_s^n\widetilde{w}_n + \left(\frac{P_w}{EI}\sum_{n=0}^{N_w}\theta_s^n\widetilde{w}_n\right)^2 d\theta_s \tag{4.50}$$

55

The integral is in terms of only monomials of the polar angle thus its integration is relatively straight forward and can be evaluated to the expression below, with the coefficients B_0, B_1, and B_2 provided in Appendix B.

$$S_A(t) = B_0 + B_1 \left(\frac{P_w(t)}{EI} \right) + B_2 \left(\frac{P_w(t)}{EI} \right)^2 \tag{4.51}$$

For the added mass and drag coefficient, additional assumptions were made that allow the same relations of the geometric model to be used. The added mass was initially calculated based on an ellipsoid of largest volume that fit the material points along the x, y, and z-axis of the robot body. After some numerical experimentation though, it was found that the added mass coefficient maintained very small oscillations around a value of 0.5, the value for a sphere, and due to the first approximation nature of this model the coefficient has been fixed to this value. Since the deformation to the body is relatively small, the assumption of a spherical geometry is a reasonable approximation. This also influences the approximation for the drag coefficient, where the same sphere drag equation used previously has been implemented in this model.

4.3.3. Addition of IPMC Electromechanical Effects

To couple the electromechanical transduction of an IPMC to the beam theory model, the mechanical loading of the beam, P_w, is related to the electrochemical behavior of the IPMC through Equation (3.17).

$$P_w = \alpha_{RCW} Q \tag{4.52}$$

Again, where the charge, Q, of the IPMC is found through the Laplace transform of the RCW

circuit transfer function below.

$$Q(t) = \mathcal{L}^{-1}\left\{\frac{1}{s}H(s)\mathcal{L}\{V_{ext}(t)\}\right\} \tag{4.53}$$

The Fourier series in Equation (4.2) is still used as the model input here, where it defines the

input voltage to the IPMC. Using Equation (4.53), the charge response of the IPMC to the

Fourier series input is given by

$$Q(t) = \frac{At_c + Bt_r}{t_c + t_r} \frac{2c_1 + c_2}{2}\left(1 - exp\left(-\frac{2t}{2c_3 + c_4}\right)\right) +$$

$$\sum_{n=0}^{\infty} \frac{A - B}{n\pi} \frac{2c_1 + c_2}{4 + \left(f_n(2c_3 + c_4)\right)^2}\left[\left(2\sin(f_n t_c) - (2c_3 + c_4)f_n(1 - cos(f_n t_c))\right)cos(f_n t)\right.$$

$$+$$

$$(2(1 - cos(f_n t_c)) + (2c_3 + c_4)f_n \sin(f_n t_c))sin(f_n t) +$$

$$\left.\left((2c_3 + c_4)f_n(1 - cos(f_n t_c)) - 2\sin(f_n t_c)\right)exp\left(-\frac{2t}{2c_3 + c_4}\right)\right] \tag{4.54}$$

with

$$c_1 = C, \quad c_2 = W, \quad c_3 = RC, \quad c_4 = RW, \quad f_n = \frac{2n\pi}{t_c + t_r} \tag{4.55}$$

The charge response to a representative input for the model is given in Figure 4.12. The

capacitive charge and discharge profiles are clearly visible, and even in this short simulation the

beginning of the decay to a steady state response is seen in the peaks of the charge during the

contraction phases.
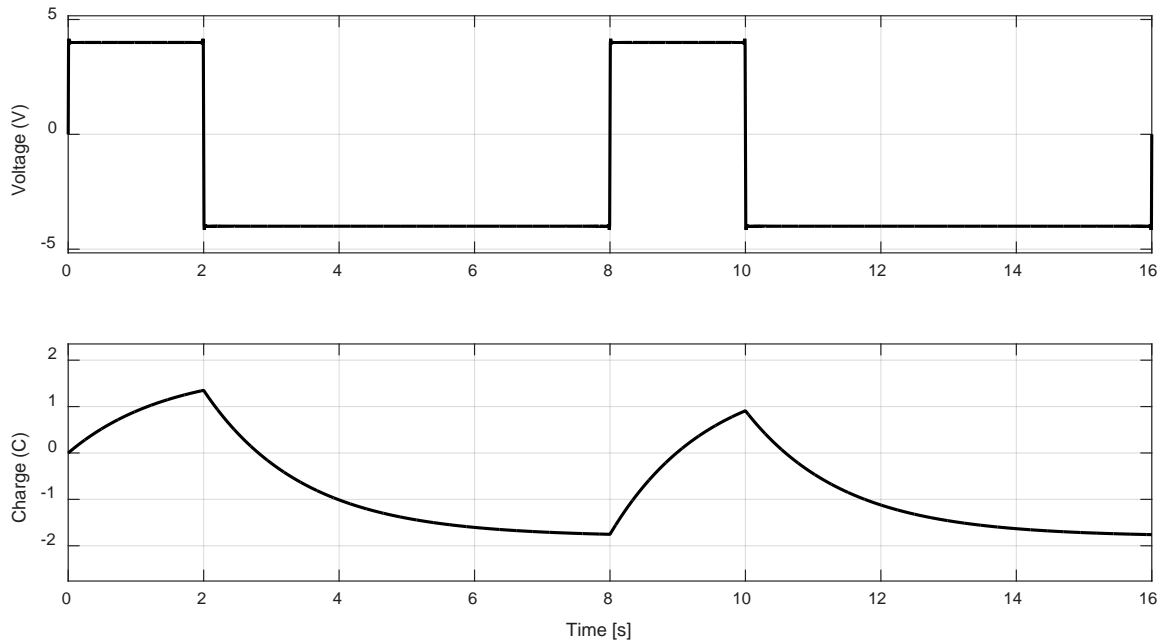
Figure 4.12 RCW Model Charge Response for Fourier Series Input
Noting the input voltage, the charge response shows a non-net-zero charge over each swimming cycle due to the equal voltage amplitudes over different time periods. This can be remedied with an input that follows the constraint of Equation (4.15).

4.3.4. Evaluation and Comparison to Previous Model

A comparison of the swimming behavior of this physics-based model to the two previous models is given in Figure 4.13. For the comparison, the original model in Chapter 2 was used. A jellyfish of comparable size and volume exchange was modeled, the parameters of which are given in Table 4.3. An important note must be made here. The simulation of the biological jellyfish used was matched to a comparable volume exchange of the two proposed models. From [58], the typical volume change for a jellyfish is on the order of 50%, where here a change of only 7.5% is used. While Figure 4.13 demonstrates that the two proposed biomimetic robot models do perform better than the biological counter-part, the biological jellyfish model is not operating at full capacity.

This comes from the limitations on the amount of deformation allowed within the newly proposed physics-based model. By using a linear beam theory, small strain limitations do not

58

allow for the IPMC to be actuated with large deformation. Thus, the model comparisons made

here are for small actuation strokes, for not only the physics-based model but also for the

geometric and biological models, as to keep them within the same performance levels for better

comparison. Taking this into account, the proposed robot design has a clear advantage over the

biological jellyfish, and these are only more prominent at higher levels of deformation and over

longer simulation periods.
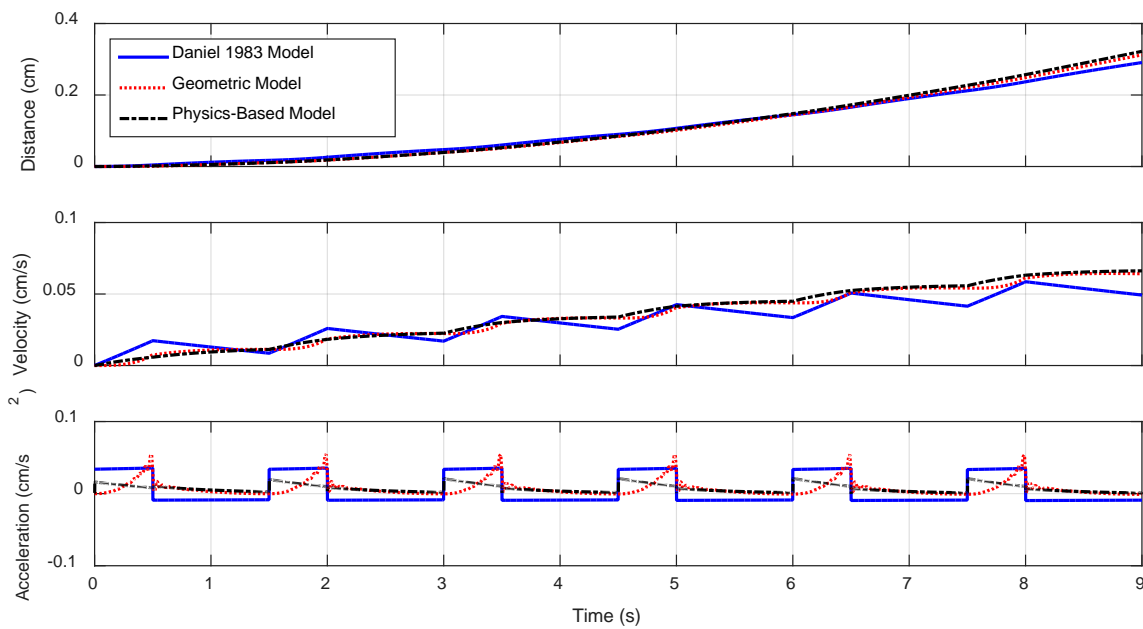
Figure 4.13 Comparison of Physics-Based Model to Geometric and Jellyfish Models
The two robot models are compared to the original model of biological jellyfish, where the final
physics-based model is seen to perform better at the given percent volume change.

Table 4.3 Physics-Based Model Comparison Parameters

Parameter	Value		
	Daniel 1983	**Geometric**	**Physics-Based**
Radius of Body (mm)	~	25.4	25.4
Height of Bell (mm)	25.4	~	~
Half-Axis Rate (mm/s)	~	3	~
Volume Change (%)	7.5	~	~
IPMC Length (mm)	~	~	20.5
IPMC Width (mm)	~	~	9.94
IPMC Thickness (mm)	~	~	0.57
Voltage (V)	~	~	4
Contraction Time (s)	0.5	0.5	0.5
Time Ratio (1)	2	2	2
Outlet Radius (mm)	12.7	1	1

Evaluating the physics-based model on its own, the thrust profile given in Figure 4.14 for both P1 and P2 swimming modes is reminiscent of the geometric model. The biomimetic mode shows a constant positive thrust where the relaxation phase component is seen to be mirror over the zero-line. Furthermore, the longer simulation allows for the transient behavior of the initial IPMC actuation to be more easily seen. The peak thrust during the contraction phase is at the initial contraction, which is followed by a steep decay in thrust. Similarly, the relaxation phase sees a high initial thrust value, followed by a slower decay until the next contraction occurs. This is due to the initial expelling or intake of water and can be directly related to the mass flux through the system, as shown in Figure 4.15.
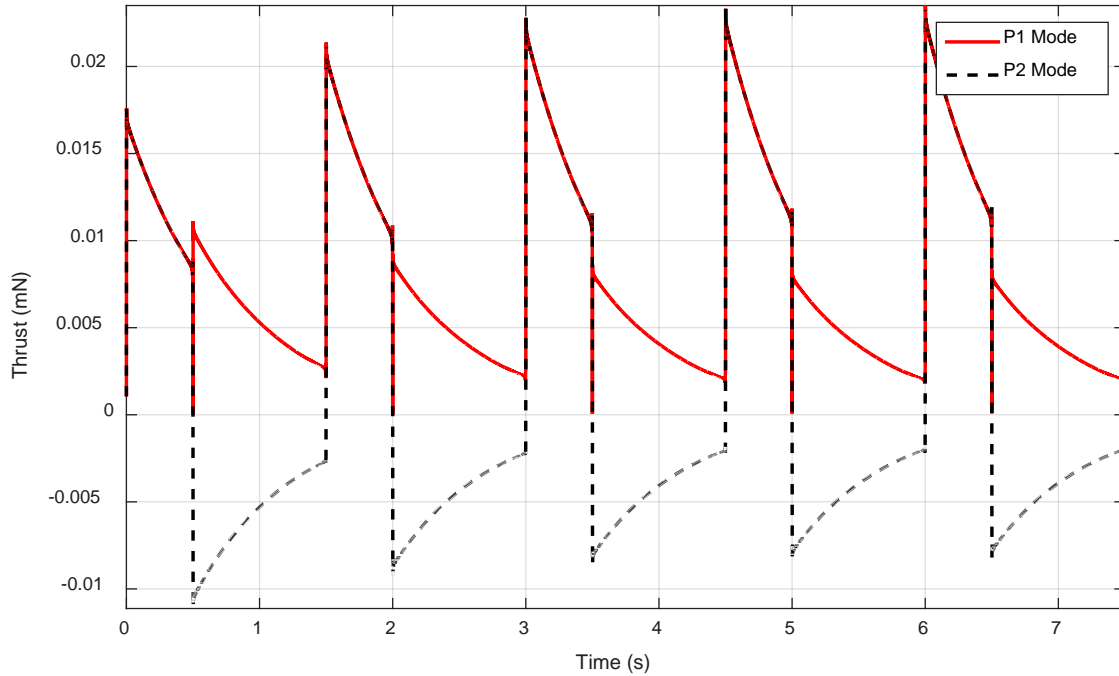
Figure 4.14 Thrust Profile for Physics-Based Model
As seen before for the geometric based model, the physics-based model shows a positive thrust profile throughout the swimming cycle in the P1 swimming mode.
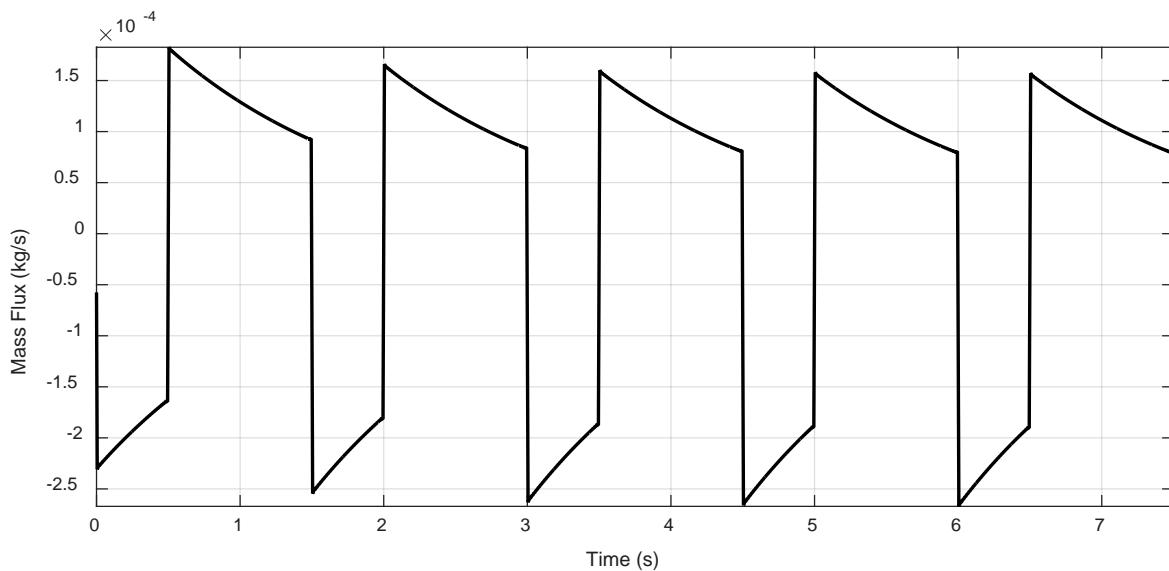
Figure 4.15 Mass Flux for Physics-Based Model
The mass flux throughout the body of the robot is characteristic of the momentum exchanged through the fluid pumped out of the device.

61

Observing the mass flux profile, during the contraction phase there is a negative flux as water leaves the internal volume. If a control volume is drawn at the outlet of the robot, and if the robot were constrained and fixed in place, the fluid motion through the control volume may be plotted. The ejected fluid through the control volume has a velocity given by

$$v_e = \frac{\dot{m}}{\rho_w A_v} \tag{4.56}$$

where $\dot{m}$ is the mass flux through the control volume. It can be easily visualized that during the relaxation phase, the velocity through this control volume is zero, assuming the inlet is forward facing. Thus, the system now behaves as a unidirectional fluid pump. Clearly, the longer the relaxation phase is the more pulsating the flow through the control volume becomes. If the time ratio for the robot is then lowered, the velocity through the control volume becomes more continuous. This is illustrated in Figure 4.16, where velocity profiles for the device in normal operation and the described low time ratio are shown for comparison.

This type of operation transforms the robot into a fluid pump, allowing for a near constant mass flow or a pulsating flow, making it suitable for multiple applications in low volume fluid pumping, akin to the proposed design in [96]. An interesting feature is the unidirectional aspect of this pump, where using one-way valves inherent in the structure of the shell, back flow is restricted. The IPMC driven actuation also makes the system a low voltage component. An alternative input voltage waveform may also allow for a more uniform flow velocity, but this is a question for future optimization and experimentation.
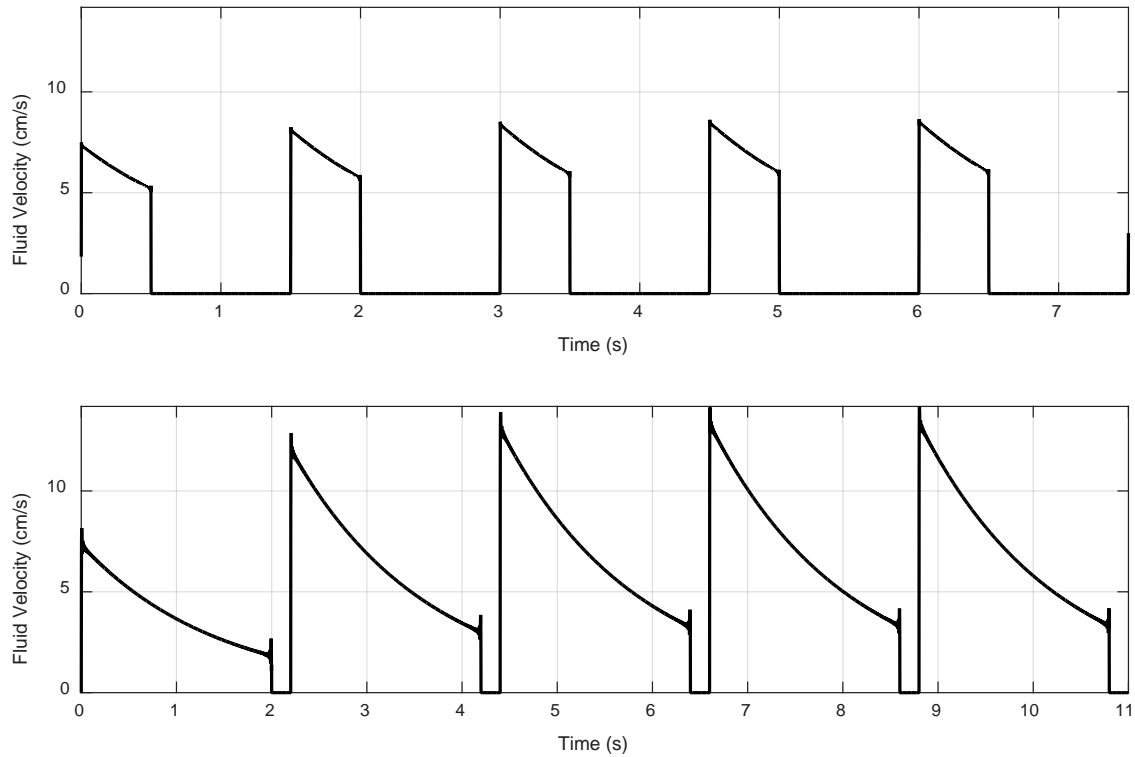
Figure 4.16 Velocity Profiles for Fluid Pump Operation
Fluid velocity profile at outlet of device. The outlet fluid velocity during a swimming operation shows the distinct pulse during contraction phases. By extending the contraction phase over a longer period and shortening the relaxation phase, the outlet velocity becomes more continuous and the device may be used as a fluid pump. (Top) Swimming operation. (Bottom) Fluid pumping operation.

Chapter 5. Design Optimization

With a physics-based model for the swimming behavior of the proposed robot, there is a question of whether the original design can be improved upon. Here, a simple design optimization is conducted to search for model parameters that give largest swimming distance over a given period. To conduct the optimization, a sequential quadratic programming (SQP) routine is implemented in MATLAB on a few, hand selected design parameters. These parameters are investigated from a qualitative view to gain some understanding of how they might interact with each other during the optimization process. From there, an optimization routine is run to search for the optimal parameters, and the newly optimized design is compared to the originally proposed model. Some preliminary work on the scalability of the device is also presented and a discussion on the limitations of the model as it relates to its optimization capabilities is discussed.

5.1. Sequential Quadratic Programming Optimization

5.1.1. Selection of Design Variables

The design variables selected for optimization were chosen manually with some insight into the model and its limitations. Of all the possible variables involved in the physics-based model, the three chosen as design parameters were the IPMC length, contraction time, and time ratio. Other parameters, such as IPMC thickness, IPMC width, valve aperture, input voltage, and many more have significant effects on the performance of the robot, but due to a few model limitations which will be discussed later, these were not viable selections.

As expected, the IPMC length plays an important role, but its exact effects on the performance of the robot were not fully understood. To begin the optimization process, the

model was made into an executable MATLAB function that took an input of the IPMC length
and would output the maximum distance traveled over a 30 second period. This gives a
qualitative understanding of how the parameter affects the swimming behavior. The results of
this numerical experiment are given in Figure 5.1, where there is a noticeable peak in
performance around $L = 26$ (mm). While the increase in performance with increasing length was
expected, the rapid decay in distance traveled when passing the peak value was not. This is
attributed to the degree the shell wall is deformed as the length increases. After the length passes
the observed optimal value, the contraction and relaxation phases switch roles in the sense that
during the "contraction" phase, the internal volume is increased, and the "relaxation" phase sees
a decrease in volume. This effectively changes the operation behavior of the device and when
keeping the contraction time and time ratio constant, this results in decreased performance. The
parameters for the model simulation are given in Table 5.1.
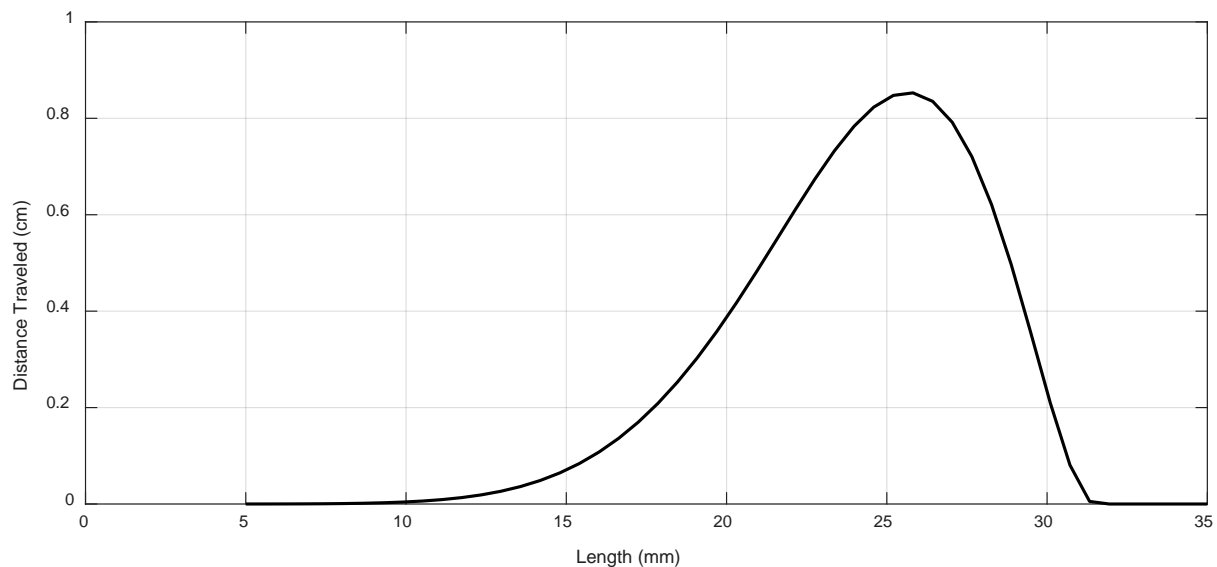
Figure 5.1 Distance vs IPMC Length
A simple plot of distance traveled as a function of IPMC length shows that an optimal value for
the length is located near 26 (mm).

Table 5.1 Simulation Parameters for IPMC Length Optimization

Parameter	Value
Simulation Time (s)	30
Time Step (s)	0.001
Contraction Time (s)	0.5
Time Ratio (1)	2

To gain further insight in the design variables in question, a surface plot of distance traveled was constructed for the pairwise combinations of the three parameters. These surface plots are a kind of brute force optimization aid where one can visually identify the trends in the performance of the model based on the two-parameter combination. Since the approach requires repeated simulations, the accuracy of the model has been sacrificed to a degree to speed up the process, as reflected by the increased time step shown in Table 5.2. Because these surface plots are more qualitative, the loss in accuracy is not an issue, and a more robust optimization will be conducted in the next chapter.

The surface plot for the combination of IPMC length and the contraction time shows an unsurprising trend. The familiar optimal value for the length parameter is evident, and a monotonically decreasing distance in the contraction time is seen. These results are expected, but it at least verifies the behavior seen in Figure 5.1. Turning to the plot of IPMC length and the time ratio, the surface profile is a little more interesting. The profile observed in Figure 5.1 is still prevalent, but the behavior of the surface shows a global maximum near a time ratio value of $\delta_t \cong 2.5$. This means that there may be an optimal design solution in this neighborhood that could be found using a more robust optimization routine. For now, it will be taken only for a qualitative understanding of where a more optimal design may reside. Finally, the results of pairing the contraction time and time ratio give a predictable surface plot. The monotonically

decreasing behavior of the contraction time is evident while the peak value associated with the

time ratio discussed previously is clearly seen. These qualitative results are presented in Table

5.3, where the original unoptimized design parameters are listed alongside of the expected

optimal parameter values.

Table 5.2 Simulation Parameters for Pairwise Optimization

Parameter	Value	Range
Simulation Time (s)	20	~
Time Step (s)	0.005	~
Contraction Time* (s)	0.5	0.2-2
Time Ratio* (1)	2	1-10
Length* (mm)	20.5	5-35

* Indicates the value taken when the variable is not selected as design parameter for optimization plots.
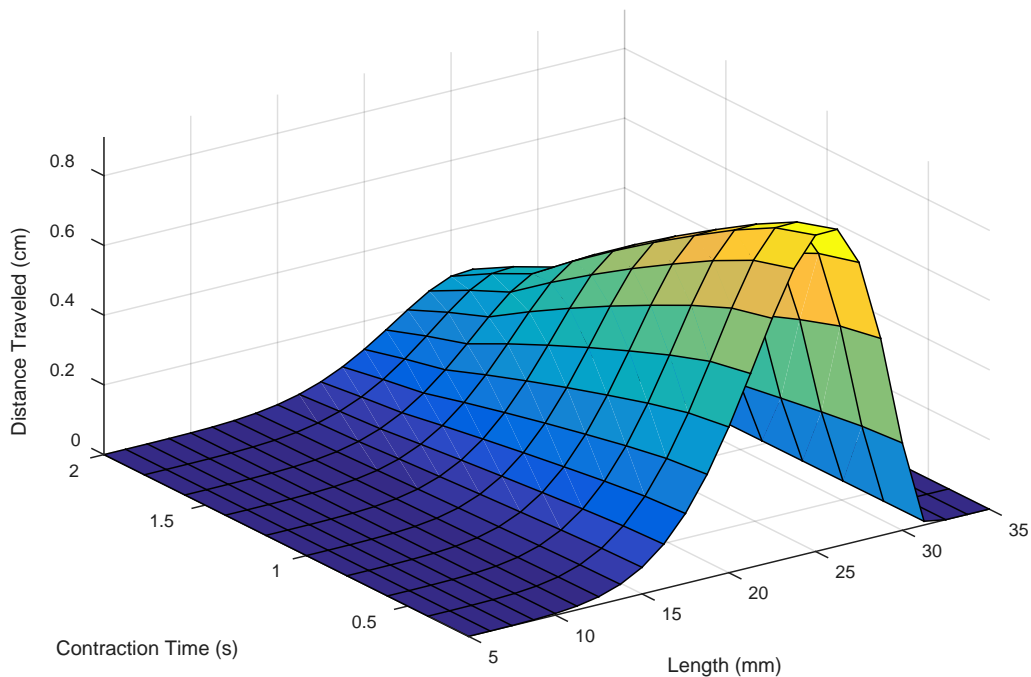
Figure 5.2 Surface Plot of Distance vs Length and Contraction Time
The two-parameter surface plot shows the interaction between the length and contraction time
and their effect on distance traveled.

67
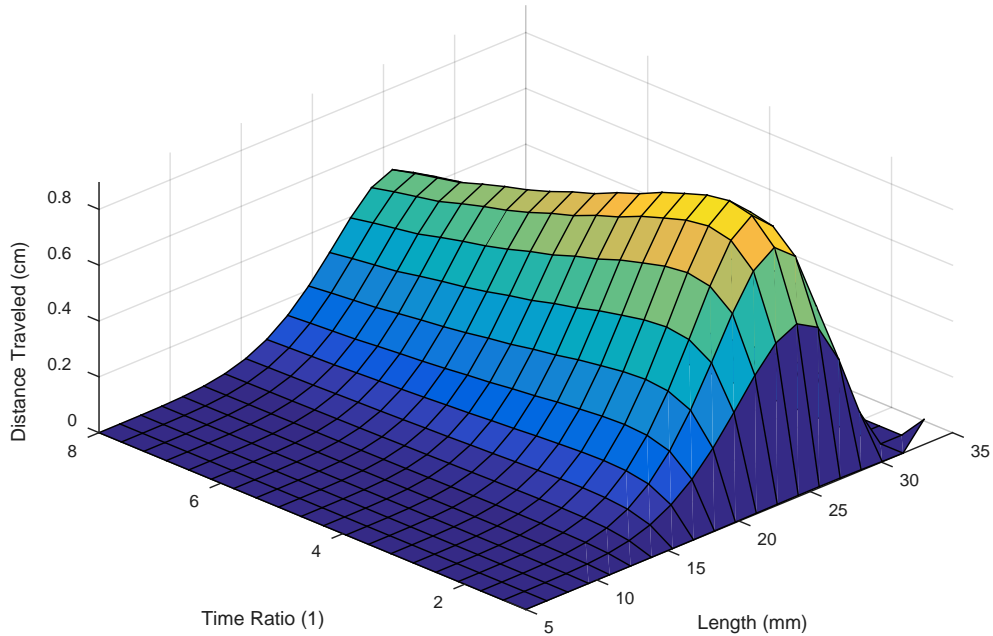
Figure 5.3 Surface Plot of Distance vs Length and Time Ratio
The two-parameter surface plot shows the interaction between the length and time ratio and their effect on distance traveled.
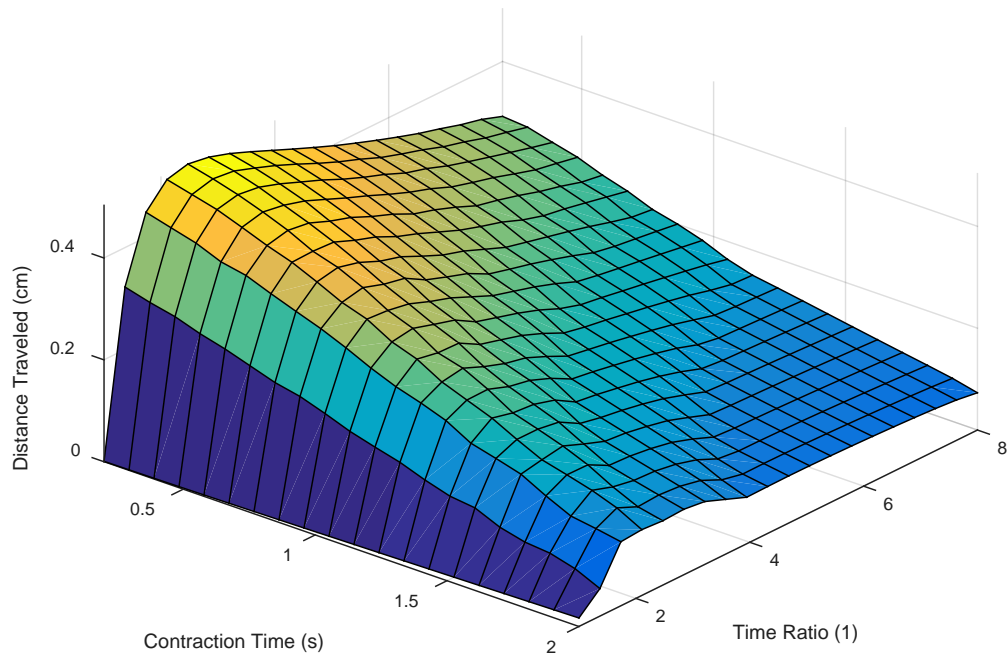
Figure 5.4 Surface Plot of Distance vs Time Ratio and Contraction Time
The two-parameter surface plot shows the interaction between the time ratio and contraction time and their effect on distance traveled.

Table 5.3 Parameter Values for Unoptimized and Expected Optimal Designs

Parameter	Unoptimized Design	Expected Optimal Value
IPMC Length (mm)	20.5	26
Contraction Time (s)	0.5	0.2
Time Ratio (1)	2	2.5

5.1.2. Optimization of Design Variables

There are numerous methods for constrained nonlinear optimization, many of which are excellently described in [97]. To conduct a more thorough optimization of these design parameters, an implementation of the SQP method is performed in MATLAB using the fmincon function. This algorithm is capable of handling constrained nonlinear optimization problems. The constraints used here consist only of bounding limits on the design variables and an inequality constraint on the IPMC length. The boundary limits are given as

$$10 < L_{ipmc} \leq \frac{\pi}{2}\rho - \epsilon_L \tag{5.1}$$

$$1 < \delta_t < 5 \tag{5.2}$$

$$0.05 < t_c < 2 \tag{5.3}$$

where ϵ_L is the minimum amount of passive material that makes up the shell wall after the end of the IPMC. The inequality constraint ensures that the length of the IPMC does not exceed the hemisphere that is being modeled after symmetry planes have been addressed. The remaining boundaries for the design parameters have been chosen based on experience with the model. The lower boundary for the time ratio is chosen such that the relaxation time will be no shorter than the contraction, which is an implied assumption in the development of this model. The upper

boundary on the time ratio as well as the boundaries for the contraction time have been chosen to provide a large solution space for the optimization to search within.

To make sure that the optimal solution obtained through this method is accurate, multiple implementations of the algorithm are conducted, each starting from an initial condition that is randomly perturbed. This ensures that more of the solution space is explored by the algorithm, and by collecting multiple solutions statistical metrics can be collected to verify the accuracy of the obtained values. The initial values and perturbations applied to them are given in Table 5.4, along with the simulation parameters used. The perturbations are applied via

$$X_{i,0} = x_i + \delta_i \, r_{i,1}(-1)^{\lfloor r_{i,2} \rfloor} \tag{5.4}$$

where $X_{i,0}$ is the ith parameter's initial value, x_i is the parameter's nominal value, δ_i is the perturbation of the parameter, $r_{i,1}$ and $r_{i,2}$ are distinct random numbers generated for the parameter, and $\lfloor \rceil$ denotes the rounding operator, which outputs the integer value obtained after rounding its argument up or down depending on the leading digit of the decimal. This approach scales the value of each parameter by a range associated with the perturbation in both positive and negative directions based on two randomly generated numbers, thus ensuring that each successive implementation of the SQP algorithm begins at a different initial point.

The SQP function is implemented with the constraints given in Equations (5.1)-(5.3) with an initial condition obtained from Equation (5.4). Here, the routine was run for 100 trials, with the results of each being retained so that the mean and standard deviation for each of the resulting design parameters could be calculated. Random variables are uniformly distributed over the range [0,1].

Table 5.4 Parameters for SQP Optimization of Design Variables

Parameter	Value	Perturbation
Simulation Time (s)	30	~
Time Step (s)	0.005	~
IPMC Length* (mm)	20.5	5
Time Ratio* (1)	2	1
Contraction Time* (s)	0.5	0.1
Passive Material, ϵ_L (mm)	5	~

* Indicates the nominal value used in (5.4)

After 100 successive SQP routines, the resulting optimal parameters obtained were processed into the probability density functions for the IPMC length, time ratio, and contraction time shown in Figure 5.5, Figure 5.6, and Figure 5.7, respectively. The mean and standard deviation for these results are provided in Table 5.5, where it is clear that the final optimal values are in good agreement with the expected results obtained from the surface plots.

Of interest is how precise the results are for the IPMC length, evident from both the probability density function as well as the small standard deviation. Similarly, the contraction time shows a more compact distribution, indicating that the mean value obtained is more likely to be the ideal value. The time ratio shows a wider distribution, corresponding to its larger standard deviation. This implies that the result obtained is not as significant for the optimal

design. This is also expected from the form of the surface plots shown previously, where the decay in performance was not as significant for changes in the time ratio as compared to the contraction time or length.
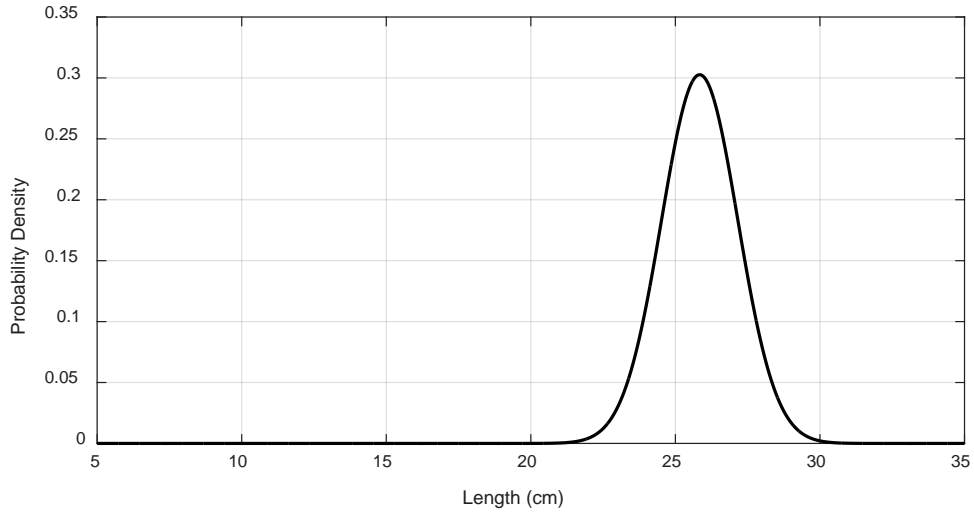
Figure 5.5 Probability Density Function: IPMC Length
The probability density function for the IPMC length helps in visualizing the certainty in the optimal value obtained.
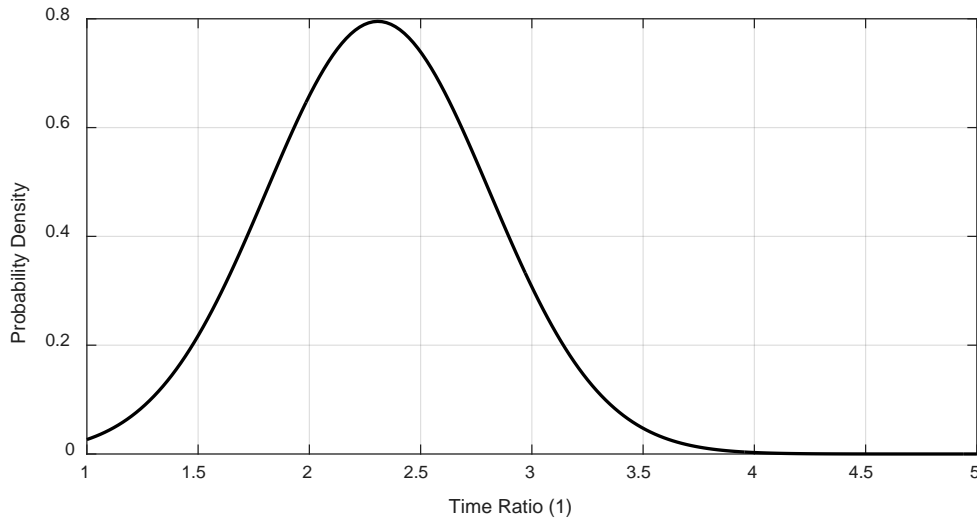
Figure 5.6 Probability Density Function: Time Ratio
The probability density function for the time ratio helps in visualizing the certainty in the optimal value obtained.
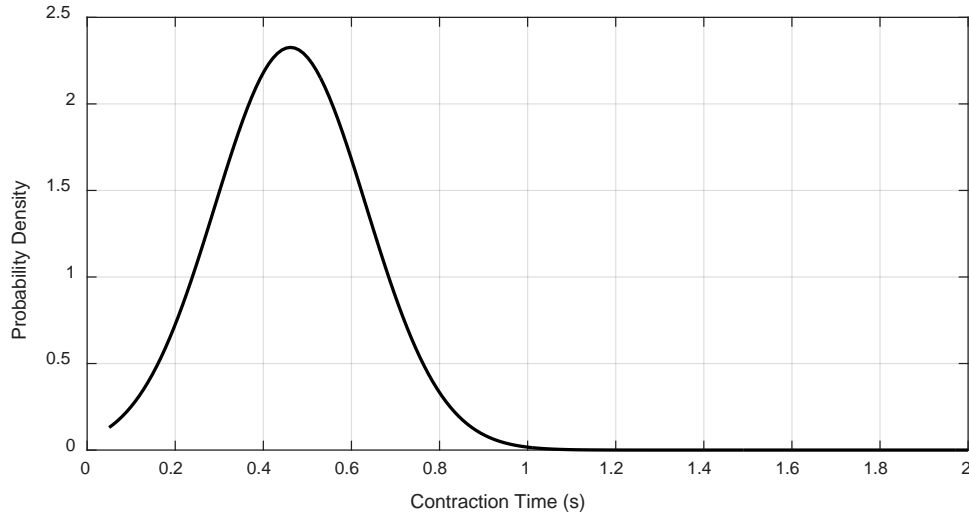
Figure 5.7 Probability Density Function: Contraction Time
The probability density function for the contraction time helps in visualizing the certainty in the optimal value obtained.

Table 5.5 Results of SQP Optimization

Parameter	Mean Value	Standard Deviation
IPMC Length (mm)	25.8	1.32
Time Ratio (1)	2.31	0.502
Contraction Time (s)	0.462	0.171

5.2. Comparison of Unoptimized and Optimized Design

The newly optimized model has been compared to the original unoptimized model for both the P1 and P2 swimming modes. As demonstrated in Figure 5.8, the optimized model far outperforms the unoptimized design. In both swimming modes, the optimal design shows an improvement of approximately a factor of 2 in terms of distance traveled. Again, the advantages of the P1 mode out performances P2, as expected. This strongly indicates that the proposed design may be useful in developing a high performance, highly efficient soft robot for aquatic applications.

73
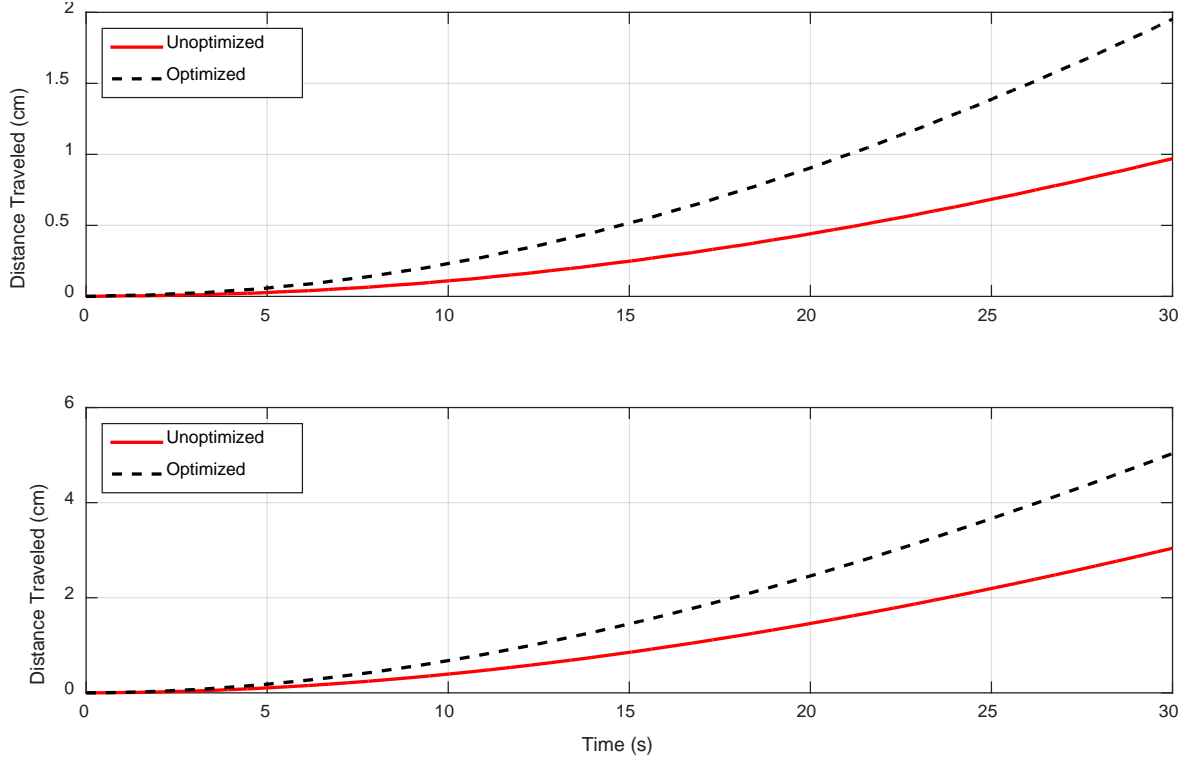
Figure 5.8 Comparison of Unoptimized and Optimized Models: Distance Traveled
Top: Comparison of distance in P2 swimming mode. *Bottom*: Comparison of distance in P1 swimming mode.

A quantitative comparison between the unoptimized and optimized model can be obtained by examining the propulsion efficiency of the two models at steady state. This efficiency is calculated using

$$\eta_{prop} = \frac{2}{1 + \dfrac{v_{fluid}}{v_{robot}}}$$ (5.5)

where v_{fluid} and v_{robot} are the fluid velocity and robot velocity, respectively. As evident from the equation, as the robot velocity matches that of the fluid the efficiency approaches unity, and as the robot velocity drops lower than the fluid, the efficiency approaches zero. These efficiencies are calculated individually, at steady state, over the final contraction and relaxation

cycle, and the result is averaged to obtain the propulsion efficiency for the robot in each

swimming mode. These results are tabulated in Table 5.6, along with the average thrust

generated over the entire swimming cycle. Figure 5.9 shows the resulting velocity plots for the

two models in both the P1 and P2 swimming modes.

Table 5.6 Propulsion Efficiency for Unoptimized and Optimized Models

Model	Swimming Mode	Efficiency (%)	Mean Thrust (μN)
Unoptimized	P1	10.8	8.20
	P2	5.06	2.58
Optimized	P1	11.6	14.2
	P2	6.27	5.38
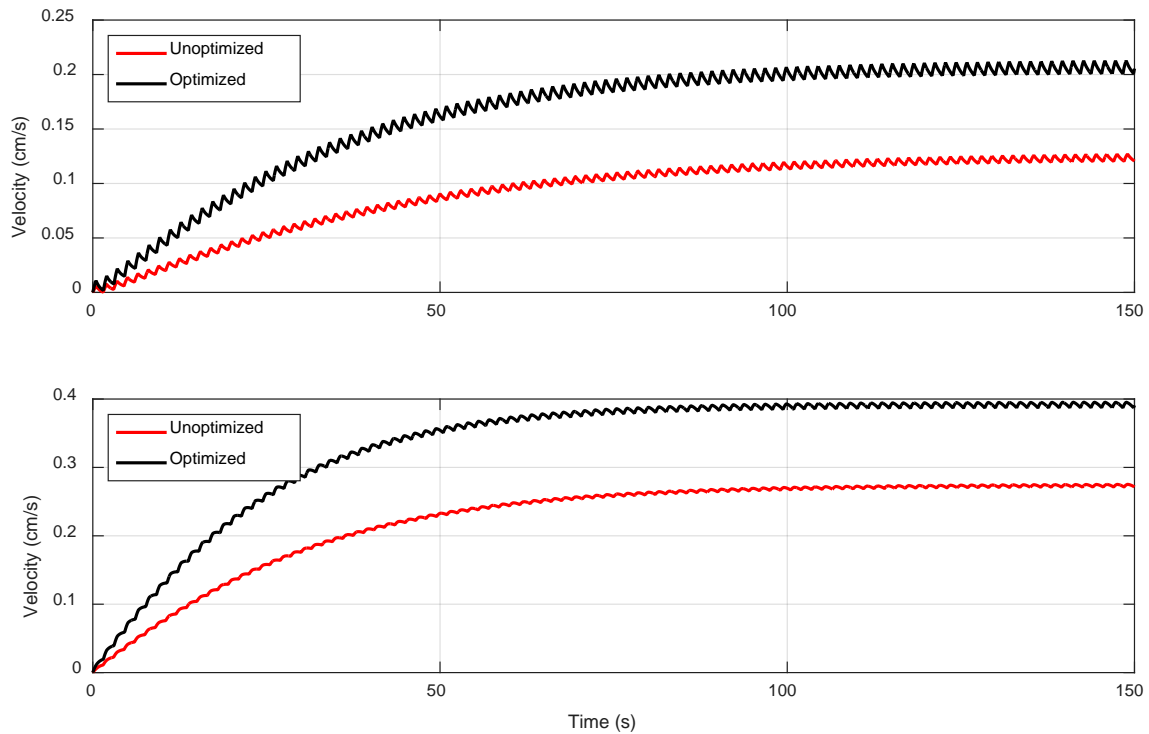
Figure 5.9 Velocity Profiles for Efficiency Calculation
Top: Profile for swimming velocity during P2 mode. Upper profile is the optimized model.
Bottom: Profile for swimming velocity during P1 mode. Upper profile is the optimized model.

The results shown in Figure 5.9 again show a factor increase in velocity of approximately 2 for the optimal design as compared to the unoptimized approach. One further point of interest is that the more efficient swimming behavior of the biomimetic mode leads to the robot reaching its steady state behavior more rapidly. This is evident in the profile of the velocity plots, where the P1 swimming mode is seen to reach its steady state around 50 seconds, whereas the P2 mode takes approximately twice as long.

5.3. Scale Effects on Optimal Parameter Values

To gain insight into how the proposed robot design might scale, a second implementation of the SQP optimization was undertaken. Here, the size of the robot body is scaled, and the optimization routine is used to determine how the chosen design variable's optimal value vary with the size of the robot. There are some limitations regarding the model that limit the physical size of the robot, but these will be elaborated on further in the discussion section of this chapter.

Firstly, the boundaries of the design variables that have the units of length are scaled to the original body radius of 25.4 (mm), thus ensuring that the solution space scales along with the size of the robot. The SQP routine is then used to find an optimal parameter set for five different robot sizes over 25 trials. Data from all 25 optimization routines for each robot size are then used to construct statistics necessary to quantify the results. The final values obtained after this process are tabulated in Table 5.7, where a few interesting trends are seen.

When looking down the column for the IPMC length, there is a clear linear trend that is almost one to one in terms of IPMC length and shell radius. Furthermore, the time ratio and contraction time seem to have no dependence on the size of the robot. As seen from the standard deviation, the results seem to become not as precise as the size of the robot scales up. This may

76

be an implication that as the robot becomes larger, the model no longer has as well defined of an optimal solution as compared to the smaller devices.

Table 5.7 Results of Optimization with Scaled Shell Radius

Radius of Shell (mm)	Optimal Value, Mean / Std. Dev.		
	IPMC Length (mm)	Time Ratio (1)	Contraction Time (s)
10	10.7 / 0.951	2.11 / 0.557	0.418 / 0.125
20	20.2 / 0.104	2.17 / 0.550	0.427 / 0.128
30	30.7 / 2.22	2.30 / 0.544	0.438 / 0.236
40	40.1 / 0.202	2.48 / 0.380	0.551 / 0.363
50	52.6 / 7.31	2.52 / 0.895	0.840 / 1.23

The data given in Table 5.7 is also presented in Figure 5.10, Figure 5.11, and Figure 5.12, where the trends are much easier to visualize. As evident in the data shown in the figures, as the shell radius increases, the precision of the SQP optimization decreases.
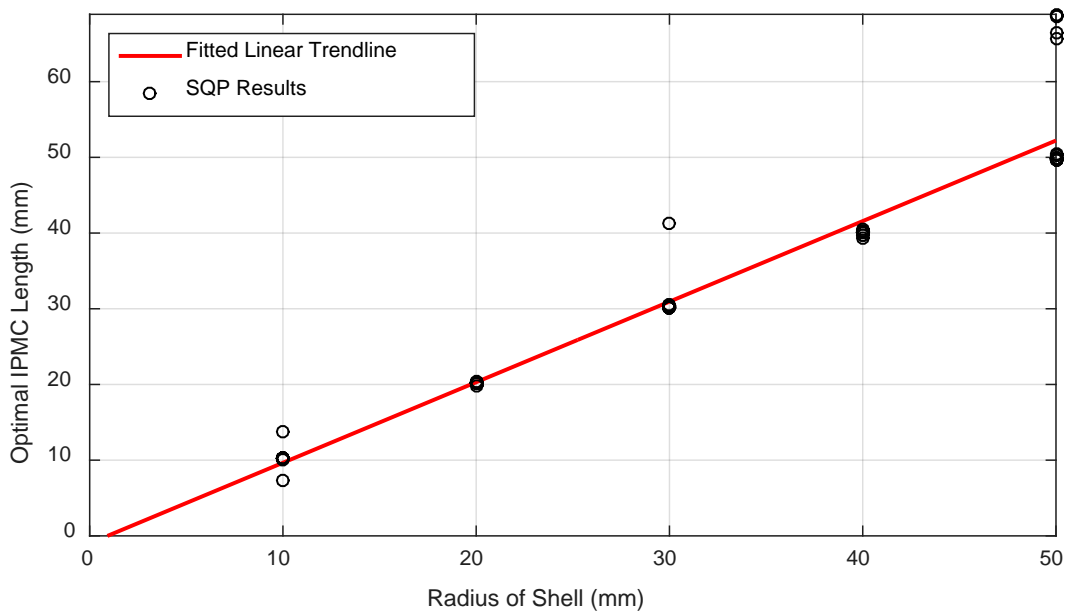
Figure 5.10 Optimized IPMC Length Versus Radius of Shell
The above figure shows the linear trend of the optimized IPMC length as a function of the shell radius. Equation (5.6) gives the regression line shown, where the slope is shown to be near unity.
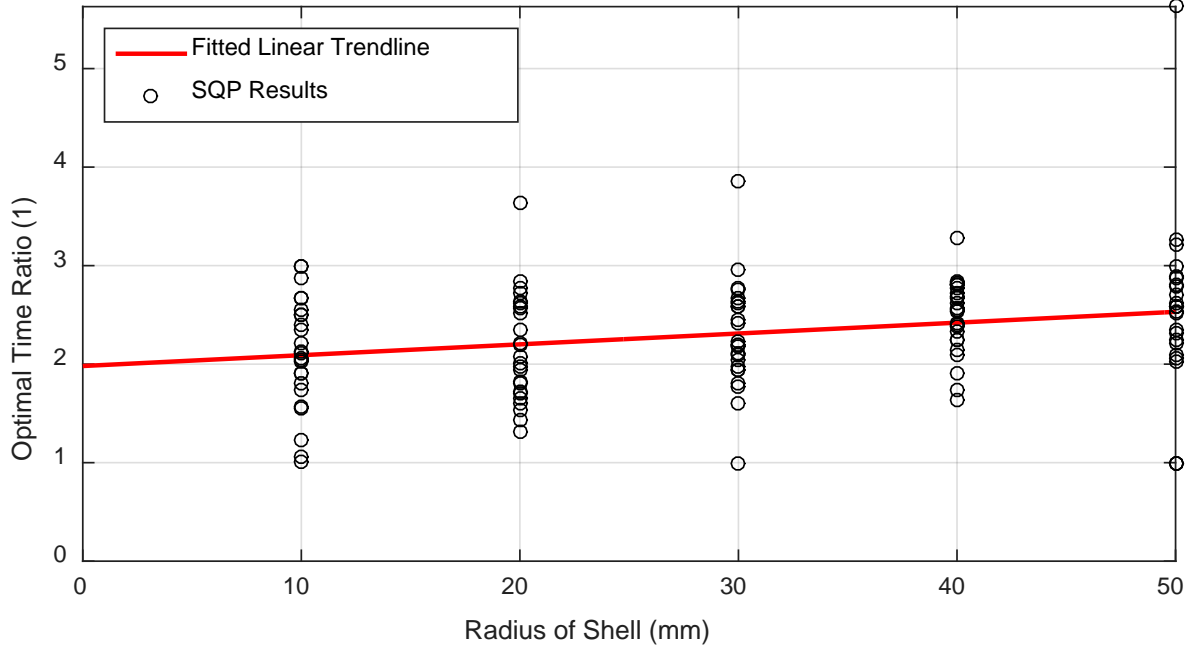
Figure 5.11 Optimized Time Ratio Versus Radius of Shell
Here, a near constant trend is seen in the SQP results, with a much wider range of values. This is expected as during the initial SQP optimization the time ratio was seen to have a less well defined optimal value.
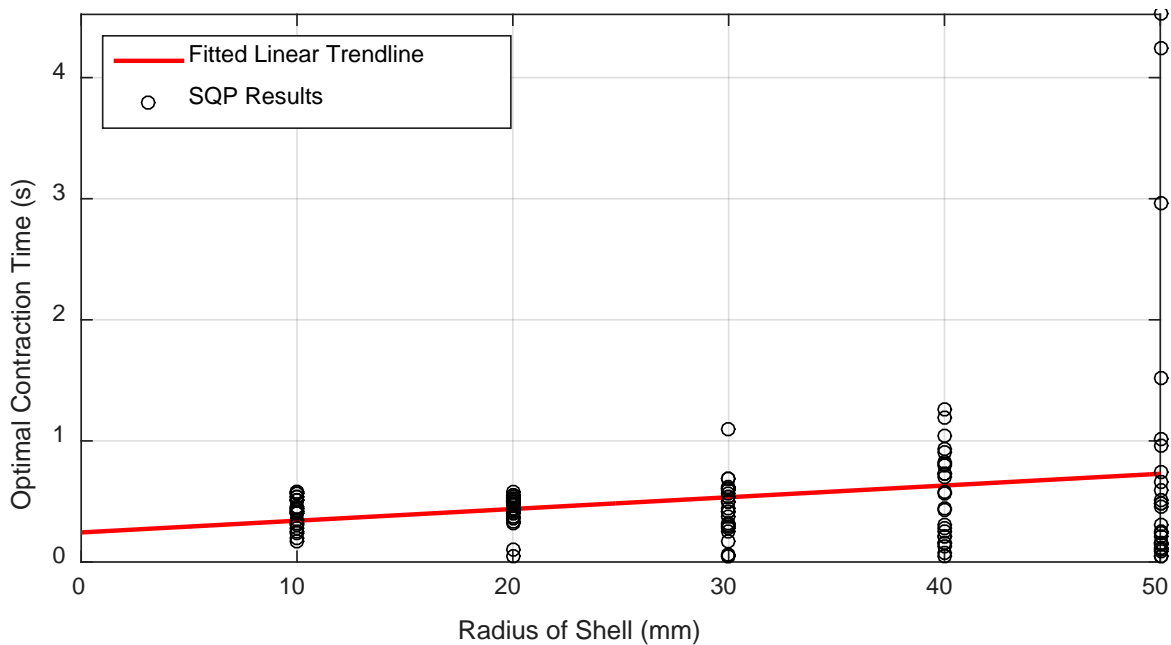
Figure 5.12 Optimized Contraction Time Versus Radius of Shell
Similarly, the contraction time shows a more constant trend as a function of the shell radius. This is also explained in the previous optimization analysis.

$$L_{IPMC} = 1.06\rho - 0.985 \tag{5.6}$$

$$\delta_t = 0.011\rho + 1.98 \tag{5.7}$$

$$t_c = 0.00969\rho + 0.244 \tag{5.8}$$

From the SQP data, linear regressions for each design parameter were found, with the IPMC length, time ratio, and contraction time being given by Equation (5.6), Equation (5.7), and Equation (5.8), respectively. The near one-to-one trend of the IPMC length seen in Table 5.6 is highlighted by the near unity slope of its regression equation. Similarly, both regression equations for time ratio and contraction time show a near constant form, with a small slope that may be explained by the larger standard deviation seen in the previous analysis. At larger shell radii, the optimal value is seen to be less distinct, particularly for the IPMC length.

5.4. Discussion

The optimization approach here is somewhat limited due to the use of only three design parameters. While other variables certainly play important roles in the functionality of such a robot design, the current model components do not lend themselves for a full suite of multi-variable optimization. In particular, the RCW circuit model is not robust enough to capture the effects of back relaxation, steric interactions, and thickness of the polymer on the actuation performance of the IPMC. Additionally, the choice of a linear beam theory limits the IPMC deflection to small strains, and hence large deformations of the shell wall cannot be accounted for in the overall model. This also limits the capability to optimize the overall size of the robot.

As mentioned earlier, when attempting to optimize the size of the robot, the constrained on the IPMC length is very important. The model is not capable of handling a zero-percentage of passive material in the shell wall, and as such there must be some constraint in place to ensure that as the size of the robot increases the IPMC does not fully eliminate the passive portion in the design. Furthermore, from experience with the IPMC actuators, there is a tradeoff between performance and length, whereas the IPMC scales its actuation capabilities degrade. This phenomenon is not currently captured within the proposed models, and hence the scale effects on optimization demonstrated here are not valid at the larger size of robots. With the limitations of the circuit model in predicting the behavior of the IPMC at larger sizes, the optimization of the overall size and geometry of the robot is currently not feasible.

Chapter 6. Conclusion

Biology has been shown to provide invaluable inspiration for the modeling, design, and development of soft robotic systems. Here, insight of the jet propulsion mechanism found in jellyfish lead to a new theory about an improved swimming mechanism for small aquatic robots.

A robust finite element model of the complex Poisson-Nernst-Planck system of equations for IPMC actuation was described, wherein a reduction in the problem's dimensionality was leveraged to drastically improve on the computational overhead required to solve these complex Multiphysics problems. The described approach was shown to give highly accurate results in good agreement with other modeling approaches found in literature. This was achieved by solving the PNP system in 1D and using a mapping equation to transform the results on this lower dimensional domain onto a full 2D domain, where the electromechanical transduction was solved and the IPMC displacement was calculated. This finite element model was then shown to be in good agreement with experimental data taken from an actual IPMC.

Similarly, an equivalent circuit model was described which included resistive, capacitive, and Warburg impedances. The circuit model provides a quick, easy to implement, and highly modular model for the electrochemical behavior of IPMC actuators. This approach, when combine with an electromechanical coupling equation, can be used to model IPMC actuator displacement in response to an external voltage input. Using a straight beam model, the circuit model was shown to be in good agreement with both experimental data as well as the complex finite element implementation.

Using a simplified geometrically defined model, the proposed biomimetic robot design was proved to be at least feasibly and to provide potential efficiency improvements over its biological inspiration. A simple ellipsoid geometry was found to provide a useful tool for the

description of a robotic system but lacked a physical basis that was desired for a more well-defined model. The model still provided some critical information and insight into how a robot of this design may function and behave as compared to its biological jellyfish inspiration.

The simplified geometric approach was improved upon by starting from a physical basis, namely, a beam theory found in the field of solid mechanics. Due to the spherical design, a linear curved beam was proposed and the deformation of such beam under a uniformly distributed load was calculated approximately through a Galerkin trial function. The trial function was specifically chosen to include only monomial terms so that future endeavors for developing a dynamic model for the swimming behavior would be easier to express mathematically. The choice of trial function was shown to be extremely useful in describing the internal volume and cross-sectional area for the physics-based model. The model was then completed by coupling the equivalent circuit model for IPMC deformation with the curved beam theory used to provide a fast and accurate modeling approach that is grounded in physical principles. The physics-based approach was found to be in good agreement with both the geometric and biological jellyfish models for the swimming regimes tested. Using the newly developed model, the ability for the proposed robot design be used as a low volume fluid pump was described. By changing how the device was constrained and examining a small control volume at the outlet of the system, it was shown that it is possible to generate nearly continuous flow or pulsating flow from the same device while relying only on low voltage inputs for the IPMC actuators.

Finally, an optimization of the design was conducted. A few design parameters were chosen and their effect on the distance traveled by the robot was modeled. After narrowing down on three parameters, namely the IPMC length, contraction time, and time ratio, surface plots of the robot's displacement were created to gain some valuable insight into the existence of a

possible optimal parameter set. From there, an implementation of sequential quadratic programming was used to find the exact optimal solution. In this optimization, 100 trials were used to construct mean and standard deviations of the design variables to verify that the optimization routine found a good maximum. From the results obtained, the optimal solution was verified, and the optimal model was compared to the original unoptimized implementation. The optimal parameters were shown to increase performance significantly, evident from plots of the distance traveled over time as well as comparing the average thrust and propulsion efficiency. A look at the scale effects on the optimal design parameters was taken, and it was shown that as the robot increases in size, the IPMC actuator necessary to achieve optimal performance also must increase linearly. The limitations of the model with regard to optimization were discussed. Specifically, the linear deflection and limited circuit model do not allow for a more complex multi-variable optimization with scaling to be conducted. This is an important topic for future research.

Ultimately, the work here demonstrated the value in biological inspiration and model for the development of new and efficient soft robotic systems. The final physics-based model is highly modular and flexible in terms of the techniques and approaches used. The Galerkin approximation technique allows for boundary conditions on the beam to be changed with ease to allow for changes in the robot design, as well as provide a simple and concise way to describe the physical parameters that are key to modeling the swimming behavior of the robot. This approach also allows for more complex beam equations to be used, where the requirement on infinitesimal strain may be relaxed and larger deflections of the IPMC actuator may be captured. Additionally, the role of the circuit model is highly adaptable for new and improved equivalent circuit models, or other such approaches to modeling the electrochemical nature of IPMCs.

Chapter 7. Future Work

7.1. Fabrication of Prototype

To verify the model developed, a prototype for experiments must be created. Currently, some work has been made in this endeavor. The body of the robot would ideally be made of a soft, flexible, passive material that will allow for easy deformation of an enclosed internal volume. A design for the shell body of the robot has been drawn in CAD software, shown in Figure 7.1, to manufacture molds that can be used to cast a flexible elastomer body. Using this CAD model, two mold designs have been drawn and 3D printed for the manufacturing of a prototype robot.
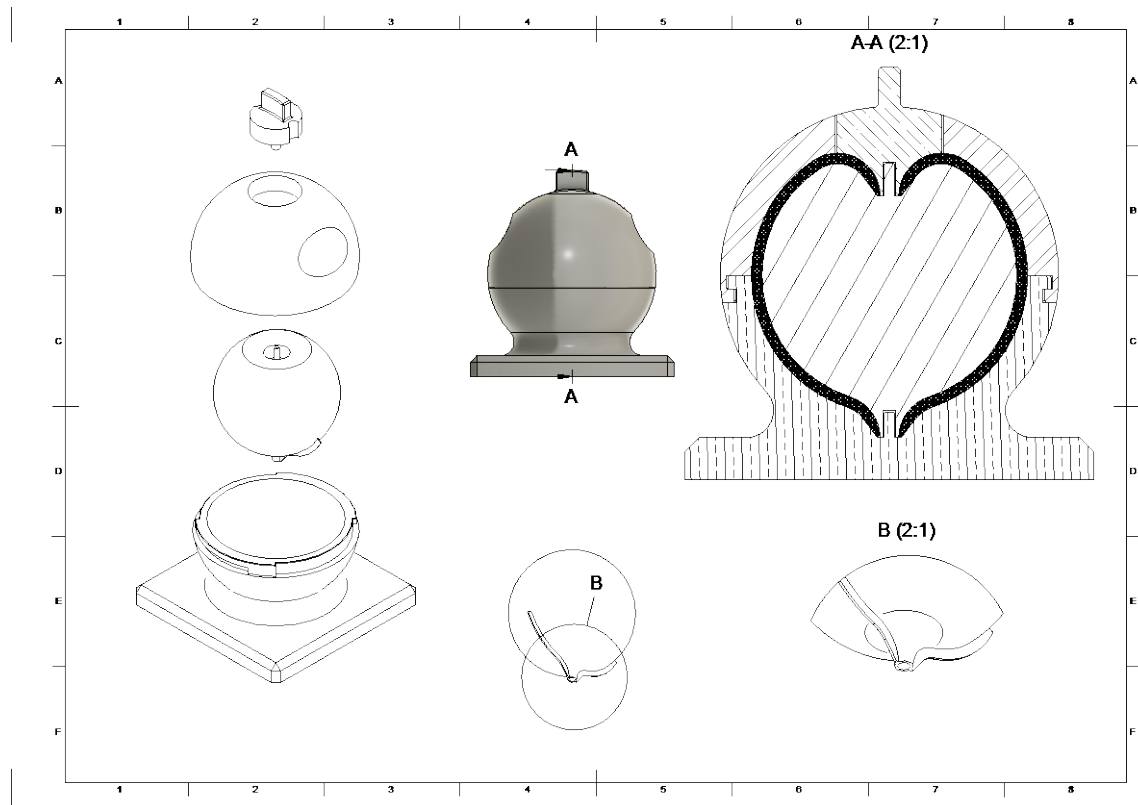
Figure 7.1 Engineering Sketch of Prototype Mold Design
With the mold design shown, a soft elastomer material such as Ecoflex is cast into void shown in black in the A-A cross-section and cured to obtain a flexible shell.

The first mold is a four-part design that allows for an elastomer material to be poured and cast around a center core, seen in black in the cross-section A-A of Figure 7.1. This design requires the cured body to be cut and pulled off the central core and bonded back together to create an air tight shell. The expanded view B in Figure 7.1 shows two tabs where the cast body will be thin enough to easily cut and separate from the central core. With the shell created, the mold can be used without the core to recast and patch the cut portion of the body.

A second mold has been designed that allows two half-shells to be cast simultaneously. In the assembly process of the prototype these half-shells will be bonded to the exterior surface of the main body to form pockets for IPMC actuators to be embedded into the body of the device. These molds have been 3D printed, as seen in Figure 7.3 and Figure 7.4, and an initial prototype is currently being manufactured, as shown in Figure 7.5.

Figure 7.2 Second Mold Design CAD Image
This mold design allows for two half shells to be cast and then bonded together in order to avoid cutting the shell off the central core of the previous design.

Figure 7.3 First 3D Printed Mold
The first mold design was 3D printed for initial prototyping.
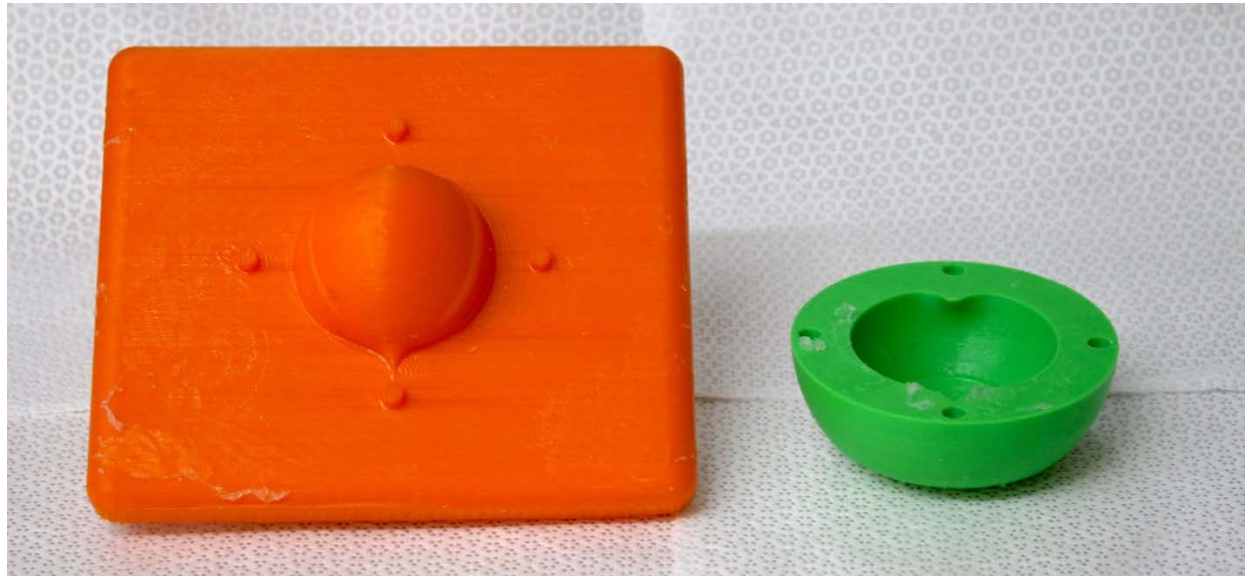
Figure 7.4 Second 3D Printed Mold
Similarly, the second mold was 3D printed to assemble pockets that will ultimately hold the IPMC actuators in the final prototype.

Figure 7.5 Current Status of Elastomer Prototype Body
Using the 3D printed molds, the above Ecoflex shells have been cast and are under assembly.

7.2. Structure of Future Experimental Study

The experimental procedure is modeled after the work of [98] where the robot will be placed within a flow tank and its thrust and drag characteristics experimentally determined and compared to the proposed model. Furthermore, the swimming performance of the robot is to be evaluated through computer vision techniques. The robot may be placed within the flow tank and video footage will be recorded of the swimming behavior over a set period. Using optical feature tracking using optical flow techniques, along with calibrating the pixel-to-distance correlation for the video, the experimental swimming displacement can be collected and compared to the physics-based model. The drag characteristics of the robot body can be experimentally measured by towing the robot through the water at various speeds while a load cell is used to record the towing force. This allows for the drag force and hence drag coefficient to be calculated. A similar experimental setup may be used to measure the thrusting force. In this case, the system is kept static and the robot thrusts against the load cell measurement arm, and the resulting thrust force may be measured. This can be directly compared to the proposed model for verification.

7.3. Additions to Physics-Based Model

One of the limitations of the currently proposed model is the reliance on infinitesimal strain in the beam theory. The proposed model has been shown to provide accurate beam deflection results using a Galerkin approximation. The flexibility gained by using such an approximation technique allows for easy modification of the beam theory used. By transitioning from the linear strain theory to a non-linear one, the same Galerkin approach can be used while the rest of the proposed model retains the same results and forms. This will ultimately allow for the modeling of large IPMC deformations and thus yield a more physically accurate model.

Similarly, the equivalent circuit model is easily changed for other variants that include nonlinear circuit components or more finely tuned parameters. One interesting approach that is being investigated is the use of a 1D finite element implementation outside of COMSOL Multiphysics. The 1D approach has been shown to provide accurate results for the PNP system, and with this multiphysics-based model the more robust electromechanical coupling equations may be used. This, combined with a nonlinear beam theory, is very attractive for developing a highly accurate model of soft robotic systems.

Appendix A: Additional Figures of COMSOL Domains and Mesh

Figure A.1 Finite Element Mesh for 2D PNP Domain
The extremely dense mesh used in the 2D PNP COMSOL model leads to longer computation time and larger stiffness matrices in the FEM approach.

Figure A.2 Enhanced View of Figure A.1
The enhanced view of the 2D mesh shows the high aspect ratio rectangular elements within the polymer region of the model.

Figure A.3 Finite Element Mesh of 2D Solid Mechanics Domain
The 2D domain has a similar structure but has lower density and less severe aspect ratio elements.
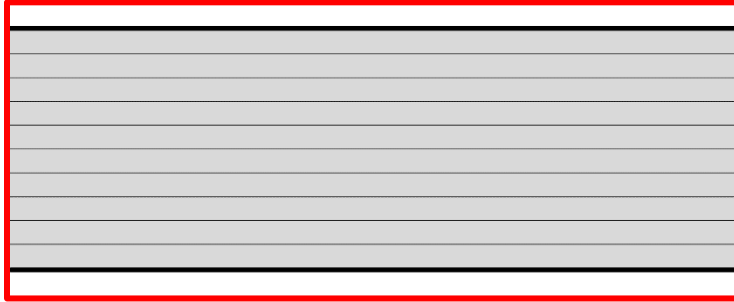
Figure A.4 Enhanced View of Figure A.3
This view shows the larger elements used to calculate the mechanical deformation in the solid mechanics domain.
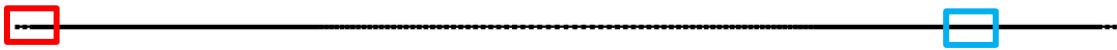
Figure A.5 Finite Element Mesh of 1D PNP Domain
The refined 1D domain has two areas of interest when investigating the structure of the mesh. On the left is the electrode-polymer interface, and the right is the polymer-polymer interface at the buffer region.
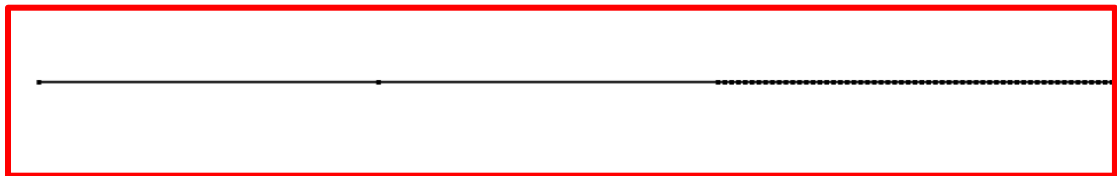
Figure A.6 Enhanced View of Figure A.5, Electrode-Polymer Interface
The electrode-polymer interface shows the stark contrast between element density in the two respective sub-domains.
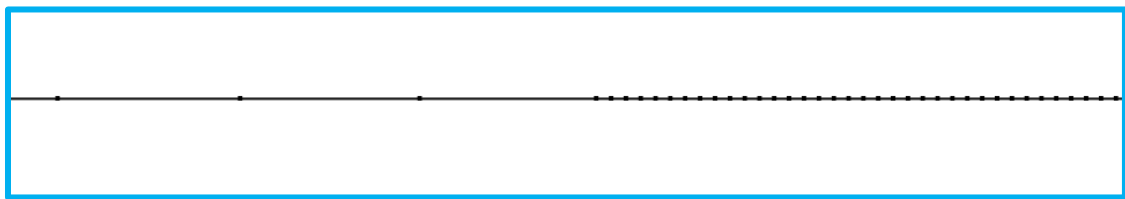
Figure A.7 Enhanced View of Figure A.5, Membrane-Membrane Interface
Similarly, the polymer-polymer interface has a drastic difference in mesh density.

Figure A.8 Finite Element Mesh of 2D Solid Mechanics Domain for 1D PNP Modeling
A similar 2D domain is used for the solid mechanics physics when using the 1D PNP model.
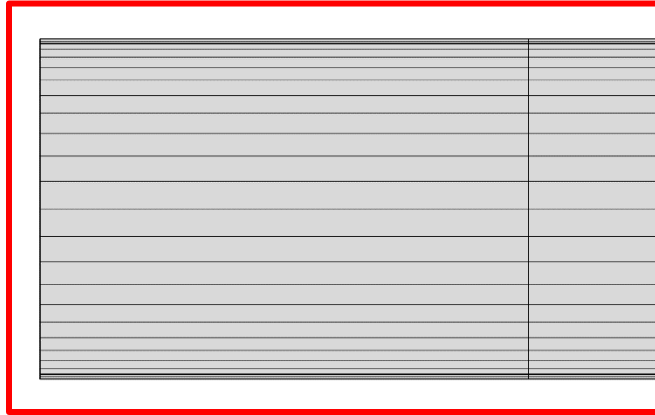
Figure A.9 Enhanced View of Figure A.8
In this domain, the mesh is refined near the electrodes with a geometric sequence in order to more accurately capture the electromechanical coupling after the 1D PNP solution is mapped to the 2D domain.

Appendix B: Coefficients for Volume and Cross-Sectional Area in Physics-Based Model

$$A_0 = \rho^3 {}_0^{\frac{\pi}{2}} \bar{I}_0 \tag{B.1}$$

$$A_1 = 3\rho^2 \left[\sum_{n=0}^{N_w} {}_\alpha^\beta \bar{I}_n \widetilde{\widehat{w}}_n \right]\Bigg|_0^{\frac{\pi}{2}} = 3\rho^2 \left(\sum_{n=0}^{N_w} \left[{}_0^\beta \bar{I}_n \widetilde{\widehat{w}}_n \right]_{active} + \left[{}_\beta^{\frac{\pi}{2}} \bar{I}_n \widetilde{\widehat{w}}_n \right]_{passive} \right) \tag{B.2}$$

$$A_2 = 3\rho \left[\sum_{m=0}^{N_w} \sum_{n=0}^{N_w} {}_\alpha^\beta \bar{I}_{m\_n} \widetilde{\widehat{w}}_m \widetilde{\widehat{w}}_n \right]\Bigg|_0^{\frac{\pi}{2}}$$
$$= 3\rho \left(\sum_{m=0}^{N_w} \sum_{n=0}^{N_w} \left[{}_0^\beta \bar{I}_{m+n} \widetilde{\widehat{w}}_m \widetilde{\widehat{w}}_n \right]_{active} + \left[{}_\beta^{\frac{\pi}{2}} \bar{I}_{m+n} \widetilde{\widehat{w}}_m \widetilde{\widehat{w}}_n \right]_{passive} \right) \tag{B.3}$$

$$A_3 = \left[\sum_{l=0}^{N_w} \sum_{m=0}^{N_w} \sum_{n=0}^{N_w} {}_\alpha^\beta \bar{I}_{l+m+n} \widetilde{\widehat{w}}_l \widetilde{\widehat{w}}_m \widetilde{\widehat{w}}_n \right]\Bigg|_0^{\frac{\pi}{2}}$$
$$= \sum_{l=0}^{N_w} \sum_{m=0}^{N_w} \sum_{n=0}^{N_w} \left[{}_0^\beta \bar{I}_{l+m+n} \widetilde{\widehat{w}}_l \widetilde{\widehat{w}}_m \widetilde{\widehat{w}}_n \right]_{active} + \left[{}_\beta^{\frac{\pi}{2}} \bar{I}_{l+m+n} \widetilde{\widehat{w}}_l \widetilde{\widehat{w}}_m \widetilde{\widehat{w}}_n \right]_{passive} \tag{B.4}$$

$$B_0 = \pi \rho^2 \tag{B.5}$$

$$B_1 = 4\rho \sum_{n=0}^{N_w} \frac{\theta^{n+1}}{n+1} \widetilde{\widehat{w}}_n \Bigg|_0^{\pi/2} = 4\rho \left(\sum_{n=0}^{N_w} \left[\frac{\beta^{n+1}}{n+1} \widetilde{\widehat{w}}_n \right]_{active} + \left[\frac{\left(\frac{\pi}{2}\right)^{n+1} - \beta^{n+1}}{n+1} \widetilde{\widehat{w}}_n \right]_{passive} \right) \tag{B.6}$$

$$\begin{aligned} B_2 &= 2 \sum_{m=0}^{N_w} \sum_{n=0}^{N_w} \frac{\theta^{n+m+1}}{n+m+1} \widetilde{\widehat{w}}_n \widetilde{\widehat{w}}_m \Bigg|_0^{\pi/2} \\ &= 2 \sum_{m=0}^{N_w} \sum_{n=0}^{N_w} \left[\frac{\beta^{n+m+1}}{n+m+1} \widetilde{\widehat{w}}_n \widetilde{\widehat{w}}_m \right]_{active} \\ &+ \left[\frac{\left(\frac{\pi}{2}\right)^{n+m+1} - \beta^{n+m+1}}{n+m+1} \widetilde{\widehat{w}}_n \widetilde{\widehat{w}}_m \right]_{passive} \end{aligned} \tag{B.7}$$

$* \ \ \beta = \dfrac{L_{ipmc}}{\rho}$

Bibliography

[1]   Bar-Cohen, Y., 2002, "Electroactive Polymers as Artificial Muscles: A Review," J. Spacecr. Rockets, **39**(6), pp. 822–827.

[2]   O'Halloran, A., O'Malley, F., and McHugh, P., 2008, "A Review on Dielectric Elastomer Actuators, Technology, Applications, and Challenges," J. Appl. Phys., **104**(7).

[3]   Bonomo, C., Fortuna, L., Giannone, P., Graziani, S., and Strazzeri, S., 2007, "A Nonlinear Model for Ionic Polymer Metal Composites as Actuators," Smart Mater. Struct., **16**(1), pp. 1–12.

[4]   Trabia, S., Olsen, Z., and Kim, K. J., 2017, "Searching for a New Ionomer for 3D Printable Ionic Polymer-Metal Composites: Aquivion as a Candidate," Smart Mater. Struct., **26**(11).

[5]   Kim, K. J., 2007, "Ionic Polymer-Metal Composites as a New Actuator and Transducer Material," *Electroactive Polymers for Robotics Applications*, pp. 165–198.

[6]   Bonomo, C., Fortuna, L., Giannone, P., Graziani, S., and Strazzeri, S., 2006, "A Model for Ionic Polymer Metal Composites as Sensors," Smart Mater. Struct., **15**(3), pp. 749–758.

[7]   Akle, B., and Habchi, W., 2013, "Finite Element Modeling of the Sensing and Energy Harvesting Performance in Ionic Polymer Metal Composites," Electroact. Polym. Actuators Devices, **8687**, p. 86870G.

[8]   Porfiri, M., 2009, "An Electromechanical Model for Sensing and Actuation of Ionic Polymer Metal Composites," Smart Mater. Struct., **18**(1), p. 15016.

[9]   Chen, Z., Tan, X., Will, A., and Ziel, C., 2007, "A Dynamic Model for Ionic Polymer-Metal Composite Sensors," Smart Mater. Struct., **16**(4), pp. 1477–1488.

[10]   Cha, Y., and Porfiri, M., 2014, "Mechanics and Electrochemistry of Ionic Polymer Metal

Composites," J. Mech. Phys. Solids, **71**(1), pp. 156–178.

[11] Shahinpoor, M., 2016, *Fundamentals of Ionic Polymer Metal Composites (IPMCs)*.

[12] Shen, Q., Palmre, V., Stalbaum, T., and Kim, K. J., 2015, "A Comprehensive Physics-Based Model Encompassing Variable Surface Resistance and Underlying Physics of Ionic Polymer-Metal Composite Actuators," J. Appl. Phys., **118**(12).

[13] Schicker, D., and Wallmersperger, T., 2013, "Modeling and Simulation of the Chemo-Electro-Mechanical Behavior of Ionic Polymer-Metal Composites," J. Appl. Phys., **114**(16).

[14] Shahinpoor, M., and Kim, K. J., 2001, "Ionic Polymer-Metal Composites: I. Fundamentals," Smart Mater. Struct., **10**(4), pp. 819–833.

[15] Kim, K. J., and Shahinpoor, M., 2003, "Ionic Polymer-Metal Composites: II. Manufacturing Techniques," Smart Mater. Struct., **12**(1), pp. 65–79.

[16] Jo, C., Pugal, D., Oh, I. K., Kim, K. J., and Asaka, K., 2013, "Recent Advances in Ionic Polymer-Metal Composite Actuators and Their Modeling and Applications," Prog. Polym. Sci., **38**(7), pp. 1037–1066.

[17] Wallmersperger, T., Leo, D. J., and Kothera, C. S., 2007, "Transport Modeling in Ionomeric Polymer Transducers and Its Relationship to Electromechanical Coupling," J. Appl. Phys., **101**(2).

[18] Chu, W. S., Lee, K. T., Song, S. H., Han, M. W., Lee, J. Y., Kim, H. S., Kim, M. S., Park, Y. J., Cho, K. J., and Ahn, S. H., 2012, "Review of Biomimetic Underwater Robots Using Smart Actuators," Int. J. Precis. Eng. Manuf., **13**(7), pp. 1281–1292.

[19] Brunetto, P., Fortuna, L., Graziani, S., and Strazzeri, S., 2008, "A Model of Ionic Polymer-Metal Composite Actuators in Underwater Operations," Smart Mater. Struct.,

17(2).

[20]   Abdelnour, K., Mancia, E., Peterson, S. D., and Porfiri, M., 2009, "Hydrodynamics of Underwater Propulsors Based on Ionic Polymer-Metal Composites: A Numerical Study," Smart Mater. Struct., **18**(8).

[21]   Kim, K. J., Yim, W., Paquette, J. W., and Kim, D., 2007, "Ionic Polymer-Metal Composites for Underwater Operation," J. Intell. Mater. Syst. Struct., **18**(2), pp. 123–131.

[22]   Yim, W., Lee, J., and Kim, K. J., 2007, "An Artificial Muscle Actuator for Biomimetic Underwater Propulsors," Bioinspiration and Biomimetics, **2**(2).

[23]   Sareh, S., Rossiter, J., Conn, A., Drescher, K., and Goldstein, R. E., 2012, "Swimming like Algae: Biomimetic Soft Artificial Cilia," J. R. Soc. Interface, **10**(78), pp. 20120666–20120666.

[24]   Shen, Q., Wang, T., and Kim, K. J., 2015, "A Biomimetic Underwater Vehicle Actuated by Waves with Ionic Polymer-Metal Composite Soft Sensors," Bioinspir. Biomim., **10**(5), p. 55007.

[25]   Jeon, J. H., Yeom, S. W., and Oh, I. K., 2008, "Fabrication and Actuation of Ionic Polymer Metal Composites Patterned by Combining Electroplating with Electroless Plating," Compos. Part A Appl. Sci. Manuf., **39**(4), pp. 588–596.

[26]   Chen, Z., and Tan, X., 2010, "Monolithic Fabrication of Ionic Polymer-Metal Composite Actuators Capable of Complex Deformation," Sensors Actuators, A Phys., **157**(2), pp. 246–257.

[27]   Rosly, M. A., Yussof, H., Shaari, M. F., Samad, Z., Kamaruzaman, D., and Omar, A. R., 2017, "Speed Control Mechanism for IPMC Based Biomimetic Flapping Thruster," pp. 5–7.

[28] Zheng, C., Shatara, S., and Tan, X., 2009, "Modeling of Robotic Fish Propelled by an Ionic Polymer-Metal Composite Caudal Fin," Proc. SPIE - Int. Soc. Opt. Eng., **7287**(3), pp. 448–459.

[29] Yang, T., and Chen, Z., 2015, "Development of 2D Maneuverable Robotic Fish Propelled by Multiple Ionic Polymer-Metal Composite Artificial Fins," 2015 IEEE Int. Conf. Robot. Biomimetics, IEEE-ROBIO 2015, **1**(2), pp. 255–260.

[30] Kopman, V., and Porfiri, M., 2012, "Design, Modeling, and Characterization of a Miniature Robotic-Fish for Research and Education in Biomimetics and Bioinspiration," IEEE/ASME Trans. Mechatronics, **18**(2), pp. 471–483.

[31] Shen, Q., Wang, T., Wen, L., and Liang, J., 2013, "Modelling and Fuzzy Control of an Efficient Swimming Ionic Polymer-Metal Composite Actuated Robot," Int. J. Adv. Robot. Syst., **10**, pp. 1–13.

[32] Phamduy, P., Vazquez, M. A., Kim, C., Mwaffo, V., Rizzo, A., and Porfiri, M., 2017, "Design and Characterization of a Miniature Free-Swimming Robotic Fish Based on Multi-Material 3D Printing," Int. J. Intell. Robot. Appl., **1**(2), pp. 209–223.

[33] Chen, Z., Um, T. I., and Bart-Smith, H., 2011, "A Novel Fabrication of Ionic Polymer-Metal Composite Membrane Actuator Capable of 3-Dimensional Kinematic Motions," Sensors Actuators, A Phys., **168**(1), pp. 131–139.

[34] Chen, Z., Um, T. I., and Bart-Smith, H., 2012, "Bio-Inspired Robotic Manta Ray Powered by Ionic Polymer-Metal Composite Artificial Muscles," Int. J. Smart Nano Mater., **3**(4), pp. 296–308.

[35] Shen, Q., Wang, T., Liang, J., and Wen, L., 2013, "Hydrodynamic Performance of a Biomimetic Robotic Swimmer Actuated by Ionic Polymer-Metal Composite," Smart

Mater. Struct., **22**(7).

[36]   Yeom, S.-W., and Oh, I.-K., 2009, "A Biomimetic Jellyfish Robot Based on Ionic

       Polymer Metal Composite Actuators," Smart Mater. Struct., **18**(8), p. 85002.

[37]   Najem, J., and Leo, D. J., 2012, "A Bio-Inspired Bell Kinematics Design of a Jellyfish

       Robot Using Ionic Polymer Metal Composites Actuators," **8340**, p. 83401Q.

[38]   Villanueva, A., Priya, S., Anna, C., and Smith, C., 2010, "Robojelly Bell Kinematics and

       Resistance Feedback Control," pp. 1–6.

[39]   Xiao, J., Duan, J., and Yu, J., 2013, "Design and Implementation of a Novel Biomimetic

       Robotic Jellyfish," 2013 IEEE Int. Conf. Robot. Biomimetics, ROBIO 2013, (December),

       pp. 988–993.

[40]   Villanueva, A. A., Joshi, K. B., Blottman, J. B., and Priya, S., 2010, "A Bio-Inspired

       Shape Memory Alloy Composite (BISMAC) Actuator," Smart Mater. Struct., **19**(2).

[41]   Villanueva, A., Smith, C., and Priya, S., 2011, "A Biomimetic Robotic Jellyfish

       (Robojelly) Actuated by Shape Memory Alloy Composite Actuators," Bioinspiration and

       Biomimetics, **6**(3).

[42]   Yang, Y., Ye, X., and Guo, S., 2007, "A New Type of Jellyfish-like Microrobot," IEEE

       ICIT 2007 - 2007 IEEE Int. Conf. Integr. Technol., (2006), pp. 673–678.

[43]   Salazar, R., Fuentes, V., and Abdelkefi, A., 2018, "Classification of Biological and

       Bioinspired Aquatic Systems: A Review," Ocean Eng., **148**(September 2017), pp. 75–114.

[44]   Lauder, G. V., Anderson, E. J., Tangorra, J., and Madden, P. G. A., 2007, "Fish

       Biorobotics: Kinematics and Hydrodynamics of Self-Propulsion," J. Exp. Biol., **210**(16),

       pp. 2767–2780.

[45]   Lu, X. Y., Yin, X. Z., Yang, J. M., and Tong, B. G., 2010, "Studies of Hydrodynamics in

Fishlike Swimming Propulsion," J. Hydrodyn., **22**(5 SUPPL. 1), pp. 17–22.

[46] Triantafyllou, G. S., Triantafyllou, M. S., and Grosenbaugh, M. A., 1993, "Optimal Thrust Development in Oscillating Foils with Application to Fish Propulsion," J. Fluids Struct., **7**(2), pp. 205–224.

[47] Alben, S., Miller, L. A., and Peng, J., 2013, "Efficient Kinematics for Jet-Propelled Swimming," J. Fluid Mech., **733**, pp. 100–133.

[48] Spagnolie, S. E., and Lauga, E., 2010, "Jet Propulsion without Inertia," Phys. Fluids, **22**(8).

[49] Evans, A. A., Spagnolie, S. E., and Lauga, E., 2010, "Stokesian Jellyfish: Viscous Locomotion of Bilayer Vesicles," Soft Matter, **6**(8), p. 1737.

[50] Dabiri, J. O., 2005, "On the Estimation of Swimming and Flying Forces from Wake Measurements," J. Exp. Biol., **208**(18), pp. 3519–3532.

[51] Dabiri, J. O., Colin, S.P, Costello, J. H., Gharib, M., 2005, "Flow Patterns Generated by Oblate Medusan Jellyfish: Field Measurements and Laboratory Analyses," J. Exp. Biol., **208**(7), pp. 1257–1265.

[52] Dabiri, J. O., 2003, "Sensitivity Analysis of Kinematic Approximations in Dynamic Medusan Swimming Models," J. Exp. Biol., **206**(20), pp. 3675–3680.

[53] Demont, M. E., and Gosline, M., 1988, "Mechanics of Jet Propulsion in the Hydromedusan Jellyfish, *Polyorchis Penicillatus*. I. Mechanical Properties of the Locomotor Structure," J. Exp. Biol., **134**(1), pp. 313–332.

[54] Demont, M. E., and Gosline, J. M., 1988, "Mechanics of Jet Propulsion in the Hydromedusan Jellyfish, Polyorchis Penicillatus: III. A NATURAL RESONATING BELL; THE PRESENCE AND IMPORTANCE OF A RESONANT PHENOMENON IN

THE LOCOMOTOR STRUCTURE," J. Exp. Biol., **134**, pp. 333–345.

[55] Demont, M. E., and Gosline, M., 1988, "Mechanics of Jet Propulsion in the
Hydromedusan Jellyfish, Polyorchis Penicillatus. II. ENERGETICS OF THE JET
CYCLE," J. Exp. Biol., **134**(1), pp. 313–332.

[56] McHenry, M. J., 2003, "The Ontogenetic Scaling of Hydrodynamics and Swimming
Performance in Jellyfish (Aurelia Aurita)," J. Exp. Biol., **206**(22), pp. 4125–4137.

[57] Shorten, M., Davenport, J., Seymour, J. E., Cross, M. C., Carrette, T. J., Woodward, G.,
and Cross, T. F., 2005, "Kinematic Analysis of Swimming in Australian Box Jellyfish,
Chiropsalmus Sp. and Chironex Fleckeri (Cubozoa, Cnidaria: Chirodropidae)," J. Zool.,
267(4), pp. 371–380.

[58] Daniel, T. L., 1983, "Mechanics and Energetics of Medusan Jet Propulsion," Can. J.
Zool., **61**(6), pp. 1406–1420.

[59] Daniel, T. L., 1985, "Cost of Locomotion: Unsteady Medusan Swimming," J. Exp. Biol.,
119, pp. 149–164.

[60] Tokic, G., and Yue, D. K. P., 2012, "Optimal Shape and Motion of Undulatory Swimming
Organisms," Proc. R. Soc. B Biol. Sci., **279**(1740), pp. 3065–3074.

[61] Simcik, M., Puncochar, M., and Ruzicka, M. C., 2014, "Added Mass of a Spherical Cap
Body," Chem. Eng. Sci., **118**, pp. 1–8.

[62] Ruzicka, M. C., Simcik, M., and Puncochar, M., 2015, "How to Estimate Added Mass of a
Spherical Cap Body: Two Approaches," Chem. Eng. Sci., **134**, pp. 308–311.

[63] Nemat-Nasser, S., and Li, J. Y., 2000, "Electromechanical Response of Ionic Polymer-
Metal Composites," J. Appl. Phys., **87**(7), pp. 3321–3331.

[64] Shahinpoor, M., and Kim, K. J., 2004, "Ionic Polymer-Metal Composites: III. Modeling

and Simulation as Biomimetic Sensors, Actuators, Transducers, and Artificial Muscles," Smart Mater. Struct., **13**(6), pp. 1362–1388.

[65] Zhu, Z., Asaka, K., Chang, L., Takagi, K., and Chen, H., 2013, "Multiphysics of Ionic Polymer-Metal Composite Actuator," J. Appl. Phys., **114**(8).

[66] Zhu, Z., Asaka, K., Chang, L., Takagi, K., and Chen, H., 2013, "Physical Interpretation of Deformation Evolvement with Water Content of Ionic Polymer-Metal Composite Actuator," J. Appl. Phys., **114**(18).

[67] Porfiri, M., 2008, "Charge Dynamics in Ionic Polymer Metal Composites," J. Appl. Phys., **104**(10).

[68] Chen, Z., Hedgepeth, D. R., and Tan, X., 2008, "A Nonlinear, Control-Oriented Model for Ionic Polymer-Metal Composite Actuators," Proc. IEEE Conf. Decis. Control, pp. 1851–1856.

[69] Chen, Z., Member, S., and Tan, X., 2008, "A Control-Oriented and Physics-Based Model for Ionic Polymer – Metal Composite Actuators," **13**(5), pp. 519–529.

[70] Gutta, S., Lee, J. S., Trabia, M. B., and Yim, W., 2009, "Modeling of Ionic Polymer Metal Composite Actuator Dynamics Using a Large Deflection Beam Model," Smart Mater. Struct., **18**(11).

[71] Lee, S., Park, H. C., and Kim, K. J., 2005, "Equivalent Modeling for Ionic Polymer - Metal Composite Actuators Based on Beam Theories," Smart Mater. Struct., **14**(6), pp. 1363–1368.

[72] Porfiri, M., Sharghi, H., and Zhang, P., 2018, "Modeling Back-Relaxation in Ionic Polymer Metal Composites: The Role of Steric Effects and Composite Layers," J. Appl. Phys., **123**(1), p. 14901.

[73]   Aureli, M., Kopman, V., and Porfiri, M., 2010, "Free-Locomotion of Underwater Vehicles Actuated by Ionic Polymer Metal Composites," IEEE/ASME Trans. Mechatronics, **15**(4), pp. 603–614.

[74]   Davidson, J. D., and Goulbourne, N. C., 2011, "Nonlinear Capacitance and Electrochemical Response of Ionic Liquid-Ionic Polymers," J. Appl. Phys., **109**(8).

[75]   Pugal, D., Kim, K. J., and Aabloo, A., 2011, "An Explicit Physics-Based Model of Ionic Polymer-Metal Composite Actuators," J. Appl. Phys., **110**(8).

[76]   Davidson, J. D., and Goulbourne, N. C., 2011, "Boundary Layer Charge Dynamics in Ionic Liquid-Ionic Polymer Transducers," J. Appl. Phys., **109**(1).

[77]   Wallmersperger, T., Akle, B. J., Leo, D. J., and Kröplin, B., 2008, "Electrochemical Response in Ionic Polymer Transducers: An Experimental and Theoretical Study," Compos. Sci. Technol., **68**(5), pp. 1173–1180.

[78]   Cha, Y., Aureli, M., and Porfiri, M., 2012, "A Physics-Based Model of the Electrical Impedance of Ionic Polymer Metal Composites," J. Appl. Phys., **111**(12).

[79]   Galante, S., Lucantonio, A., and Nardinocchi, P., 2013, "The Multiplicative Decomposition of the Deformation Gradient in the Multiphysics Modeling of Ionic Polymers," Int. J. Non. Linear. Mech., **51**, pp. 112–120.

[80]   Pugal, D., Stalbaum, T., Palmre, V., and Kim, K. J., 2016, "Modeling Ionic Polymer Metal Composites with COMSOL: Step-by-Step Guide," RSC Smart Mater., **2016**–**Janua**(17), pp. 185–214.

[81]   Wallmersperger, T., Kröplin, B., and Gülch, R. W., 2004, "Coupled Chemo-Electro-Mechanical Formulation for Ionic Polymer Gels - Numerical and Experimental Investigations," Mech. Mater., **36**(5–6), pp. 411–420.

[82]   Nemat-Nasser, S., 2002, "Micromechanics of Actuation of Ionic Polymer-Metal Composites," J. Appl. Phys., **92**(5), pp. 2899–2915.

[83]   Nardinocchi, P., Pezzulla, M., and Placidi, L., 2011, "Thermodynamically Based Multiphysic Modeling of Ionic Polymer Metal Composites," J. Intell. Mater. Syst. Struct., **22**(16), pp. 1887–1897.

[84]   Wallmersperger, T., Kroeplin, B., Holdenried, J., and Guelch, R. W., 2001, "Coupled Multifield Formulation for Ionic Polymer Gels in Electric Fields," SPIE's 8th Annu. Int. Symp. Smart Struct. Mater., **4329**(July 2001), pp. 264–275.

[85]   Wallmersperger, T., Horstmann, A., Kroplin, B., and Leo, D. J., 2009, "Thermodynamical Modeling of the Electromechanical Behavior of Ionic Polymer Metal Composites," J. Intell. Mater. Syst. Struct., **20**(6), pp. 741–750.

[86]   Pugal, D., and Kim, K. J., 2012, "Physics Based Model of Ionic Polymer-Metal Composite Electromechanical and Mechanoelectrical Transduction," **3539200**(August 2012), p. 192.

[87]   Paquette, J. W., Kim, K. J., Nam, J.-D., and Tak, Y. S., 2003, "An Equivalent Circuit Model for Ionic Polymer-Metal Composites and Their Performance Improvement by a Clay-Based Polymer Nano-Composite Technique," J. Intell. Mater. Syst. Struct., **14**(10), pp. 633–642.

[88]   Vahabi, M., Mehdizadeh, E., Kabganian, M., and Barazandeh, F., 2011, "Experimental Identification of IPMC Actuator Parameters through Incorporation of Linear and Nonlinear Least Squares Methods," Sensors Actuators, A Phys., **168**(1), pp. 140–148.

[89]   Branco, P. J. C., and Dente, J. A., 2006, "Derivation of a Continuum Model and Its Electric Equivalent-Circuit Representation for Ionic Polymer-Metal Composite (IPMC)

Electromechanics," Smart Mater. Struct., **15**(2), pp. 378–392.

[90] Bard, A. J., and Faulkner, L. R., 1944, *Electrochemical Methods: Fundamentals and Applications*.

[91] Kopman, V., Laut, J., Acquaviva, F., Rizzo, A., and Porfiri, M., 2015, "Dynamic Modeling of a Robotic Fish Propelled by a Compliant Tail," IEEE J. Ocean. Eng., **40**(1), pp. 209–221.

[92] Sun, A.-B., Bajon, D., Moschetta, J.-M., Benard, E., and Thipyopas, C., 2015, "Integrated Static and Dynamic Modeling of an Ionic Polymer–metal Composite Actuator," J. Intell. Mater. Syst. Struct., **26**(10), pp. 1164–1178.

[93] Morrison, F. A., 2013, "An Introduction to Fluid Mechancis," Cambridge Univ. Press. New York.

[94] Korotkin, A. I., 2009, "Added Masses of Ship Structures," Fluid Mech. Its Appl., **88**.

[95] Byskov, E., 2013, "Elementary Continuum Mechanics for Everyone," Solid Mech. Its Appl., **194**.

[96] Lee, S., Kim, K. J., and Park, H. C., 2006, "Modeling of an IPMC Actuator-Driven Zero-Net-Mass-Flux Pump for Flow Control," J. Intell. Mater. Syst. Struct., **17**(6), pp. 533–541.

[97] Rao, S. S., 2009, *Engineering Optimization: Theory and Practice*, John Wiley & Sons.

[98] Shen, Q., 2017, "THEORETICAL AND EXPERIMENTAL INVESTIGATION ON THE MULTIPLE SHAPE MEMORY IONIC POLYMER-METAL COMPOSITE ACTUATOR."

Curriculum Vitae

Zakai J. Olsen

Zakai.Olsen@gmail.com
www.linkedin.com/in/zakai-olsen-8685a8110

PROFESSIONAL EXPERIENCE

Graduate Research Assistantship, University of Nevada, Las Vegas, 1/2017 – Present

Conducted original research in the fields of soft robotics and smart materials for publication and oral presentation in academic journals and conferences.

- Designed prototype biomimetic actuator using mathematical and finite element modeling techniques. Source of proposal material that secured $18,000 fellowship.
- Successfully developed method for the additive manufacturing of ionic-polymer membranes used as soft robotic actuators.
- Devised workflow to utilize DICOM image data in the modeling of biological structures for the design of soft robot components.

Undergraduate Research Assistant, University of Nevada, Las Vegas, 12/2014 - 12/2016

Assisted MS and PhD students in their daily research activities. Conducted preliminary research on up-and-coming topics in smart materials.

- Worked as a primary investigator on additive manufacturing techniques for ionic-polymer membranes.
- Designed and fabricated prototype fixtures for lab experiments using CAD, additive manufacturing, and machine shop skills.

Engineering Research Intern, KAIST University (Daejeon, South Korea), 7/2016

Participated on an international team researching soft robotics and artificial muscles (NSF Grant #1545857).

- Created mathematical model simulating the kinematics of IPMC based artificial cilia.
- Assembled comprehensive reports on active research progress and presented findings to peers and colleagues within the research community.

TECHNICAL SKILLS

Software: MATLab, Simulink, Solidworks, Fusion 360, COMSOL, LabView, Python, C++, OpenCV
Research and Design: Finite Element Analysis (FEA), Mathematical Modeling, Additive Manufacturing, Structural Mechanics, Numerical Methods

EDUCATION

Master of Science in Engineering (MSE), Mechanical Engineering, 5/2018 (Expected)

University of Nevada, Las Vegas – Las Vegas, Nevada
Specialization: Dynamic Systems and Controls

Bachelor of Science in Engineering (BSE), Mechanical Engineering, 12/2016

University of Nevada, Las Vegas – Las Vegas, Nevada
Honors: summa cum laude (3.96 GPA)
Minors: Mathematics and Unmanned Aircraft Systems

HONORS AND AWARDS

Graduate Research Opportunity Fellowship, 9/2017 – 5/2018
Nevada NASA Space Grant Consortium: Awarded $18,000 fellowship for proposal of original research on the biomimetic design of thrust generation and fluid pumping soft robotic actuators for aerospace applications.

Bhatnagar Top Math Minor Award, 6/2017
University of Nevada, Las Vegas – College of Science: Awarded $500 for graduating with the highest GPA within the Mathematics minor.

Class of 2016 Outstanding Graduate, 4/2017
University of Nevada, Las Vegas – Department of Mechanical Engineering: Department honors award given to the graduating mechanical engineering student with the highest GPA.

Graebel Outstanding Senior of the Year, 4/2016
University of Nevada, Las Vegas – Howard R. Hughes College of Engineering: Awarded $1,000 for graduating with the highest GPA within the College of Engineering.

RELEVANT PROJECTS

Advanced Dynamics: Created kinematic constraint library and modeled a gantry crane under dynamic payload transport and hoisting. Compared forward dynamic model via the embedding technique with inverse dynamic model via Euler-Lagrange equations for verification of results.

Senior Design Project: Worked on a team developing a base platform for autonomous campus transportation. Utilized OpenCV in Python and C++ to implement HOG descriptor detection, Kalman filter tracking, Hungarian Algorithm assignment, and LK optical flow. Successfully achieved pedestrian detection and tracking that allowed for the preliminary automation of an in-house modified electric vehicle.

Engineering Optimization: As part of a two-member team, coded a genetic algorithm to search for optimal fuzzy logic parameters for a gantry crane controller. Algorithm fitness stabilized after 800 generations and resulting controller showed errors within 1% for travel limit, maximum payload swing, and hoisting height.

PUBLICATIONS

Stalbaum, T., Hwang, T., Trabia, S., Shen, Q., Hunt, R., Olsen, Z., & Kim, K. J. (2017) "Bioinspired Travelling Wave Generation in Soft-Robotics using Ionic Polymer-Metal Composites." International Journal of Intelligent Robotics and Applications.

Trabia, S., Olsen, Z., & Kim, K. J. (2017) "Searching for a new ionomer for 3D printable ionic polymermetal composites: Aquivion as a candidate" Smart Materials and Structures.

Kim, K., Stalbaum, T., Trabia, S., Hwang, T., Olsen, Z., Nelson, S., Shen, Q., Lee, D., Carrico, J., Leang, K., Palmre, V., Nam, J., Park, I., Tiwari, R., Kim, D., Kim, S. (2017). "Guidelines for making Ionic

Polymer-Metal Composite (IPMC) materials as artificial muscles by advanced manufacturing methods: State-of- the-Art. In Advances in manufacturing and processing of materials and structures." (Under preparation for peer review)

Olsen, Z. J. & Kim, K. J. (2018, March). "An IPMC Modeling Approach for Computational Efficiency and Rapid Design Development." SPIE Smart Structures / NDE Conference 10594. (Presentation)

Olsen, Z. J. & Kim, K. J. (2017, March). "IPMC driven thrust generation: A new conceptual design." SPIE Smart Structures / NDE Conference 10163. (Presentation)

Trabia, S., Olsen, Z. J., Hwang, T., & Kim, K. J. (2017, March). "Producing intricate IPMC shapes by means of spray-painting and printing." SPIE Smart Structures / NDE Conference 10163. (Presentation)

RELEVANT COURSEWORK

Mathematical Physics, Perturbation Methods, Advanced Dynamics, Aerodynamics, Finite Element Analysis, Energy and Variational Methods in Applied Mechanics, Engineering Optimization

PROFESSIONAL AFFILIATIONS

American Society of Mechanical Engineers (Student Member)
National Society of Professional Engineers (Student Member)
Tau Beta Pi Engineering Honor Society (Member)
Phi Kappa Phi Honor Society (Inducted 4/2015)

MISCELLANEOUS

Licensure: Engineering Intern (EI) #0T7647, 12/2016
Publications: 2 Journal, 1 Book Chapter (in review)
Presentations: 3 Conference
Hobbies: Photography, Camping, Hiking, Travel
Interests: Multibody Dynamics, Computational Modeling Techniques, Optimization, Continuum Mechanics, Particle Methods (e.g. SPH), Computer Vision, UAS, Robotics, STEM Education